Creep deformation in Mg-Al-Ca-based alloys

by

Jessica Renae TerBush

A dissertation submitted in partial fulfillment
of the requirements for the degree of
Doctor of Philosophy
(Materials Science and Engineering)
in the University of Michigan
2010

Doctoral Committee:

Professor J. Wayne Jones, Co-Chair
Professor Tresa M. Pollock, Co-Chair
Assistant Professor Samantha H. Daly
Bob R. Powell, General Motors

To my family, for all their support over the years

Acknowledgements

This thesis, although it bears only my name, is really the result of the work of many. To acknowledge them all individually would be impossible, but the following people have made significant contributions to the effort.

I can't thank my advisors, Professor J. Wayne Jones and Professor Tresa M. Pollock, enough for all their guidance and support over the years. Thank you for all the opinions, for asking questions that I couldn't quite answer at the time, for showing me what it truly means to a Materials Scientist. Working with the two of you was one of the best decisions I ever made, and I am truly grateful for the opportunity.

Much gratitude is also due to Drs. Akane Suzuki and Nicholas Saddock, my collaborators and mentors during the early years of grad school. Thank you for never being too busy to answer my questions, for always being willing to demonstrate a technique or train me on the various microscopes, and for your friendship along the way. Thanks also to Dr. Raghav Adharapurapu, for always being willing to share his knowledge and providing much needed support over the years.

Speaking of support, I would have been lost without the help of Chris Torbet. Chris, you are literally a life-saver for our group! Thanks also to Olivia Chen, Eric Lee and Laura LaCasse, my crew of undergrad research assistants over the years. Your hard work is greatly appreciated and I hope you all learned something during our time together – besides the fact that polishing Mg can be… frustrating… at times. For all his patience and help troubleshooting the TEM and electron microprobe over the years, I would also like to thank Carl Henderson from Central Campus EMAL.

Thanks to Bob Powell from General Motors, for all the conversations and advice along the way.

To my fellow members of the Pollock and Jones groups, past and present: I have learned so much from our interactions and really treasure the friendships that I've developed with you. I'm very grateful that I've had the chance to work with you, and wish you all nothing but the best in your future endeavors.

Thanks also to Jessica Bickel, for being such a good friend and sounding board – despite not being a metallurgist - and for always trying to cheer me up when I've had a rough day.

To the University of Michigan – thanks for nine years and three degrees. I have grown so much since freshman year, and will always look back with fondness at my time here. Go Blue!

Last but certainly not least, thank you to my family. Mom and Dad, thank you for supporting me in my decisions and for always being there when I need you. Your love has made me the person I am today. And to my sister Tiffany, thank you for putting up with me all these years and for being my first (and best) friend.

Financial support for this work has been provided by the USAMP program and by the National Science Foundation FRG Grants No. F015408 and DMR-0309468. Support has also been provided by the Rackham Graduate School in the form of a Predoctoral Fellowship.

Table of Contents

List of Tables

List of Figures

Abstract

Magnesium alloys, with a lower density than steel or aluminum, have the potential to reduce the mass of automotive components. However, new alloys with improved creep resistance must be developed before Mg can be used for high temperature powertrain applications. Limiting the development of these alloys is the lack of fundamental knowledge of creep deformation in Mg alloys. This dissertation investigates the dependence of creep resistance on elemental partitioning during solidification, using thermodynamic modeling and experimental composition mapping. The effect of Sn additions on Mg-Al-Ca alloys is examined with respect to solute and precipitation strengthening, and the results are used to develop strategies for future alloy development.

Viscous glide of <a> dislocations in the α-Mg phase was determined to be the operative creep deformation mechanism through observation of dislocation substructures in crept samples. Thus, compositional and microstructural changes offer a pathway to improved creep resistance through solute and precipitation strengthening of the α-Mg phase.

Addition of 0.75-1wt% Sn to Mg-5Al-3Ca increased the Ca partitioning to the α-Mg phase during solidification and led to a higher average Ca concentration in the α-Mg by changing the phase free energy. Additions of greater than 1wt% Sn changed the solidification path, leading to lower Ca partitioning to the α-Mg. Increasing the local Ca concentration led to a greater decrease in minimum creep rate than a corresponding change in local Al concentration, indicating that the Ca concentration in the α-Mg phase contributes more to solute strengthening than the Al concentration. The lowest minimum creep rate was observed in Mg-5Al-3Ca-0.75Sn, which combined a high concentration of Ca in the α-Mg phase and increased Ca partitioning during solidification.

Precipitation strengthening accounts for a significant portion (20-50%) of the creep strength of Mg-Al-Ca alloys. Basal precipitates of Al_2Ca in α-Mg cells led to

modest increases in creep resistance. The Mg-5Al-3Ca-0.75Sn alloy had the smallest precipitate spacing and exhibited a minimum creep rate approximately two times lower than other Sn-containing alloys. Alloying additions should therefore be targeted that can increase both the local Ca concentration in the α-Mg and the volume fraction of Al_2Ca precipitates for improved creep resistance.

Chapter 1

Introduction

1.1 Motivation for the Use of Mg Alloys in Powertrain Applications

Magnesium alloys have become increasingly important in the automotive industry, because of their low density of ~1.7 g/cm^3. In comparison, aluminum has a density of ~2.7 g/cm^3 and steel a density of ~7.85 g/cm^3, making Mg ~4.5x less dense than steel and ~1.5x less dense than aluminum. Some components that were traditionally made of steel or aluminum can thus be replaced by lightweight magnesium components, resulting in a decrease in vehicle mass. This reduction in mass can lead to greater fuel economy and, correspondingly, a decrease in harmful emissions.

Traditionally, magnesium alloys have been used mainly for ambient temperature automotive applications including instrument panel beams, steering column components, transfer cases, valve/cam covers, and an assortment of housings and brackets [1]. The use of magnesium has been somewhat limited because of its low creep resistance above 125°C [1, 2]. To extend the use of magnesium alloys to powertrain applications, which typically operate in the temperature range of 150-200°C [1, 3], it is necessary to improve the creep resistance of current alloys or develop new alloys with higher creep resistance. According to Hines et al. [4], the creep resistance requirement for an engine block is < 0.5% creep strain after 500 h at 110 MPa and 150°C, and < 0.5% creep strain at 70 MPa and 100°C for an oil pan. This corresponds to an average creep rate of ~2.8×10^{-9} s^{-1}.

To better understand the challenges faced in designing creep-resistant alloys for powertrain applications, this chapter reviews alloy development efforts that provide a basis for our current understanding of the role of composition and microstructure on creep behavior in Mg alloys. Current understanding of deformation and strengthening mechanisms

pertinent to creep behavior are next reviewed and, finally, the objectives and methodology of this dissertation research are described.

1.2 Elemental Magnesium

To fully understand the Mg alloys that have been developed, it is important to first understand the properties of elemental magnesium. Magnesium has a hexagonal close-packed (hcp) structure, space group #194 ($P6_3/mmc$) [5], with lattice parameters a = 3.21 Å and c = 5.21 Å [5, 6] and thus a c/a ratio of 1.624 [7, 8]. This is a -0.5% deviation from the ideal c/a ratio of 1.633 [8], a small deviation compared with most other hcp metals, which can deviate as much as 15.5% (i.e. Cd). Correspondingly, Mg has smaller stacking fault energy than hcp metals with larger negative deviations from the ideal c/a ratio [9]. The atomic (metallic) radius of magnesium is 1.60 Å [10]. Pure Mg melts at 650°C [6, 10, 11], and has a room temperature Young's modulus of 45 GPa [6].

Five independent slip systems are necessary for homogeneous deformation without cracking, but the two most common slip systems in Mg offer only four independent modes [7]. In hcp materials, the preferred slip direction is $\langle 11\bar{2}0 \rangle$, which corresponds to the close-packed direction. The dominant slip plane varies according to the material. For Mg, this is the (0001) basal plane [8, 10-14], which is also the close-packed plane. The same is true for Cd, Zn, Co and Be, but for Zr, Ti and Hf slip on $\{10\bar{1}0\}$ prismatic planes [8, 12] is favored. The dominant slip plane is not determined by c/a ratio, but slip on prismatic planes is favored by transition metals with less than half their electronic d orbitals filled [8]. Some researchers have related dominant slip on prismatic planes to less than ideal c/a ratios, but Mg, Co and Be, which have c/a ratios of 0.5, 0.6 and 4% less than ideal, respectively, do not fit this trend and slip principally on basal planes [8]. At higher temperatures, more slip systems are activated, thus increasing the formability. For Mg, the secondary slip system is prismatic $\{10\bar{1}0\}\langle 11\bar{2}0 \rangle$ [8, 10, 11, 13, 15, 16]. Other possible slip systems include two pyramidal systems, first order $\{10\bar{1}1\}\langle 11\bar{2}0 \rangle$ and second order $\{11\bar{2}2\}\langle 11\bar{2}3 \rangle$ [8, 12-14]. The basal, prismatic and pyramidal planes are illustrated in Figure 1.1. Deformation can also occur by $\{10\bar{1}2\}$ tension twins [7, 11, 13], although this mechanism is not possible under c-axis

compression [13-15] since this twinning mode leads to expansion along the c-axis as the basal plane within the twin reorients until it is approximately 4° from the tensile axis [16]. Deformation by $\{10\bar{1}1\}$ compression twins or $\{10\bar{1}1\}-\{10\bar{1}2\}$ double twins [16-20] has also been reported.

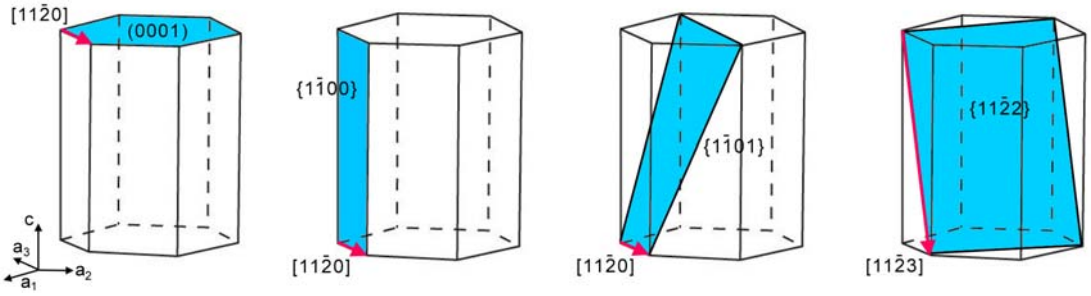

Figure 1.1 – Illustration of the major slip systems in Mg: a) basal, b) prismatic, c) 1st order pyramidal and d) 2nd order pyramidal. The slip direction is indicated in each figure.

The critical resolved shear stress (CRSS) will vary for each of the systems described, and ultimately determines which slip system will be active. The reported critical resolved shear stresses for Mg vary widely. For single crystals of pure Mg at room temperature, Burke and Hibbard measured a room temperature CRSS of 0.45 MPa for basal slip and 0.51 MPa for pyramidal slip [21]. Kelley and Hosford reported a CRSS of 0.48 MPa for basal slip, but the CRSS for prismatic slip was much higher, 39-52 MPa [22]. Akhtar and Teghtsoonian list values of 0.48MPa for basal slip [23] and 54MPa for prismatic [24] at room temperature. The CRSS generally decreases with increases temperature. According to Wonsiewicz and Backofen, the CRSS for prism slip decreases from ~110 MPa at room temperature to ~12 MPa at 270°C for polycrystalline Mg [16], indicating that slip on non-basal planes becomes easier as the temperature increases. At 330°C, the CRSS for pyramidal slip also decreases, to approximately 3.9 MPa according to Raynor [11]. Alloying additions can also change the CRSS. For Mg-4wt%Li, the critical resolved shear stress for prismatic slip decreased to 24 MPa at room temperature, suggesting that prismatic slip becomes easier with additions of Li [22]. Dilute additions of solute have been found to increase the CRSS for basal slip in single crystals [23], while the low temperature CRSS for prismatic slip decreased with additions of Zn, Al and Li [24]. The CRSS for basal slip is reported to increase with a $C^{1/2}$ or $C^{2/3}$ dependence, where C is the concentration of solute atoms [25].

Two main types of dislocations are observed in hcp materials, <a> type and <c+a> type. The <a> type dislocations have a Burgers vector of $\mathbf{b} = \frac{1}{3}\langle 11\bar{2}0\rangle$ and can glide on basal, prismatic or first order pyramidal planes. They are the most common type of dislocation observed [8, 11, 23]. Basal <a> dislocations can move to nonbasal (prismatic or pyramidal) planes via thermally activated cross slip [26]. The <c+a> type dislocations have a Burgers vector of $\mathbf{b} = \frac{1}{3}\langle 11\bar{2}3\rangle$ and glide on second order pyramidal planes [8, 12, 13, 17]. A third type of dislocation, <c> with a Burgers vector of $\mathbf{b} = [0001]$, can sometimes be found on $\{h\bar{k}i0\}$ planes [7].

1.3 Alloys Systems

Numerous alloy systems have been developed over the years to improve mechanical properties, including creep. Elements such as Al, Zn, Mn, Si, and Sn, as well as the rare earth and alkaline earth elements have all been used as alloying additions. Chemical composition can affect the microstructure, phases present and creep resistance of the alloy. Alloying elements are usually chosen with a specific purpose in mind, such as castability, room temperature strength, corrosion resistance, creep resistance, density or cost [27]. However, there are often competing demands at work. For instance, rare earth elements such as Gd can improve the creep resistance, but at an increased cost. Ca additions improve the creep resistance, but can lead to die-sticking or hot cracking during casting. Mn additions improve corrosion resistance, but have limited solubility in Mg. Elements like Al can increase room temperature strength, but have a negative effect on ductility and high temperature strength. For improved creep resistance, increased solute and precipitation strengthening is usually desired, but these other considerations must be kept in mind. Therefore, alloy compositions often represent compromises between improvement in one particular property and degradation in another.

The naming convention for most Mg alloys requires explanation before specific alloy systems are described in more detail. Mg alloys are named according to the major alloying elements used. A letter designation for each alloying element is listed first, followed by numbers representing the concentration (in wt%) of each element in order,

rounded to the nearest whole number. For example, AZ91 corresponds to an alloy with 9wt% Al and 1wt% Zn, with the balance being Mg. AXJ530 represents an alloy with 5wt% Al, 3wt% Ca and 0.15wt% Sr. Table 1-1 includes a list of the common alloying additions and their letter designations.

Table 1-1 - Designation of elements for the naming of Mg alloys [28]

Element	Designation
Aluminum	A
Bismuth	B
Copper	C
Cadmium	D
Rare Earth (e.g. Ce, La)	E
Iron	F
Thorium	H
Strontium	J
Zirconium	K
Lithium	L
Manganese	M
Nickel	N
Lead	P
Silver	Q
Chromium	R
Silicon	S
Tin	T
Calcium	X
Yttrium	W
Antimony	Y
Zinc	Z

1.3.1 Mg-Al-based Alloys

A large number of the creep resistant alloys that have been developed are based on the Mg-Al system. Al is added to increase the room temperature strength and castability, although a high Al level can also decrease the high temperature strength and ductility [28, 30, 31]. From the Mg-Al binary phase diagram, Figure 1.2, there is significant solubility of Al in Mg, up to 12.9 wt% Al at 437°C [29]. At 200°C, the equilibrium Al concentration is 2.9 wt% [30]. The Al concentration can vary across a grain or dendrite cell due to microsegregation during solidification. For example, in a directionally

solidified Mg-4Al alloy, Zhang et al. determined that the first material to solidify had an Al concentration of ~1.5 wt%, while the last to solidify had an Al concentration of ~9 wt%. This would correspond to the concentration of the core of the cell and the interdendritic region, respectively [31]. Elemental segregation is important to consider, since it can influence precipitation and creep at high temperatures, as will be discussed in more detail later. The primary intermetallic that forms in this binary system through a eutectic reaction at 437°C is the β-$Mg_{17}Al_{12}$ phase [1], which has a bcc structure [32] with the cI58 ($I\bar{4}3m$ or A12) space group [33, 34]. The presence of β phase is often associated with lower creep resistance. Multiple reasons have been proposed to explain this phenomenon, but the underlying mechanism is still under debate. It has been suggested [11, 35] that creep resistance in these alloys is reduced by softening of the beta phase at elevated temperatures. This in turn can lead to weakening of the grain boundaries as the beta phase softens [35]. However, Dargusch et al. [36, 37] note that β-$Mg_{17}Al_{12}$ does not markedly soften below 260°C, a temperature much higher than that normally experienced in powertrain applications. Instead, they suggest that the poor creep resistance of these alloys can be attributed to the discontinuous precipitation of β-$Mg_{17}Al_{12}$ in areas that had previously been regions of highly supersaturated α-Mg [36, 38]. During discontinuous

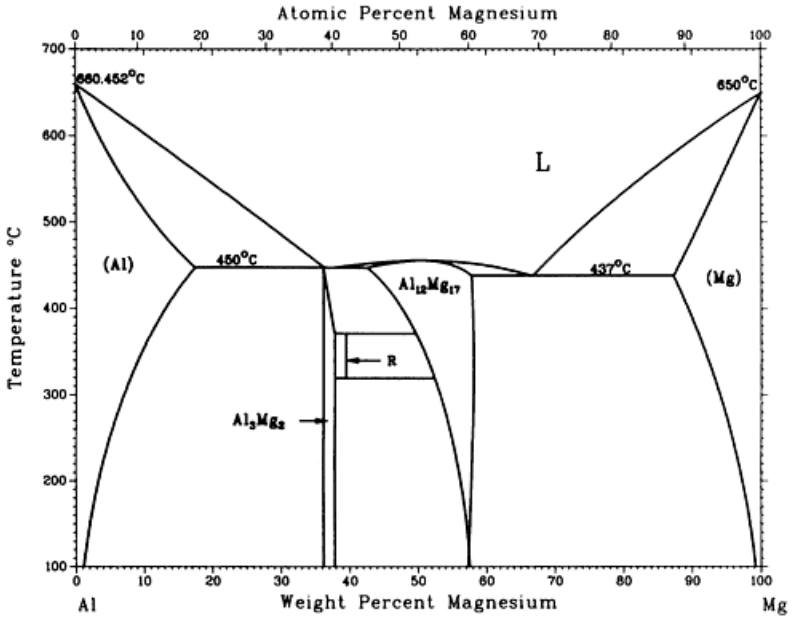

Figure 1.2- Binary Mg-Al phase diagram [33].

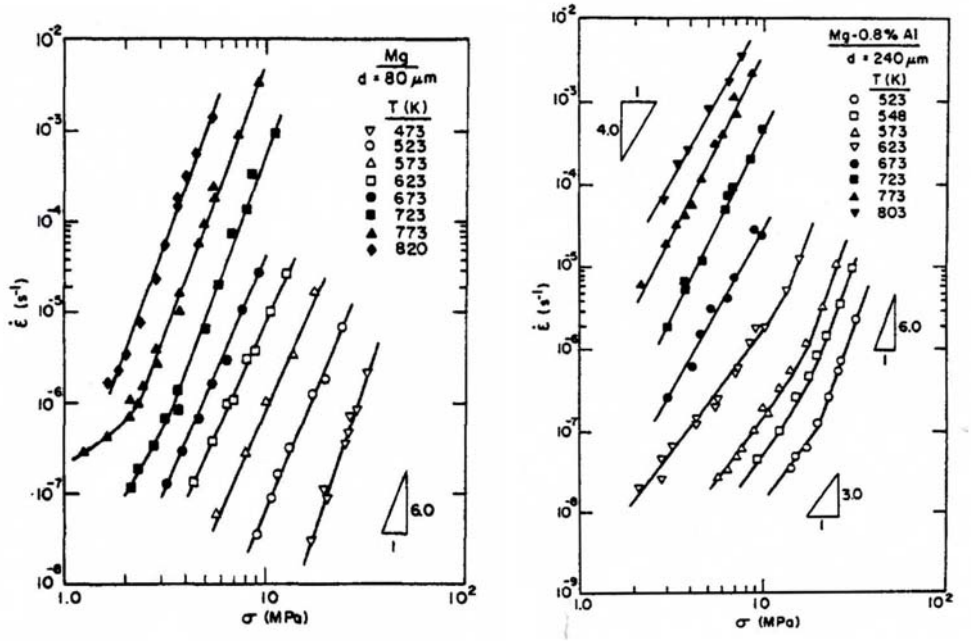

Figure 1.3 - Steady-state creep rate vs. stress for a) pure Mg [39] and b) Mg-0.8wt%Al [40].

precipitation, cellular growth of alternating layers of β and near-equilibrium Mg occurs at high angle boundaries [30]. This explanation is based on the argument that discontinuous precipitation provides more interfaces that allow for increased grain boundary sliding. Continuous precipitation can also occur within the α-Mg cells in areas that were supersaturated in Al. In this instance, the decrease in creep resistance has been attributed to rapid coarsening of these continuous precipitates due to their low melting point, which leads to decreased precipitation strengthening. Solute strengthening also decreases from the removal of solute from the α-Mg phase [41].

Pure Mg has a creep rate of ~10^{-7} s^{-1} when crept at 250°C and 10 MPa [39], while Mg-0.8Al has a creep rate one order of magnitude lower, ~10^{-8} s^{-1} at this temperature and stress [40]. The creep rate at other temperature and stress combinations for pure Mg and Mg-0.8Al are compared in Figure 1.3. The addition of 0.8wt% Al to pure Mg increases the creep resistance of the material. Neither material has acceptable creep resistance for automotive applications, however. Sato and Oikawa [42] studied creep at 600K in Mg-Al solid solution alloys, and found that creep rate decreased as the Al content was increased from 0.5 to 3 at%. They attributed this improvement in creep resistance to an increase in breakaway stress from solute atmospheres for gliding dislocations [42].

Recently, Dargusch et al. [37] have studied the effect of aluminum concentration on the mechanical properties and microstructure of die-cast Mg-Al binary alloys. The Al content was varied from 2-18 wt%, and the yield strength of the alloy was found to increase with increasing Al concentration, from 87 to 244 MPa respectively. Conversely, the ductility decreased with increasing Al content, from 19% to 0.7%. The amount of eutectic β-$Mg_{17}Al_{12}$ increased with increasing Al concentration, although the morphology of the β phase changed from fully divorced eutectic to partially divorced eutectic to "fibrous" eutectic. Supersaturated α-Mg was present in all the alloys and microstructure was morphologically unstable with creep testing at 150°C and 50 MPa. Continuous and discontinuous precipitation of β-$Mg_{17}Al_{12}$ occurred during creep [37]. During continuous precipitation, lath-shaped plates grow on the basal planes. These precipitates are responsible for most of the age hardening that occurs in Mg-Al alloys [30]. The creep rate was found to decrease with increased Al concentration. After 100 h at 150°C and 50 MPa, the creep strain measured for Mg-2Al was ~3.5%, while Mg-18Al had a creep strain of ~1.3%. Dargusch et al. attributed this improvement in creep resistance to an increase in solute Al in the primary α-Mg, since this would lead to an increase in continuous precipitation and also in solute strengthening. During continuous precipitation, thin plates of β-$Mg_{17}Al_{12}$ form parallel to the basal plane, which can inhibit creep in the α-Mg matrix until they coarsen too extensively. Interestingly, the increase in volume fraction of eutectic β-$Mg_{17}Al_{12}$ did not have a detrimental affect on the creep properties [37], supporting the theory that β phase instability is not the cause of reduced creep resistance in these alloys.

1.3.2 Mg-Al-Zn Alloys

One of the most common alloy systems based on Mg-Al is the Mg-Al-Zn system, whose liquidus projection is shown in Figure 1.4. Alloys such as AZ91D, AZ31 and AZ61 have been developed within this ternary system. As with the binary Mg-Al system, the predominant intermetallic phase present in these alloys is β-$Mg_{17}Al_{12}$, Figure 1.5, as long as the Al to Zn ratio is greater than 3:1. According to Spigarelli et al. [43], Zn is added to increase the solute strengthening of the alloy. The addition of zinc to binary Mg-Al decreases the amount of Al in solid solution in the primary α-Mg by increasing

the amount of precipitates that form during high temperature exposure [29]. The amount of Al in solid solution, as well as volume fraction and distribution of the β phase and α grain size, can also be affected by the processing route used [43, 44]. Continuous and discontinuous precipitation of the β phase from the primary α-Mg occurs after exposure to high temperatures, whether through aging [29, 32] or during creep [43]. The α-Mg in the region adjacent to the β phase is higher in Al content than the primary alpha in the center of the cell because of microsegregation during solidification. Dargusch et al. measured the Al content of the primary α-Mg in AZ91 with SEM-EDS and found an Al content of ~ 4 wt% in the center of the cell and over 11 wt% in the supersaturated region surrounding the β phase in the as-die-cast state [36]. Of course, the Al concentration of the primary alpha near the eutectic will decrease during high temperature exposure due to the precipitation processes mentioned above.

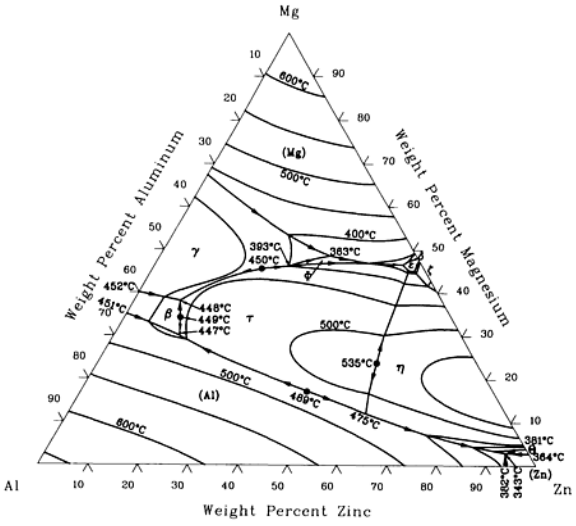

Figure 1.4 - Mg-Al-Zn liquidus projection [33].

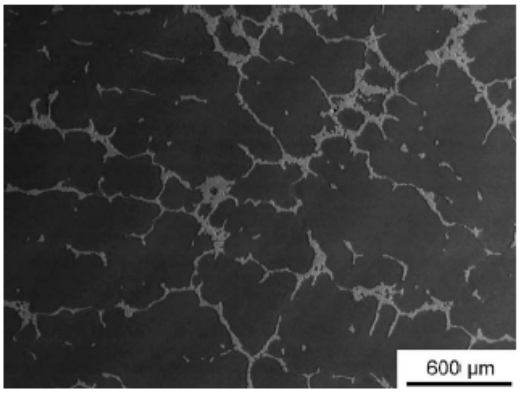

Figure 1.5 - Microstructure of AZ91 [45]. Dark contrast phase is primary alpha Mg, while lighter contrast phase is $Mg_{17}Al_{12}$.

The creep behavior of die-cast AZ91D has been characterized in multiple studies. Regev et al. [44] reported a minimum creep rate a few orders of magnitude lower than that of pure Mg at 150 and 180°C and stresses of 30-100 MPa. Stress exponents of ~5-7 were reported, and dislocation creep was identified as the operative mechanism [44]. Both basal and non-basal <a> type dislocations were observed via TEM [44, 46]. Dargusch et al. reported stress exponents of ~ 2 at low stresses, and that grain boundary sliding and migration were the dominant creep processes in this regime [36]. The creep strength as a function of temperature for 0.1% creep strain at 100 h for AZ91 is shown in Figure 1.6,

taken from Luo [1]. This figure also compares the creep strength of AZ91 to several other Mg alloys, which will be discussed later, and to Al alloy 380, which is often used in powertrain applications. The microstructure of as-cast AZ91 is not stable, and secondary β precipitates form during creep [46]. Dargusch et al. attributed the poor creep strength of die-cast AZ91 to the instability of the supersaturated regions of the α-Mg (i.e. near the interdendritic regions) at elevated temperatures, since discontinuous precipitation of β phase occurs in these regions during creep [36]. However, Regev et al. have reported that the higher the degree of Al supersaturation in the primary Mg, the lower the minimum creep rate, due to the possibility of precipitation and solute strengthening during creep in these alloys [46]. Thus, they suggest that a high level of Al in solution may be beneficial, which is supported by Suzuki et al., who reported that additions of Sr to Mg-Al-Ca alloys can increase the amount of Al in solid solution and strengthen the primary α-Mg [47]. Conversely, Dargusch et al. attribute the improved creep resistance of AS21 and AE42 (discussed in more detail later) to the lower volume fraction of supersaturated α-Mg in these alloys [36], at least in part. Together, these studies suggest that an optimum Al concentration may exist that is high enough for solute and precipitation strengthening, but low enough to limit discontinuous precipitation of the beta phase.

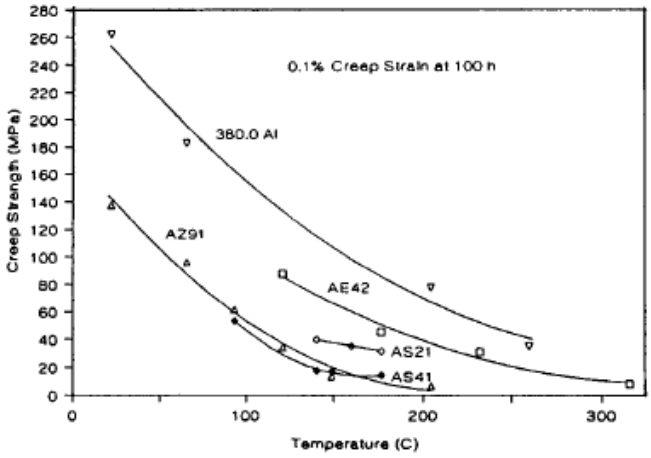

Figure 1.6 - 0.1% creep strength at 100 h for some common Mg alloys [1]. Al380 is included for comparison.

Alloys have also been developed that have zinc as the major alloying element with ternary additions of aluminum. An example of this is the alloy ZA85 [48]. ZA alloys have the typical dendritic microstructure with intermetallic compounds present in the

interdendritic regions. Areas of α-Mg solid solution highly supersaturated with Zn and Al are observed surrounding the intermetallic phase [49]. Depending on the composition, a number of intermetallic compounds are possible, including β-$Mg_{17}Al_{12}$, MgZn (ε phase), $Mg_5Zn_2Al_2$ (φ phase), and $Mg_{32}(Al,Zn)_{49}$, which is known as the τ phase [49, 50]. A metastable icosahedral quasi-crystalline phase has also been observed in some cast alloys, which transformed to the φ phase with homogenization at 325°C [51]. According to Vogel et al., the quasi-crystalline phase in ZA85 is stable at annealing temperatures of less than 200°C. They also observed the formation of continuous precipitates in the near-grain boundary regions at these temperatures [49]. Formation of β-$Mg_{17}Al_{12}$ is suppressed in most alloys with high zinc contents, and ZA alloys containing 4% Al were found to have a creep rate that was one-third that of AZ91 [52]. According to Zhang et al., the τ phase is the most effective at improving creep resistance [50].

1.3.3 Mg-Al-Mn Alloys

Another alloy system that has been developed for lower temperature applications is based on the Mg-Al-Mn ternary. Examples of alloys in this class are AM50 and AM60B. The latter alloy has been used for instrument panel (IP) beams in the automotive industry [15]. Mn is often added to improve the corrosion resistance by reacting with any iron impurities present [43]. Iron is soluble in the Al-Mn binary phases and can form $Al_8(Mn,Fe)_5$ [53], which in turn increases the stability of these phases [54]. Unlike Al, Mn has very limited solubility in Mg, even at elevated temperatures [55]. For alloys that contain 2-9 wt% Al and less than 1% Mn, the predominant intermetallic phase is β-$Mg_{17}Al_{12}$, present as a divorced eutectic in the interdendritic regions [55-57]. Additionally, coarse polygonal particles of Al_8Mn_5 are also present in the α-Mg cells [55, 58]. Mg-Al-Mn alloys have good ductility but lower strength than Mg-Al-Zn alloys [57] and during creep, fine elongated precipitates of β-$Mg_{17}Al_{12}$ form [55, 58].

The creep behavior of die-cast AM50 was studied by Ishimatsu et al. [56] at temperatures between 150 and 225°C and stresses between 20 and 120 MPa. The minimum creep rate occurred after one-third of the time to rupture, so the majority of the creep test was spent in tertiary creep under the conditions used. The stress exponent increased from ~5 at low stresses to ~10 at higher stresses above the yield stress of the

alloy. The yield strength was determined between 27-175°C at a strain rate of 2.5×10^{-4} s^{-1} [56]. Minimum creep rates ranged from 10^{-7} to 10^{-3} s^{-1} at 150°C, depending on the stress. This is higher than the 10^{-9} s^{-1} required for powertrain applications and therefore unacceptable for these components. Creep in AM50 was reported to be controlled by high temperature climb of dislocations on the basis of the strain exponent and activation energy calculated [56].

1.3.4 Mg-Al-Si Alloys

Mg-Si and Mg-Al-Si alloys have also been developed in order to reduce the amount of $Mg_{17}Al_{12}$ phase present. Examples of these alloys include AS41 and AS21. From the liquidus projection, Figure 1.7, Mg_2Si is expected to form in the interdendritic regions. Compared with $Mg_{17}Al_{12}$, which melts at 402°C [27], Mg_2Si has a high melting point, 1085°C [1]. Depending on Si concentration, two different Mg_2Si morphologies can exist: a "Chinese script" morphology for alloys with less than 1.14 wt% Si and a coarse blocky morphology at Si contents greater than 1.14 wt%. A small amount of β-$Mg_{17}Al_{12}$ was also present in high-pressure die-cast AS21 alloy, Figure 1.8. Areas of supersaturated Al-rich α-Mg were also observed along the grain boundaries and surrounding the intermetallic phases while lower Al concentrations were observed in the grain interiors [38]. Addition of a small amount of calcium (0.2-0.4 wt%) to Mg-Si alloys has been shown to modify the dendritic microstructure so that the Mg_2Si forms as finely dispersed round particles in a Mg matrix [1]. Carbonneau et al. reported that in addition to the rounded particles of Mg_2Si, a ternary MgSiCa phase with orthorhombic structure also formed in Mg-2Si and Mg-4Si with Ca additions greater than 0.8wt% [59]. The addition of 0.2-0.4wt% Ca did not improve the room temperature tensile strength of the alloys, although the ductility did increase [1]. The creep behavior of Mg-Si alloys modified with Ca has not been reported.

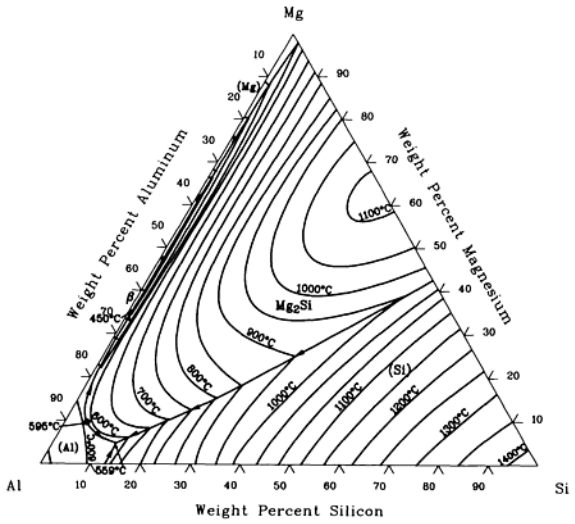

Figure 1.7 - Mg-Al-Si liquidus projection [33].

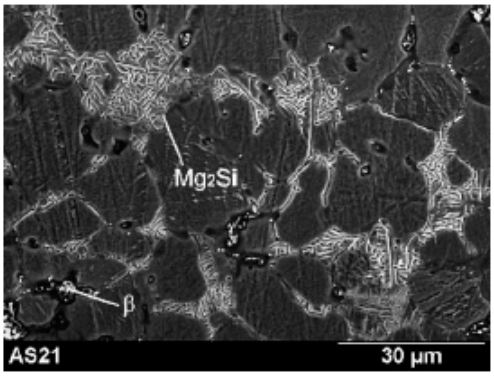

Figure 1.8 - SEM micrograph of die-cast AS21 with the eutectic compounds labeled [60].

Although Mg-Al-Si alloys have better creep resistance than AZ91D or AM50, their creep performance is still unacceptable for most powertrain applications. After 100h of creep at 150°C and 50 MPa, the creep rate for AS21 was ~ 10^{-9} s^{-1} [38]. According to Dargusch et al. [38], the creep resistance (as characterized by the creep rate after 100 hours at 150°C and 50 MPa) increases with increasing Si content up to 2.64 wt%. They have also reported that the microstructure of as-cast AS21 changes during elevated temperature creep testing. Discontinuous and continuous precipitation of β-$Mg_{17}Al_{12}$ were observed in areas adjacent to the grain boundaries, although a lower volume fraction of precipitates form compared to AZ91 [36]. Dargusch et al. suggested that the presence of the Mg_2Si particles accounted for improved creep resistance in these alloys compared to AM50 and die-cast AZ91D, where grain boundary sliding was

identified as the operative mechanism after observation of marker line offsets [36]. They argue that the particles help to both pin the boundaries, thereby increasing the resistance to deformation during grain boundary sliding, and inhibit the discontinuous precipitation of the beta phase [38]. This argument is based on the fact that no beta phase precipitation was observed at α/Mg_2Si boundaries during creep testing. When they compared the creep resistance of die-cast AM20 and AS21, which have similar levels of supersaturated α-Mg and β-$Mg_{17}Al_{12}$ and similar amounts of α-Mg, AS21 showed significant improvements in creep resistance. Their TEM results also indicated that branched Mg_2Si particles can extend into neighboring "grains", creating an "interconnected network of grains held together by the branched Chinese script Mg_2Si particles" [38]. It is not clear, however, whether these were truly separate grains, or just adjacent α-Mg cells from the same grain. There is also no direct evidence in this study that grain boundary sliding occurs without the particles.

1.3.5 Mg-Al-RE Alloys

Mg-Al-RE alloys (RE indicates rare earth additions) have shown potential for elevated temperature applications. Rare earth additions are often added in the form of La- and Ce-containing mischmetal, as in the case of AE42, AE21 and AE44 alloys. Elements such as Y and Nd have also been added independently, as in the case of WE alloys [57-60]. Alloys containing Gd have also been developed, but are typically limited to aerospace or automotive racing applications due to their higher cost [61, 62]. Microstructures of permanent mold cast ALa44 and ACe44 alloys are shown in Figure

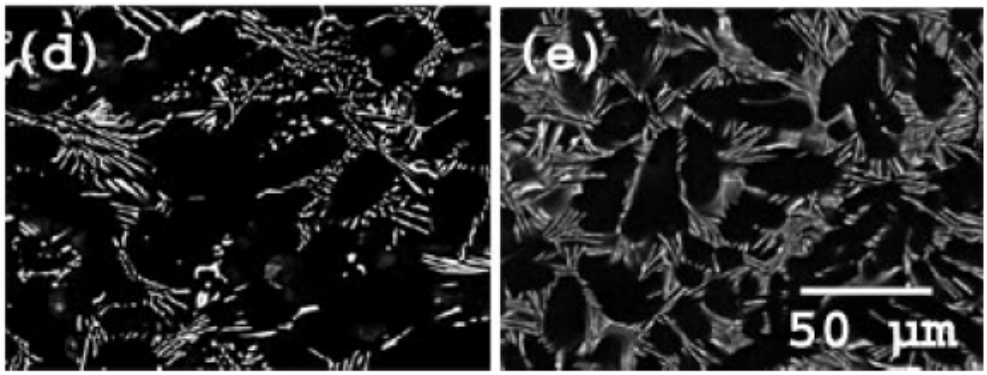

Figure 1.9 - SEM (BSE) micrograph of permanent mold cast d) Mg-4Al-4Ce and e) Mg-4Al-4La [63].

1.9. The 0.1% creep strength of AE42 is shown in Figure 1.6, and shows an improvement over AZ91 or AS21. For tensile creep tests conducted at 80 MPa, the minimum creep rate of squeeze-cast AE42 was calculated as 1.5×10^{-8} s^{-1} at 150°C, but it increased to 7×10^{-6} s^{-1} at 180°C [64].

The phases present in Mg-Al-RE alloys depend on the amount of rare earth added and the proportion of individual rare earth elements in the mischmetal. In AE42, the microstructure consists of dendrites of α-Mg surrounded by lamellar precipitates of predominantly $Al_{11}RE_3$ [65]. A small amount of Al_4RE (orthorhombic *Immm* [66]) and Al_2RE (diamond cubic $Fd\bar{3}m$ crystal structure [41]) may also be present, but the main eutectic phase is $Al_{11}RE_3$ [65, 67, 68], which has an body-centered orthorhombic (*Immm*) crystal structure [33, 69]. In AE44, Spigarelli et al. determined that the microstructure consists of primary α-Mg and Al_2RE as the major eutectic phase using SEM-EDS analysis [70]. Negligible amounts of Al, Ce and La were measured in solution in the primary phase using EDS [70]. Bakke and Westengen reported that if pure Ce is used instead of mischmetal to make ACe44, the primary eutectic phase that forms is $Al_{11}Ce_3$ ($Al_{11}RE_3$) [67] instead of the Al_2Ce (Al_2RE) that would be predicted from the work of Spigarelli et al. [70]. Bakke and Westengen were unable to explain why this difference exists. It is important to note that these observations come from SEM-EDS analysis. Although SEM-EDS can provide qualitative composition measurements, it cannot identify crystal structure. However, a recent study by Zhu et al. [69] using TEM diffraction identified $Al_{11}RE_3$ as the major eutectic phase in die-cast AE44, with minor amounts of diamond cubic Al_2RE also present. These conflicting results call into question the earlier studies of AE44, e.g. Spigarelli et al. [70] and Bakke and Westengen [67], which relied only on EDS analysis to identify the phases.

Some rare-earth-containing Mg alloys also show significant age-hardening responses, particularly those containing Gd [61, 62, 71, 72]. For an Mg-15Gd-0.5Zr alloy aged at 250°C for up to 500 hours, Gao et al. [61] observed four successive phases of precipitation, Figure 1.10. Two metastable phases, β″ and β′, coexisted in the matrix during the early stage of aging; precipitates of β′ grow, increasing the hardness rapidly, while precipitates of β″ diminish and disappear. Peak hardness occurs when the prismatic β′ plates form a triangular arrangement. These β′ plates have good thermal

stability at temperatures of 250°C for up to 50 hours. In the overaged stage, β_1 phase appears when β' decomposes. The β_1 phase then transforms to the equilibrium β phase. The hardness was found to increase by approximately 40 Hv in the peak aged condition. The addition of Y and Nd do not appear to change the precipitation sequence [61]. With lower Gd concentrations, the addition of Zn can increase the aging response significantly, and can also improve the creep strength over non-Zn-containing Mg-Gd-Zr alloys. The improvement in tensile and creep properties is associated with a uniform and dense distribution of basal plate precipitates not found in the Zn-free alloy [71].

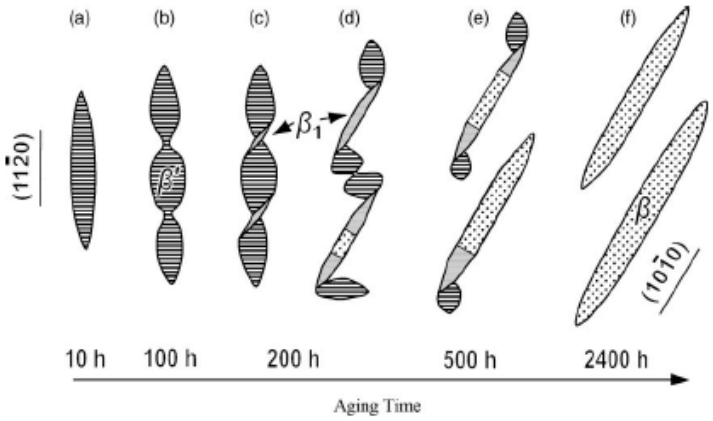

Figure 1.10 - Schematic of precipitation sequence in Mg-15Gd-0.5Zr aged at 250°C [61].

The microstructural stability of AE42 and MEZ at creep temperatures was studied by Moreno et al. [73]. For MEZ (Mg-1.92wt%RE-0.33Zn-0.26Mn), the initial microstructure was characterized by a semi-continuous grain boundary phase of $Mg_{12}RE$ intermetallic. Very little α-Mg was observed in the divorced eutectic of MEZ. After creep at 150°C for almost 600 hours, no microstructural changes were observed. AE42 (Mg-3.7Al-2.69RE-0.21Mn) had an initial as-cast microstructure that was characterized by a fine two-phase eutectic at the grain boundaries, which consisted of α-Mg and $Al_{11}RE_3$ intermetallic. After creep at 150°C for 600 hours, changes were observed in the near-grain boundary morphology. The lower creep resistance of AE42 compared to MEZ is attributed to the microstructural instability observed [73]. Powell et al. [65], Bakke and Westengen [67] and Spigarelli et al. [70] have also reported that the microstructure of AE42 is unstable at temperatures greater than 150°C due to the partial decomposition of the $Al_{11}RE_3$ phase into Al_2RE and Al, which can then form β-$Mg_{17}Al_{12}$. However, this view

has recently been contested by Zhu et al. [41], who concluded that the formation of β-$Mg_{17}Al_{12}$ is due to supersaturated Al in the primary α-Mg, not the breakdown of $Al_{11}RE_3$. In contrast, AE44, which has Al_2RE as the predominant eutectic phase, is more stable microstructurally at high temperatures and shows no difference in creep resistance for samples aged 500 hours at 175°C as compared to the as-cast state [67]. Following the logic of Bakke and Westengen, this improvement in creep resistance is due to the higher stability of the Al_2RE phase compared to the $Al_{11}RE_3$ phase. Using Zhu et al.'s reasoning the improved creep resistance can be attributed to a lower concentration of Al in solution in the primary alpha. The higher concentration of rare earth can react with more aluminum, removing the Al from solution and therefore inhibiting the formation of precipitates during the aging process. Thus, a more quantitative model of creep may be needed to resolve these differences.

1.3.6 Mg-Al-Sn Alloys

Alloys have also been developed that include tin. The combination of Al and Sn improves the castability of the Mg alloy by reducing the melting point without compromising strength [74]. Large additions of Sn can greatly increase the density of the alloy, however, and should therefore be avoided. The Mg-Al-Sn ternary phase diagram was recently calculated and published [74], Figure 1.11. For this system, no ternary phases were identified. There is also no significant ternary solubility in the system, i.e. Al is not soluble in the Mg_2Sn phase or Sn in the $Mg_{17}Al_{12}$. A very small Mg primary phase field exists, while the Mg_2Sn primary phase field is large. A ternary miscibility gap also exists in this system [74]. While this system may be important for development of quaternary alloys, few papers have been published on the ternary Mg-Al-Sn system [75, 76].

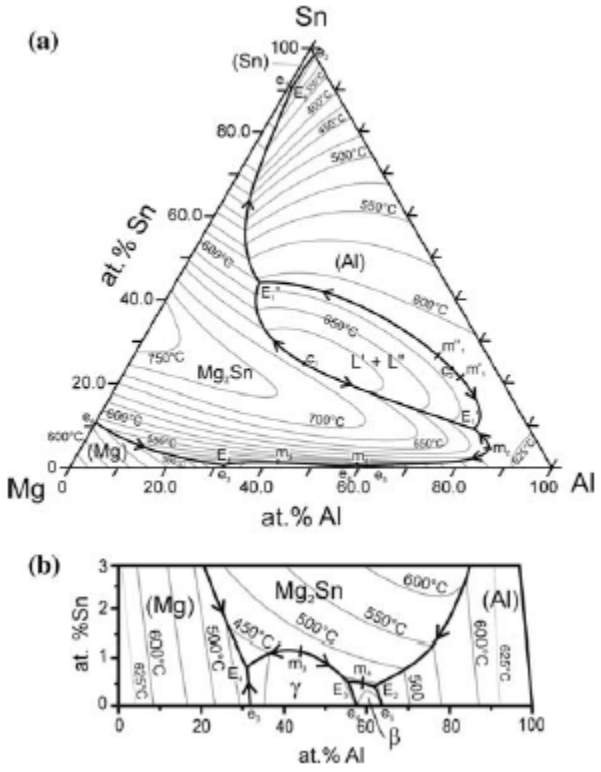

Figure 1.11 - a) Liquidus projection for the Mg-Al-Sn system, as calculated by Doernberg et al [74]. b) Magnification of the Mg-Al side of the projection.

Mg-Sn and Mg-Sn-Ca alloys have also been developed, which do not contain Al and therefore no β-$Mg_{17}Al_{12}$ phase. Instead, Sn was selected as the major alloying element due to its high solubility in Mg over a wide temperature range and the possible formation of the Mg_2Sn intermetallic phase. Sn is also reported to improve the corrosion resistance of the alloys when used as a major alloying element [77]. Zr can also be added to these alloys for grain refinement, which is not possible with Al-containing alloys [78]. Alloys such as Mg-3Sn-2Ca (TC32), TC22 and TC42 have been investigated [79]. Typical dendritic microstructures were observed for this family of alloys. The presence of both Mg_2Ca and a ternary CaMgSn phase has been reported in the interdendritic regions based on the results of XRD analysis [79]. A liquidus projection was recently calculated by Kozlov et al., Figure 1.12, where the major phases fields are identified as Mg, Mg_2Sn, Mg_2Ca, CaSn, $CaSn_3$, Ca, Sn and $Ca_{2-x}Mg_xSn$ (or CaMgSn) [80]. The CaMgSn phase is stable up to 500°C, and TEM diffraction analysis indicates that it has a primitive orthorhombic structure [81]. The formation of Mg_2Sn is suppressed when there

is excess Ca present, at levels of 1 wt% Ca or greater [33, 34, 36]. Kozlov et al. report that the presence of either Mg_2Ca or Mg_2Sn depends on the Sn/Ca ratio; a critical transition occurs at a Sn/Ca ratio around 3-3.5:1. Alloys with a Sn/Ca ratio lower than this will contain Mg_2Ca instead of Mg_2Sn [78], which is illustrated for an Mg-2Sn-2Ca alloy in Figure 1.13. The CaMgSn phase was present in two different morphologies in the alloys prepared by Kim et al. [81]: coarse laths in the grain interiors, and "feather-like" in the interdendritic regions. As the Ca content in the alloy increased, the coarse laths changed to a blocky morphology [81]. TC alloys have higher creep rates than AE42 at temperatures above 135°C [79]. Kim et al. noted that alloys containing above 2 wt% Ca show an improvement in creep properties compared to alloys with low levels of Ca, which contain the Mg_2Sn phase [81]. Hort et al. reported that the needle-like precipitates of CaMgSn found on both the grain boundaries and in the grain interiors are responsible for the improved creep properties compared to AZ91 [82].

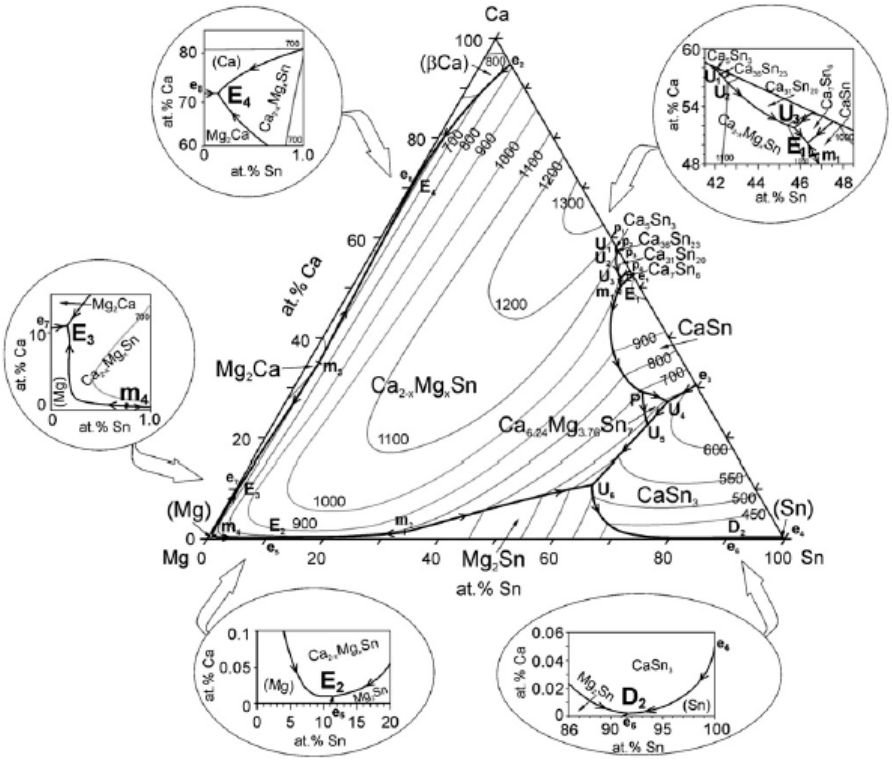

Figure 1.12 - Liquidus projection for the Mg-Ca-Sn system, as calculated by Kozlov et al [80].

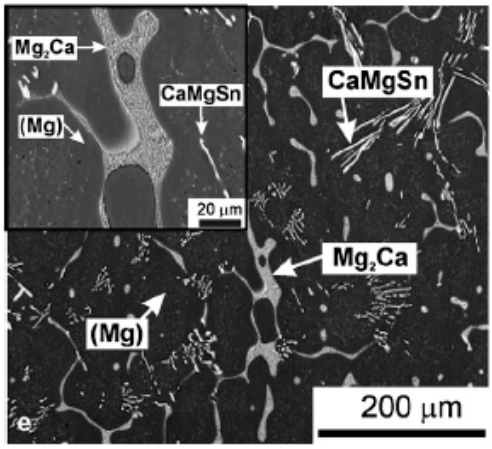

Figure 1.13 - (BSE) micrograph of Mg-2Sn-2Ca [78]. Inset is a magnification of the eutectic region.

1.3.7 Mg-Al Alloys Containing Alkaline Earth Elements

Many of the alloys developed for higher temperature applications contain ternary and often quaternary additions of alkaline earth elements such as Ca and Sr. These include alloys such as AX53, AJ62, General Motors' AXJ530 [83, 84] and Dead Sea Magnesium's MRI153M and MRI230D [85, 86]. Ca-containing alloys may be prone to die sticking or hot cracking, although Ca levels above 2% can significantly reduce these problems [1, 84].

The microstructure of Mg-Al-Ca alloys is characterized by cells of primary α-Mg surrounded by eutectic phases in the interdendritic regions. Depending on composition, several intermetallic eutectic phases may form, as shown in the liquidus surface in Figure 1.14, developed experimentally by Suzuki et al. [87] and confirmed computationally by Cao et al. [88]. These intermetallic phases include Mg_2Ca with a C14 structure, $(Mg,Al)_2Ca$ with a dihexagonal C36 structure [89], and β-$Mg_{17}Al_{12}$ (A12). The micrographs in Figure 1.15 illustrate the various eutectic compounds that may form as the amount of Al is increased. The C36 phase is a high temperature phase and can decompose into Mg_2Ca (C14) and Al_2Ca (C15) below 500°C [87]. All the intermetallic phases have significant ternary solubility [87]. Although earlier studies identified the eutectic phase as Al_2Ca [2, 90], it has been confirmed that $(Mg,Al)_2Ca$ is actually the phase that forms upon solidification [1, 89, 91]. The C36 phase is more stable morphologically than C14 or β-$Mg_{17}Al_{12}$ during annealing, since it is more resistant to coarsening, which can in turn increase the creep resistance [91]. For most Mg-Al-Ca alloys of engineering interest, i.e. those having approximately 4-6 wt% Al, the formation of β-$Mg_{17}Al_{12}$ is

suppressed. For alloys containing 3 wt% Ca, β phase formation occurs only when the Al concentration is greater than 11 wt% [47]. AX alloys were reported to have one order of magnitude improvement in creep resistance over AZ91 and a performance equal to or better than AE42 at 150°C, when creep extension (% strain) was used as the measure of creep resistance [2]. AX alloys are superior to AE42 at temperatures of 175°C, however, and adding even 0.1% Sr to these alloys can further improve the creep resistance [1, 92]. Luo and Powell have reported that grain boundary sliding at low stresses and dislocation-controlled creep at high stresses are the operative mechanisms for Mg-Al-Ca alloys based on the stress exponents measured [92]. However, in his study of permanent mold and die-cast AXJ530, Saddock saw no evidence of shearing along grain boundaries for stresses between 40-100 MPa and thus concluded that grain boundary sliding was not an operative creep mechanism in this alloy under creep conditions pertinent to automotive applications. [63].

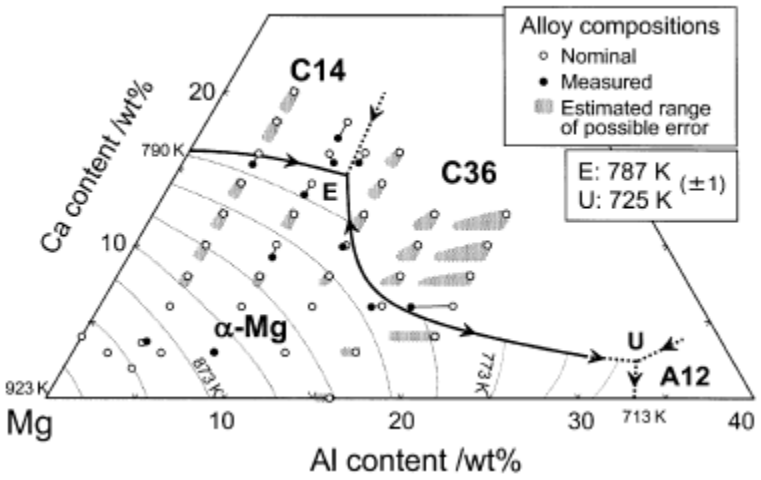

Figure 1.14 - Liquidus projection of the Mg-rich corner of the Mg-Al-Ca system, as determined experimentally by Suzuki et al [87].

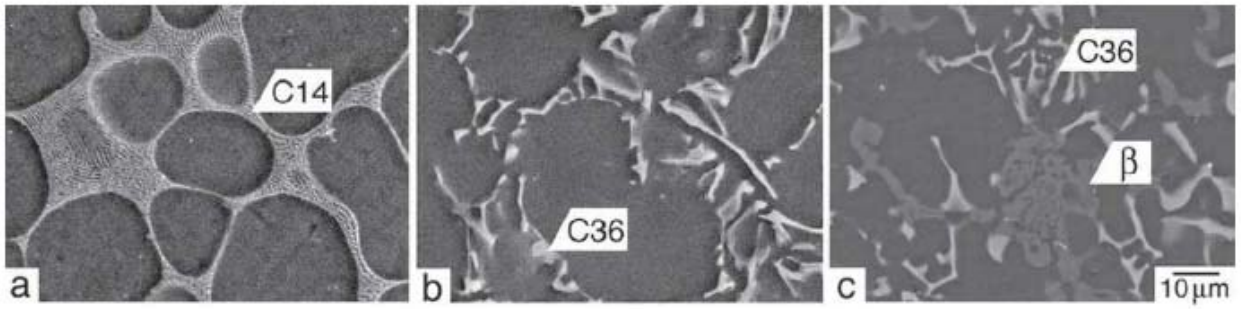

Figure 1.15 - SEM (BSE) micrographs of as-cast Mg-Al-Ca alloys: a) Mg-1.8Al-1.8Ca, b) Mg-7.4Al-1.9Ca and c) Mg-14.8Al-1.9Ca [91].

In Mg-Al-Sr alloys such as AJ51, AJ52 and AJ62, no β-$Mg_{17}Al_{12}$ phase was observed, which according to Luo [1] explains the improved creep resistance of these alloys. Low Al supersaturation was reported in the Mg matrix surrounding the second phase particles [1, 2]. In their study of quaternary additions of Sr to Mg-Al-Ca alloys, Suzuki et al. [82, 83] observed two types of intermetallic phases in an Mg-5Al-3Sr ternary alloy, Figure 1.16, which were identified through selected area diffraction patterns (SADP) in the TEM. A blocky semi-continuous compound with medium contrast was identified as the $Mg_{17}Sr_2$ phase with a hexagonal structure, while the lamellar type compound with bright contrast was identified as Al_4Sr with a tetragonal structure [93]. The semi-continuous blocky phase was also reported in other investigations [2, 90], where it was identified as an unknown ternary Mg-Al-Sr phase, although Suzuki et al. report that the blocky phase is $Mg_{17}Sr_2$ with solid-solubility of Al [93]. A calculated liquidus projection has been published by Cao et al. [94], Figure 1.17, which supports the phases observed by Suzuki et al [93, 95]. The creep resistance of AJ52 and AJ62 was reported to be better than AS21 and AZ91 and comparable to AE42 at 150°C. However, at temperatures above 150°C, AJ52 had superior creep resistance to even AE42 [95]. According to Pekguleryuz and Baril [2], this improvement in creep properties was due to the low supersaturation of Al in the α-Mg and subsequent suppression of discontinuous β-$Mg_{17}Al_{12}$ precipitates.

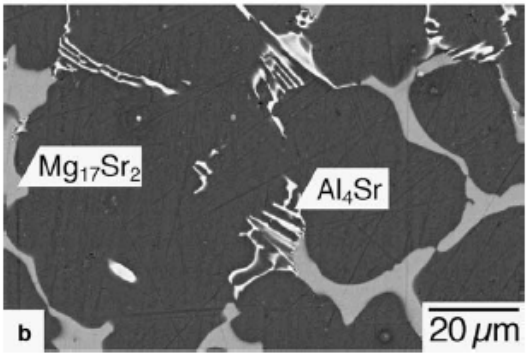

Figure 1.16 - SEM (BSE) micrograph of as-cast Mg-5Al-3Sr [96]. Dark contrast regions are primary Mg, while eutectic compounds are labeled.

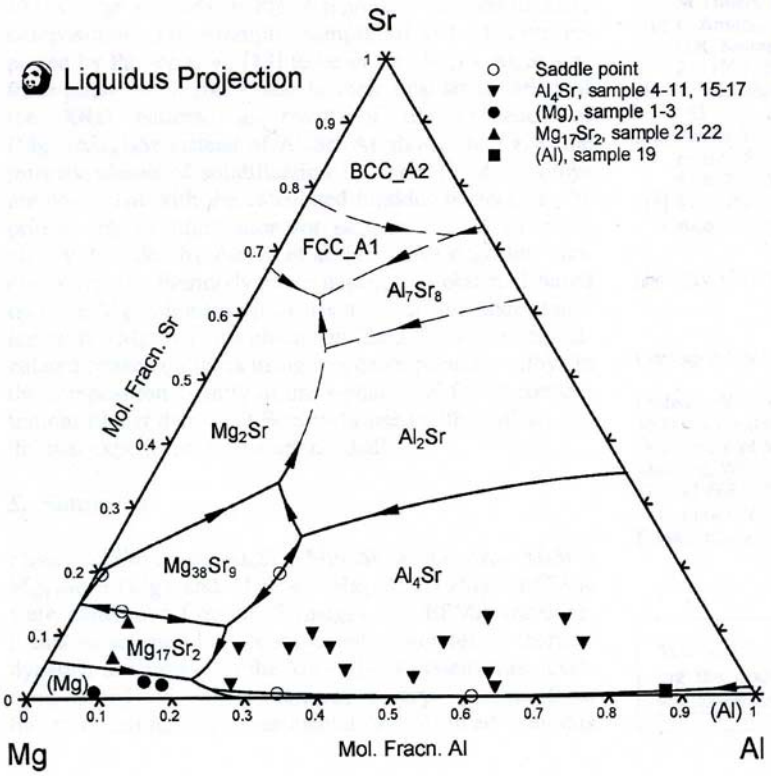

Figure 1.17 – Liquidus projection for the Mg-Al-Sr sytem, calculated by Cao et al [94].

1.4 Creep Mechanisms

Three stages of creep exist: primary, secondary and tertiary. During primary creep, the strain rate is initially high but slows over time due to strain hardening. During secondary creep, the creep rate remains relatively constant and may reach a steady-state or minimum level. Finally, the creep rate again accelerates due to damage accumulation during tertiary creep [97]. The mechanisms responsible for steady state creep are described in this section. Three major categories of creep mechanisms will be discussed – diffusional creep, grain boundary sliding and dislocation creep.

1.4.1 Diffusional Creep

Because diffusional creep is not expected to predominate under conditions relevant for powertrain applications, it will only be described briefly. Diffusional creep operates mostly at high temperatures and low stresses [98]. In this region, creep is controlled by the rate of the diffusional transport of atoms which results in a macroscopic

change in shape [99]. Within a grain, atoms will flow away from boundaries where compressive stresses exist and towards boundaries with tensile stresses [98], as illustrated by Figure 1.18. Vacancies will flow in the opposite direction [100, 101]. Microstructural evidence of diffusion creep includes denuded (precipitate free) zones formed by long range diffusion in the matrix [100, 101], although Vickers and Greenfield [102] and Ruano et al. [103] argue that this alone is not proof of diffusion creep in a hydrided Mg-Zr alloy . According to Langdon, offsets occur in marker lines as grains become elongated during diffusion creep, but the grains retain their relative positions [100], illustrated in Figure 1.19.

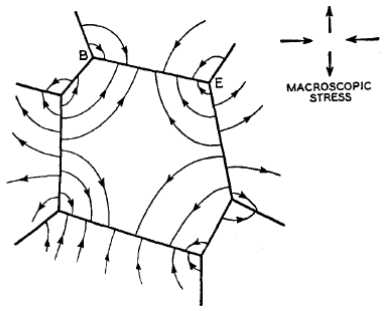

Figure 1.18 - Illustration of self diffusion currents in a grain undergoing Nabarro-Herring creep [98].

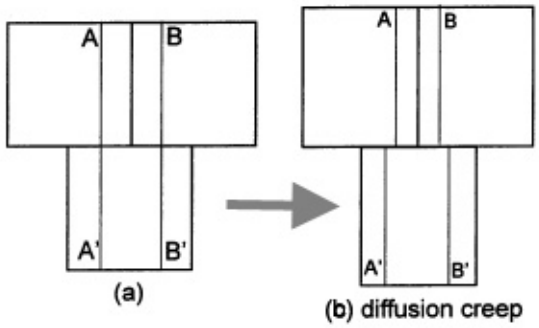

Figure 1.19 - Illustration of the effects of diffusion creep. Marker lines AA' and BB' become offset after creep, but although grains A and B become elongated, they do not shift relative position [100].

If the strain rate is controlled by diffusion through the lattice, it is known as Nabarro-Herring creep [98], and can be described by the following constitutive equation:

$$\dot{\varepsilon} = \frac{D_l \sigma b^3}{kTd^2} \qquad (1.1),$$

where D_l is the lattice self-diffusion coefficient, σ is the applied stress, b is the Burgers vector, k is Boltzmann's constant, T is temperature, and d is the grain diameter. If the

rate is controlled by grain boundary diffusion, on the other hand, it is known as Coble creep [99]:

$$\dot{\varepsilon} = \frac{aD_{gb}\sigma b^4}{kTd^3} \quad (1.2),$$

where D_{gb} is the grain boundary diffusion coefficient, a is a material constant, and the other symbols are the same as in Equation (1.1). The creep constitutive law is more generally described by the Mukherjee-Bird-Dorn equation:

$$\dot{\varepsilon} = \frac{ADGb}{kT}\left(\frac{b}{d}\right)^p\left(\frac{\sigma}{G}\right)^n \quad (1.3),$$

where A is a constant, G is the shear modulus, n is the stress exponent, and p is the grain size exponent [100, 104]. The appropriate diffusion coefficient (lattice or grain boundary) can be substituted for D, depending on the operative mechanism. The temperature dependence of the diffusion coefficient is:

$$D = D_0 \exp(-Q/(RT)) \quad (1.4),$$

where the activation energy for diffusion is Q. Typically, $n = 1$, and p is 2 (Nabarro-Herring) or 3 (Coble creep) [100].

1.4.2 Grain Boundary Sliding

Grain boundary sliding (GBS), defined as the displacement that occurs when two grains slide relative to each other in response to an external applied stress, is another mechanism that has been identified at low stresses [100]. The movement takes place at or near the grain boundary. Two types of grain boundary sliding mechanisms, Rachinger and Lifshitz, have been identified. Liftshitz sliding occurs exclusively in Nabarro-Herring or Coble creep. Here, grain boundary offsets develop as a direct result of vacancy diffusion under stress. During Rachinger sliding, the grains retain their original shape but become visibly displaced from each other. There is a net increase in the number of grains lying along the tensile axis. In a polycrystalline material, this is usually accommodated by limited dislocation slip within the grains [100, 101]. Equation (1.3) can again be used to characterize the creep rate during GBS where n~2 [39, 91, 105].

Grain boundary sliding is often inferred post-creep from offsets of scribed or FIBed marker lines on the surface of the specimen [36, 104-106], as illustrated in Figure 1.20

for AZ31. Ishida et al. also made internal measurements of grain boundary sliding in pure Al using a layer of finely dispersed oxide particles within a specimen made by press-bonding two pieces of aluminum [105]. In other instances, the operation of grain boundary sliding is inferred from calculated stress exponents [92].

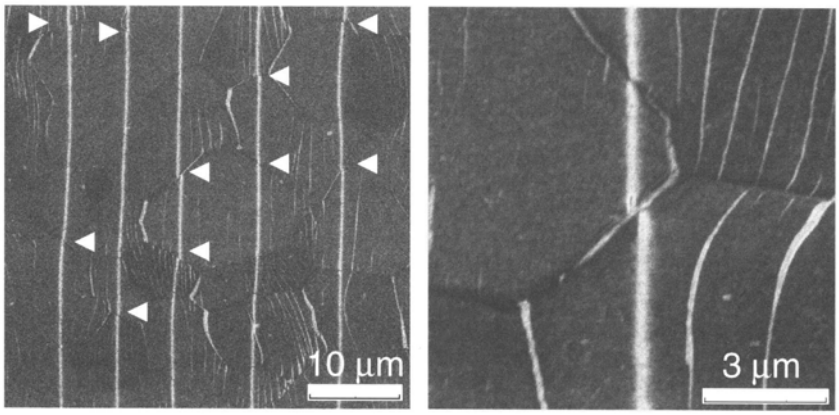

Figure 1.20 - Offset of FIB marker lines (marked by arrows) in AZ31, reported as evidence of grain boundary sliding. The image on the right is a magnified view of one of the offsets [106].

The presence of grain boundary sliding in Mg alloys is still under debate. GBS has been reported to contribute as much as 80% of the total creep strain of Magnox AL 80 alloy (Mg-0.8wt%Al) [107, 108]. Kottada and Chokshi have measured the contribution of grain boundary sliding to both diffusion and dislocation creep in a Mg-0.7wt%Al alloy, and have reported that GBS contributes significantly to diffusion creep (~75%) but much less during dislocation creep (~15%) [104]. Saddock investigated creep deformation in permanent mold and die-cast Mg-Al-Ca alloys through a strain-mapping technique and concluded that GBS is not operative under the stress and temperature level studied, 40-100 MPa at 175°C [63], which is relevant for automotive powertrain applications. Yet, grain boundary sliding was speculated to be the operative creep mechanism in earlier studies of this alloy [92]. Similarly, Vogel et al. detected no sign of grain boundary sliding in die-cast ZA85 crept at 20-125 MPa at temperatures between 150 and 210°C. Instead, they conclude that dislocation creep controls the deformation under these conditions, and that behavior is strongly influenced by microstructural stability [48]. Blum et al. have also reported that there is no need to invoke grain boundary sliding for creep of AZ91 at low strains. Instead, they propose that dislocation motion controlled by solute atoms is the operative mechanism in this regime [109].

1.4.3 Dislocation Creep

Dislocation creep in magnesium is usually attributed to three main mechanisms: viscous glide, dislocation climb and thermally activated cross-slip. All three operate in different temperature and stress regimes, although the transition is not always clear.

Vagarali and Langdon have identified viscous glide of basal dislocations as the operative creep mechanism at lower temperatures (up to 600-750 K) and lower normalized stresses in an Mg-0.8%Al solid solution alloy. They report that the activation energy is independent of stress and equal to that of interdiffusion of Al in Mg. Instantaneous strain was small or not measurable, and a very brief normal or inverted primary creep stage was observed, with stress exponents of ~3. Microstructurally, there was evidence of extensive basal slip, and the substructure consists of dislocations randomly distributed, Figure 1.21a. Dislocation motion in this regime is restricted by the presence of solute atmospheres [40]. Solute atoms create strain in the lattice that depends on the size difference between the solute and the matrix atoms. Solute atoms thus migrate to dislocations to relieve some of this strain and form solute "atmospheres", as described by Cottrell [110]. For the dislocation to move under an applied force, the dislocation must either break free of the solute atmosphere or drag it along. The dislocation velocity in this latter case is thus limited by the diffusion rate of the solute. The non-symmetrical distribution of solute atoms around a moving dislocation causes a perturbation force to act on the dislocation in the opposite direction of the applied force, resulting in a viscous drag that increases as the velocity of the dislocation increases. Only with the application of stresses greater than the atmosphere binding force will dislocations be able to break away from the solute atmospheres and move quickly through the material [110, 111].

At lower temperatures and higher normalized stresses, Vagarali and Langdon report that creep occurs by dislocation climb as the dislocations break away from their solute atmospheres. The activation energy for steady state creep is the same as that observed for viscous glide, and a measurable instantaneous strain is reported. Extensive primary creep is observed, and the stress exponent is ~6. Furthermore, the substructure consists of well-defined subgrains, as shown in Figure 1.21b [40]. During dislocation

climb, dislocations circumvent obstacles by the nucleation and motion of jogs [112], aided by the creation or destruction of vacancies [113]. A jog in the dislocation develops at either end of a row of vacancies, and these double jogs grow apart as more vacancies are added during the climb process. Climb can also occur through interstitials instead of vacancies [114, 115].

Finally, at higher temperatures, creep deformation in Mg alloys has been attributed to thermally activated cross-slip of basal dislocations to prismatic or pyramidal planes. Once again, there is a measurable instantaneous strain and a normal primary stage of creep, although the activation energy reported is much higher than with the other two mechanisms. The activation energy was also found to decrease slightly with increasing stress. Stress exponents of ~4 were observed. The microstructure is characterized by extensive non-basal slip and the substructure consists of free dislocations with isolated but well-defined sub-boundaries, Figure 1.21c [40].

Table 1-2 summarizes a sampling of the proposed creep mechanisms for Mg reported in the literature. Note that in some cases multiple mechanisms for a given alloy system have been proposed. For example, the creep of AZ91 has been attributed to grain boundary sliding [36] and dislocation climb [43] for the same general stress and temperature regime. Dislocation creep is the most common mechanism identified in the literature, especially dislocation climb. However, many of the studies have identified the operative creep mechanism from stress exponent and activation energy calculations alone, without characterizing the resulting dislocation substructures. The few studies that have incorporated observation of dislocations after creep deformation report evidence of basal and non-basal dislocations.

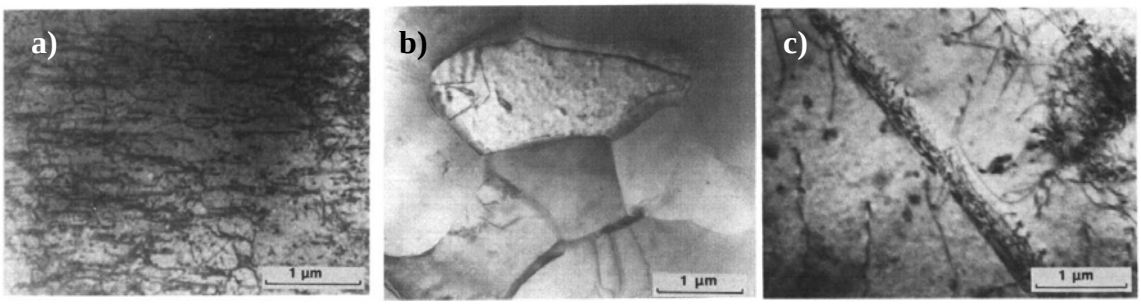

Figure 1.21 - Dislocation substructures observed by Vagarali and Langdon for an Mg-0.8Al alloy [40]: a) free dislocations, b) subgrains and c) sub-boundary.

Table 1-2 - Creep mechanisms reported in the literature for Mg alloys

Alloy	Processing method	Temperature	Stress	Mechanism	Ref
AE42	Squeeze cast	150-240°C	40-120 MPa	Dislocation glide and climb	[64]
AE42	Die-cast	150°C	20-80 MPa	Grain boundary sliding	[36]
AJ52, AZ91 and AS21	HPDC	135-190°C	40-240 MPa	Basal glide (supplemented by nonbasal glide and twinning)	[109]
AM50	Die-cast	423-498 K	20-120 MPa	Dislocation climb	[56]
AS21	Die-cast plate	70-150°C	75-250 MPa	Dislocation climb	[60]
AS21	Die-cast	150°C	20-80 MPa	Grain boundary sliding	[36]
AZ31, AZ61, AZ91	Annealed sheet	473-623K		Dislocation climb	[116]
AZ61	Hot rolled plate	250-346°C	0.9-4 MPa	Diffusion creep	[117]
AZ91	Thixoformed	120-180°C	30-100 MPa	Dislocation climb	[118]
AZ91	Die cast, ingot cast, thixoformed	70-200°C	30-300 MPa	Dislocation climb	[43]
AZ91	Die-cast	150°C	20-80 MPa	Grain boundary sliding	[36]
AZ91D	Rheocast	150-180°C	40-100 MPa	Dislocation climb	[119]
AZ91D	Die-cast	150-180°C	30-100 MPa	Dislocation motion on basal and non-basal planes	[44]
AZ91D	Cast ingots	120-180°C	40-115 MPa	Dislocation motion on basal planes and cross-slip	[120]
Mg	Powder metallurgy	400-800K	1-10 kg/mm^2	non-conservative motion of jogs on screw dislocations gliding on basal plane (high stress); cross slip from basal to pyramidal (low stress)	[121]
Mg	Extruded	473-820 K	2-30 MPa	Dislocation glide (low temp); Cross-slip (high temp,); Nabarro-Herring (high temp, very low stress)	[39]
Mg-(0.5,1.3%)Al	Extruded	600-650 K	3-50 MPa	Viscous glide	[42]
Mg-(0-4.4wt%)Zn	Hot pressed powders	150°C	30-50 MPa	Dislocation climb	[122]
Mg-0.8Al	Extruded	473-810 K	2-30 MPa	Viscous glide (low temp, low stress); Dislocation climb (low temp, higher stress); Cross-slip (high temp)	[40]
Mg-4Y-3RE	Heat Treated (T6)	423-523 K	30-300 MPa	Dislocation climb	[123]

Mg-Al-Ca (+Si or Sr)	Die-cast	150-200°C	56-83 MPa	Grain boundary sliding (low stress), dislocation glide (high stress)	[92]
Mg-Sc	Squeeze cast	200-350°C	30-80 MPa	Dislocation interactions with precipitates	[124]
Mg-Y	Heat Treated Plate	550–650 K	4–200 MPa	Cross-slip	[125]
Mg-Y	Heat Treated Plate	550K	50-200 MPa	Forest dislocation hardening and dynamic precipitation on dislocations	[126]
MRI153 (Mg-Al-Ca)	Squeeze cast, die-cast, ingot cast	150-200°C	30-120 MPa	Dislocation climb (low stress), power law breakdown (high stress)	[127, 128]
ZA85	Die-cast (as-cast and aged)	150-210°C	20-125 MPa	Dislocation creep	[48]
ZA85+Ca	Die-cast	150-200°C	20-100 MPa	Dislocation creep	[129]

1.5 Methods to Improve Creep Resistance in Mg Alloys

An analysis of available literature indicates several potential alloying and processing approaches to improve creep resistance in magnesium alloys. One approach focuses on strengthening the interdendritic regions by improving their stability. Phases that soften or weaken at high temperatures lead to increased deformation during creep, through increased grain boundary sliding or dislocation activity. By reducing the amount of less-desirable phases (especially β-$Mg_{17}Al_{12}$) or eliminating them entirely, the creep resistance should increase [1, 130]. This is often accomplished by adding alloying elements that form different intermetallic phases. As an example, by adding calcium to Mg-Al binary alloys, the amount of β-$Mg_{17}Al_{12}$ phase is reduced by the formation of $(Mg,Al)_2Ca$, Mg_2Ca or Al_2Ca [87]. Strengthening the eutectic phases or changing their crystal structure can also help to pin the grain boundaries, which is reported to reduce grain boundary sliding during creep [1, 85, 125]. However, as discussed in Section 1.3.1, β-$Mg_{17}Al_{12}$ is not expected to soften at temperatures below 260°C. Furthermore, direct evidence of grain boundary sliding is lacking for many Mg alloys, as mentioned in Section 1.4.2. Thus, the validity of this approach must be questioned.

Another method of improving creep resistance focuses on strengthening primary α-Mg by increasing the resistance to dislocation motion usually by precipitation or solid-solution strengthening [1], which Saddock suggests are the most effective methods to

improve creep resistance in cast Mg-Al alloys [63]. It can be difficult to distinguish between the two strengthening mechanisms at times, since increasing the amount of solute can also lead to an increase in precipitation. As described earlier, solute atoms which strain a crystal lattice, i.e. those with a size misfit, will migrate to the dislocations and form solute "atmospheres" around them [110]. According to Mohamed and Langdon [131], the creep rate during viscous glide can be related to the solute atom diffusion coefficient ($\widetilde{D}$), solute-solvent size difference (e), and concentration of solute atoms (c) in the following manner:

$$\dot{\varepsilon} \propto \frac{\widetilde{D}}{e^2 c} \qquad (1.5).$$

Maruyama et al., have also identified atomic size misfit and the interdiffusion coefficient as the major parameters to be considered for solution hardening [132]. Table 1-3 includes solubilities and atomic radii of some of the alloying elements of interest. Sn is very close in size to Mg, and thus is not expected to contribute as much to solid-solution strengthening despite its high solubility. However, as will be discussed in Chapters 4 and 5, Sn can affect the solubility of other elements present in the α-Mg. Al and Zn have higher solubility than the other elements with large size differences, and therefore may have increased solid-solution strengthening ability.

Table 1-3 - Atomic size and solubility in Mg for typical alloying elements

Element	Atomic radius (pm)*	Max. solubility in Mg (wt%)
Al	143	12.9
Zn	134	6.2
Mn	127	2.2
Si	111	0
La	187	0.8
Ce	182	0.5
Sn	163	14.5
Ca	197	1.3
Sr	215	0.1

* Mg atomic radius = 160 pm

Precipitation strengthening has been observed in such alloys systems as Mg-Gd [61, 62, 71, 72], Mg-Ca-Zn [130, 133], Mg-Sn-Zn-(Na) [134], Mg-Y-RE [123] and Mg-Al-Zn [29, 30, 32]. Several examples are shown in Figure 1.22. In AZ91, precipitates of β-$Mg_{17}Al_{12}$ formed during aging. Most of the precipitates were found to lie parallel to the basal

plane, although a small proportion of the precipitates lay perpendicular to this plane. The volume fraction of precipitates varied from 1.0×10^{12} /mm^3 at 70°C to 1.5×10^9 /mm^3 at 300°C. According to Celotto, the aging response of AZ91 is poor compared to many Al alloys because the continuous precipitates are not efficient obstacles to slip on the basal plane due to their orientation and also due to the low volume fraction of precipitates compared to Al alloys [29].

In an Mg-6Gd-0.6Zr alloy that was further alloyed with Zn, the creep strength of the alloy was improved by the formation of a uniform and dense distribution of basal plate precipitates that were not observed in Zn-free alloys [71]. If 2wt% Ag is added with the Zn, the peak hardness at 200 and 250°C was reported to increase even more substantially than with Zn additions alone [135]. In a study by Gao et al. [133], the addition of Zr and Nd to an Mg-1Ca-1Zn alloy led to a creep resistance that was significantly higher than AZ91 at temperatures up to 150°C. A hardness increase of approximately 30 HV was reported in these alloys. Peak aged microstructures of Mg-1Ca-1Zn, Mg-1Ca-1Zn-0.6Zr and Mg-1Ca-1Zn-1Nd-0.6Zr all contained a uniform and dense distribution of disc precipitates on the basal plane of the α-Mg matrix. The alloy containing Zr without Nd had a lower density of precipitates, due to the formation of coarser rod-shaped particles rich in Zn and Zr instead, which coarsened markedly after 1000 hours of aging at 200°C. The Mg-1Ca-1Zn alloy also coarsened markedly under these conditions. However, the alloy that contained both Zr and Nd maintained a dense distribution of disc-shaped precipitates aligned with the basal plane that was much more resistant to coarsening and overaging even after 1000 hours of aging. This alloy also had the best creep resistance of the three alloys at both 150 and 175°C [133]. In WE43 (Mg-4Y-3Nd), both long plate precipitates of metastable β′ ($Mg_{12}NdY$) and short needles of equilibrium β ($Mg_{14}Nd_2Y$) are present. The two precipitates types are interdispersed but non-uniformly distributed from grain to grain. Misfit dislocations at the α/β interface make it difficult for matrix dislocations to pass through the precipitates during creep [123].

Thus, precipitation can also be used to hinder dislocation motion, although the effectiveness of this technique depends on the volume fraction, orientation and stability of the precipitates. Nie has estimated the strengthening effectiveness of multiple precipitate shapes and orientations in Mg alloys. $[0001]_\alpha$ rods are most effective at

increasing the number density of precipitates per unit area for the slip plane, but plate shaped precipitates on prismatic planes are the most effective at increasing strengthening. The least strengthening will come from precipitate plates on basal planes [136]. Some strengthening will result from precipitates with this orientation, however, as demonstrated by effect of basal Al_2Ca precipitates on the creep properties of permanent mold [63, 137] and die-cast [44, 133, 134] AXJ530.

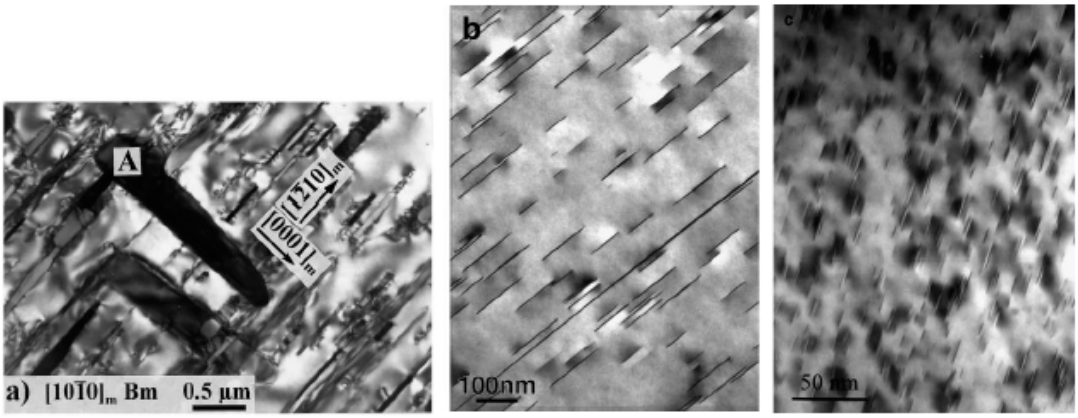

Figure 1.22 – Several examples of precipitates that form during aging: a) AZ91 aged 500 h at 200°C [29], b) peak aged Mg-6Gd-1Zn-0.6Zr [71] and c) Mg-1Ca-1Zn-1Nd-0.6Zr aged 1000 h at 200°C [133].

1.6 Partitioning of Elements during Solidification

As most Mg alloys targeted for powertrain applications will be used in the as-cast state, it is very important to understand the elemental partitioning that occurs during solidification of the alloy and its influence on high temperature strengthening mechanisms. In these alloys, a compositional variation across a dendrite or cell results from redistribution of the solute during solidification [138, 139]. The first α-Mg that forms from the melt is solute lean and further solute enrichment that occurs during solidification leads to precipitation of intermetallic phases in the interdendritic regions. If no appreciable back diffusion occurs in the solid, the solute concentration remains inhomogeneously distributed across the dendrite or cell [139].

The segregation of solute during solidification can be modeled using the Scheil equation for non-equilibrium solidification:

$$C_s = kC_0(1 - f_s)^{(k-1)} \qquad (1.6),$$

where C_s is the composition of the solid, C_0 is the bulk composition, k is the partitioning coefficient and f_s is the fraction solid [140, 141]. The partitioning coefficient, k, is defined as

C_s / C_L, where C_L is the composition of the liquid. Elements with $k > 1$ (e.g. Mg in Mg-4Al-4La [63] and Mn in AM50 [142]) segregate to the dendrite (cell) core, while elements with $k < 1$ (e.g. Al and La in Mg-4Al-4La [63]) segregate to the interdendritic region during solidification. The shape of the partitioning curves for both these cases is illustrated in Figure 1.23 for permanent mold cast Mg-4Al-4La. Elements with $k \approx 1$ will not strongly segregate during solidification.

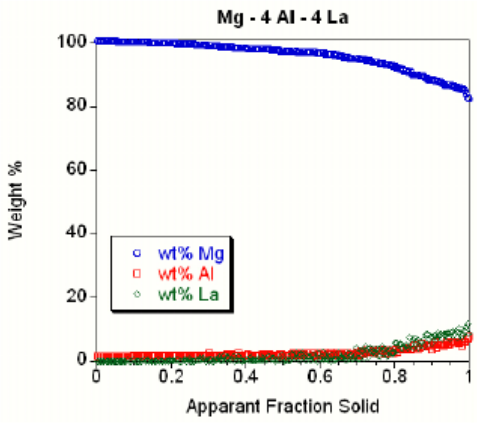

Figure 1.23 - Segregation profiles for an Mg-4Al-4La alloy. Mg (blue curve) illustrates an element with $k>1$, while Al and La both have $k<1$ [63].

The use of the Scheil equation assumes that there is no back diffusion in the solid, and that perfect mixing occurs in the liquid. The liquid composition is also assumed to be uniform, and that the phase field boundaries are linear. Because back diffusion may occur in the solid, a modified Scheil analysis [140] can also be utilized:

$$C_s = kC_0(1-(1-2\alpha k) f_s)^{\frac{k-1}{1-2\alpha k}} \qquad (1.7),$$

where the Fourier term, α, is related to the diffusion coefficient (D), local solidification time (t) and length scale of segregation (L) in the following manner:

$$\alpha = \frac{Dt}{L^2} \qquad (1.8).$$

Other microsegregation models have been developed over the years, including numerical models that take into account dendrite shape, coarsening behavior and undercooling [135, 139-141]. Undercooling may be driven by solutal effects, curvature effects, gradient undercooling, kinetic undercooling, and undercooling due to solute trapping [143].

Elemental partitioning is usually quantified using SEM-EDS or EMPA-WDS measurements of composition [144, 145]. Point composition measurements are made along

either a square grid or arbitrarily selected lines [142, 144-147]. Once the data has been collected, various sorting techniques have been used to analyze the microsegregation that occurs. The Flemings-Gungor approach sorts all elements independently, with the concentration of each element monotonically increasing or decreasing depending on their determined direction of segregation (i.e. to dendrite core or interdendritic region) [146]. Because each element is sorted separately, the segregation profiles are all smooth and continuous. Single element sorts can also be used, where the concentration of all other elements is sorted according to the concentration of one particular solute. An example of this was the study of microsegregation in quaternary Ni-based superalloys by Huang et al. [147]. A difference sort can also be used, where the concentration difference at each collection point between a pair of preselected elements is determined, and these values are then ranked in ascending order together with the other components for each location. Universal sorts, like the rank sort and weighted interval rank sort (WIRS) have also been used, where a fraction solid is assigned based on the rank between the lowest concentration and the highest concentration. Elements that partition to the interdendritic region have a rank of 1 assigned to the minimum concentration, while elements that segregate to the dendrite core have rank 1 assigned to the maximum. Fraction solids are determined by averaging the ranks assigned for each component. In WIRS, the assigned rank is weighted based on the uncertainty associated with measurement of that component [144]. Ganesan et al. have used the WIRS technique to study microsegregation in cast Al-Si-Cu alloys [148] and Mirkovic and Schmid-Fetzer have recently applied it to two ternary Mg alloys [142, 149].

Segregation in Mg-based alloys has been studied via directional solidification [142, 149-152]. The resulting microstructure depends strongly on the withdrawal rate used during directional solidification, since this controls the cooling rate of the alloy [151]. Many of these directional solidification studies have been undertaken as part of a larger study of the thermodynamic equilibrium in Mg alloy systems. Zhang et al. studied microsegregation in binary Mg-4Al, as well as in Mg-Al-Ca alloys such as Mg-5Al-3Ca and AXJ530 [150, 151]. For these alloys, the Al concentration was found to increase gradually as solidification progressed until the formation of eutectic near the end of solidification, where an abrupt increase in Al concentration was observed. This was true

whether the eutectic contained β-$Mg_{17}Al_{12}$ as in binary Mg-4Al [151] or $(Mg,Al)_2Ca$ (C36) as in AXJ530 [150]. For the Ca-containing alloys, Zhang et al. also found that the concentration of Ca in the primary α-Mg was negligibly small [150]. Mirkovic and Schmid-Fetzer have also analyzed microsegregation in AZ31 and AM50 castings produced by directional solidification [149, 150, 153]. In these alloys, Al and Zn both segregate to the interdendritic region, while Mn was found to segregate to the dendrite cores. Mirkovic and Schmid-Fetzer found no significant impact of cooling rate on the Al distribution [149], while Zhang et al. found a slight dependence on withdrawal rate, where the fastest withdrawal rate had slightly lower Al concentration [151]. Mirkovic and Schmid-Fetzer observed an effect of furnace temperature, however, which they attributed to a larger loss of Al at high temperatures [149]. Both Zhang et al. and Mirkovic and Schmid-Fetzer report significant discrepancies between their experimental results and the calculated Scheil model, attributed to back diffusion during solidification of the alloys [149-153].

Microsegregation has been studied to a lesser extent in non-directionally solidified Mg specimens. It is important, however, to understand elemental partitioning in material that has not been directionally solidified, since most components used in practical applications fall into this category. Suzuki et al. studied the effect of Sr additions on partitioning in Mg-5Al-3(Ca,Sr) alloys, and found that Sr additions of greater than 1wt% increased the partitioning of Al to the primary α-Mg phase. This increased Al partitioning lead to the formation of the $Mg_{17}Sr_2$ phase as a major eutectic component [96]. As Zhang et al. [150] note, however, basic microsegregation information is lacking for most Mg alloys, especially compared to Al alloys.

1.7 Objectives and Approach

Before low-density Mg alloys can be used extensively for high temperature powertrain applications, creep resistance must be improved. However, many questions still remain about the creep behavior of Mg alloys, and fundamental information is needed to improve the alloy development process. Contradictions exist regarding the best approach for design of creep-resistant alloys, particularly regarding the effect of solute additions. There is no consensus on the operative creep mechanisms, and many

studies rely on stress exponent or activation energy to determine creep mechanism, neglecting the dislocation substructures entirely.

The current investigation focuses on gaining a more complete understanding of solute strengthening and precipitation strengthening in improved creep resistance by combining microstructural analysis with measurements of elemental partitioning, creep experiments and thermodynamic simulations. Commercial alloys based on the ternary Mg-Al-Ca system and experimental quaternary alloys with simplified compositions have been studied. Mg-Al-Ca alloys were selected because of their potential for solute and precipitation strengthening during creep and because of growing interest in their use for automotive powertrain applications.

The overall objective of this research has been to develop a fundamental understanding of the creep processes in Mg-Al-Ca alloys, with specific focus on solute and precipitation strengthening. In particular, the effect of Sn on elemental partitioning and subsequent effects on creep behavior were investigated, and the results used to identify general alloying strategies for improved creep resistance in Mg alloys. Operative creep mechanisms for a range of alloys were investigated through creep experiments and observation of the dislocation substructures that develop during creep. The effect of solute additions on elemental partitioning during solidification, microstructural stability and creep resistance was investigated. Experimental procedures will be presented in Chapter 2, while Chapter 3 examines the microstructure, tensile creep behavior, and dislocation substructures of die-cast Mg-Al-Ca-based alloys. Elemental partitioning in these same alloys is described in Chapter 4, and the implications for creep behavior are discussed. In Chapter 5, microstructures, elemental partitioning and creep behavior of Mg-Al-Ca-Sn alloys are presented, and the contribution of solute and precipitation strengthening to creep resistance are discussed. Chapter 6 summarizes the major conclusions of this research and provides recommendations for future studies.

References

[1] A. A. Luo, *International Materials Reviews* **2004**, *49*, 13.

[2] M. O. Pekguleryuz, E. Baril, *Materials Transactions* **2001**, *42*, 1258.

[3] P. Bakke, H. Westengen, S. Sannes, D. Albright, *SAE Technical Paper 2004-01-0655*, SAE International, Detroit, MI, **2004**.

[4] J. A. Hines, R. C. McCune, J. E. Allison, B. R. Powell, L. J. Ouimet, W. L. Miller, R. Beals, L. Kopka, P. P. Ried, *SAE Technical Paper 2006-01-0522*, SAE International, Detroit, MI, **2006**.
[5] S. M. Allen, E. L. Thomas, *The Structure of Materials*, John Wiley & Sons, Inc., New York, **1999**.
[6] *ASM Handbook, Vol. 2, Properties and Selection: Nonferrous Alloys and Special-Purpose Materials*, ASM International, **1992**.
[7] M. H. Yoo, *Metallurgical Transactions A* **1981**, *12A*, 409.
[8] D. J. Bacon, V. Vitek, *Metallurgical and Materials Transactions A* **2002**, *33A*, 721.
[9] D. J. Oh, R. A. Johnson, *Journal of Nuclear Materials* **1989**, *169*, 5.
[10] N. N. Greenwood, A. Earnshaw, *Chemistry of the Elements*, 2nd ed., Elsevier, **1997**.
[11] G. V. Raynor, *The Physical Metallurgy of Magnesium and its Alloys*, Pergamon Press, New York, **1959**.
[12] M. H. Yoo, J. R. Morris, K. M. Ho, S. R. Agnew, *Metallurgical and Materials Transactions* **2002**, *33A*, 813.
[13] S. R. Agnew, J. A. Horton, M. H. Yoo, *Metallurgical and Materials Transactions* **2002**, *33A*, 851.
[14] T. Obara, H. Yoshinga, S. Morozumi, *Acta Metall.* **1973**, *21*, 845.
[15] S. R. Agnew, K. C. Liu, E. A. Kenik, S. Viswanathan, in *Magnesium Technology 2000* (Eds.: H. I. Kaplan, J. Hryn, B. Clow), TMS, **2000**, pp. 285.
[16] B. C. Wonsiewicz, W. A. Backofen, *Transactions of the Metallurgical Society of AIME* **1967**, *239*, 1422.
[17] Z. Keshavarz, M. R. Barnett, *Scripta Materialia* **2006**, *55*, 915.
[18] M. R. Barnett, *Materials Science and Engineering A* **2007**, *464*, 8.
[19] R. E. Reed-Hill, *Transactions of the Metallurgical Society of AIME* **1960**, *218*, 554.
[20] W. H. Hartt, R. E. Reed-Hill, *Transactions of the Metallurgical Society of AIME* **1967**, *239*, 1511.
[21] E. C. Burke, W. R. Hibbard Jr, *Journal of Metals* **1952**, *4*, 295.
[22] E. W. Kelley, W. F. Hosford Jr., *Transactions of the Metallurgical Society of AIME* **1968**, *242*, 5.
[23] A. Akhtar, E. Teghtsoonian, *Acta Metall.* **1969**, *17*, 1339.
[24] A. Akhtar, E. Teghtsoonian, *Acta Metall.* **1969**, *17*, 1351.
[25] A. Akhtar, E. Teghtsoonian, *Philosophical Magazine* **1972**, *25*, 897.
[26] A. Couret, D. Caillard, *Acta Metall.* **1985**, *33*, 1447.
[27] J. F. King, in *Magnesium Alloys and their Applications* (Eds.: B. L. Mordike, K. U. Kainer), Werkstoff-Informationsgesellschaft, Wolfsburg, Germany, **1998**, pp. 37.
[28] S. Housh, B. Mikucki, A. Stevenson, in *ASM Handbook, Vol. 2 (Properties and Selection of Non-ferrous Allloys and Special-Purpose Materials)*, ASM, **1992**.
[29] S. Celotto, *Acta Materialia* **2000**, *48*, 1775.
[30] S. Celotto, T. J. Bastow, *Acta Materialia* **2001**, *49*, 41.
[31] C. Zhang, D. Ma, K.-S. Wu, H. B. Cao, G. P. Cao, S. Kou, Y. A. Chang, X. Y. Yan, *Intermetallics* **2007**, *15*, 1395.

[32] J. P. Zhou, D. S. Zhao, R. H. Wang, Z. F. Sun, J. B. Wang, J. N. Gui, O. Zheng, *Materials Letters* **2007**, *61*, 4707.
[33] *ASM Handbook, Vol. 3 - Alloy Phase Diagrams*, ASM International, **1992**.
[34] NRL, "Crystal Lattice Structures", *<http://cst-www.nrl.navy.mil/lattice/spcgrp/index.html>*, **1998**.
[35] A. Luo, M. O. Pekguleryuz, *Journal of Materials Science* **1994**, *29*, 5259.
[36] M. S. Dargusch, G. L. Dunlop, K. Pettersen, in *Magnesium Alloys and their Applications* (Eds.: B. L. Mordike, K. U. Kainer), Werkstoff-Informationsgesellschaft mbH, Frankfurt, Germany, **1998**, pp. 277.
[37] M. S. Dargusch, K. Pettersen, K. Nogita, M. D. Nave, G. L. Dunlop, *Mat Trans* **2006**, *47*, 977.
[38] M. S. Dargusch, A. L. Bowles, K. Pettersen, P. Bakke, G. L. Dunlop, *Metallurgical and Materials Transactions* **2004**, *35A*, 1905.
[39] S. S. Vagarali, T. G. Langdon, *Acta Metall.* **1981**, *29*, 1969.
[40] S. S. Vagarali, T. G. Langdon, *Acta Metall.* **1982**, *30*, 1157.
[41] S. M. Zhu, M. A. Gibson, J. F. Nie, M. A. Easton, T. B. Abbott, *Scripta Materialia* **2008**, *58*, 477.
[42] H. Sato, H. Oikawa, in *9th Int. Conf. on Strength of Metals and Alloys*, Haifa, Israel, **1991**, pp. 463.
[43] S. Spigarelli, M. Regev, E. Evangelista, A. Rosen, *Materials Science and Technology* **2001**, *17*, 627.
[44] M. Regev, E. Aghion, A. Rosen, *Materials Science and Engineering A* **1997**, *234-236*, 123.
[45] M. Ohno, D. Mirkovic, R. Schmid-Fetzer, *Materials Science and Engineering A* **2006**, *421*, 328.
[46] M. Regev, A. Rosen, M. Bamberger, *Metallurgical and Materials Transactions* **2001**, *32A*, 1335.
[47] A. Suzuki, N. D. Saddock, J. R. TerBush, B. R. Powell, J. W. Jones, T. M. Pollock, *SAE Technical Paper 2007-01-1025*, SAE International, Detroit, MI, **2007**.
[48] M. Vogel, O. Kraft, E. Arzt, *Scripta Materialia* **2003**, *48*, 985.
[49] M. Vogel, O. Kraft, G. Dehm, E. Arzt, *Scripta Materialia* **2001**, *45*, 517.
[50] Z. Zhang, R. Tremblay, D. Dube, A. Couture, *Canadian Metallurgical Quarterly* **2000**, *39*, 503.
[51] L. Bourgeois, B. C. Muddle, J. F. Nie, *Acta Materialia* **2001**, *49*, 2701.
[52] Z. Zhang, A. Couture, A. Luo, *Scripta Materialia* **1998**, *39*, 45.
[53] C. J. Siemensen, B. C. Oberlander, J. Svalestuen, A. Thorvaldsen, *Z. Metallkd.* **1989**, *80*, 101.
[54] M. Ohno, R. Schmid-Fetzer, *Z. Metallkd.* **2005**, *96*, 857.
[55] V. Y. Gertsman, J. Li, S. Xu, J. P. Thomson, M. Sahoo, *Metallurgical and Materials Transactions A* **2005**, *36A*, 1989.
[56] N. Ishimatsu, Y. Terada, T. Sato, K. Ohori, *Metallurgical and Materials Transactions A* **2006**, *37A*, 243.
[57] G. Chadha, J. E. Allison, J. W. Jones, *Metallurgical and Materials Transactions A* **2007**, *38A*, 286.

[58] R. M. Wang, A. Eliezer, E. M. Gutman, *Materials Science and Engineering A* **2003**, *355*, 201.
[59] Y. Carbonneau, A. Couture, A. Van Neste, R. Tremblay, *Metallurgical and Materials Transactions A* **1998**, *29A*, 1759.
[60] P. Zhang, *Scripta Materialia* **2005**, *52*, 277.
[61] X. Gao, S. M. He, X. Q. Zeng, L. M. Peng, W. J. Ding, J. F. Nie, *Materials Science and Engineering A* **2006**, *431*, 322.
[62] B. Smola, I. Stulikova, J. Pelcova, B. L. Mordike, *Journal of Alloys and Compounds* **2004**, *378*, 196.
[63] N. D. Saddock, Ph.D. thesis, University of Michigan (Ann Arbor, MI), **2007**.
[64] H. Dieringa, N. Hort, K. U. Kainer, *Materials Science and Engineering A* **2009**, *510-511*, 382.
[65] B. R. Powell, V. Rezhets, M. P. Balogh, R. A. Waldo, *JOM* **2002**, *54*, 34.
[66] R. Ayer, L. M. Angers, R. R. Mueller, J. C. Scanlon, C. F. Klein, *Metallurgical Transactions A* **1988**, *19*, 1645.
[67] P. Bakke, H. Westengen, in *Magnesium Technology 2005* (Eds.: N. R. Neelameggham, H. I. Kaplan, B. R. Powell), TMS, San Francisco, CA, **2005**, pp. 291.
[68] H. Dieringa, N. Hort, K. U. Kainer, in *Magnesium Technology 2007* (Eds.: R. S. Beals, A. A. Luo, N. R. Neelameggham, M. O. Pekguleryuz), TMS, Orlando, FL, **2007**, pp. 395.
[69] S. M. Zhu, M. A. Gibson, J. F. Nie, M. A. Easton, P. Bakke, in *Magnesium Technology 2008* (Eds.: M. O. Pekguleryuz, N. R. Neelameggham, R. S. Beals, E. A. Nyberg), TMS, New Orleans, LA, **2008**, pp. 437.
[70] S. Spigarelli, E. Evangelista, M. Cabibbo, M. El Mehtedi, in *Magnesium Technology 2007* (Eds.: R. S. Beals, A. A. Luo, N. R. Neelameggham, M. O. Pekguleryuz), TMS, Orlando, FL, **2007**, pp. 401.
[71] J. F. Nie, X. Gao, S. M. Zhu, *Scripta Materialia* **2005**, *53*, 1049.
[72] Q. M. Peng, Y. M. Wu, D. Q. Fang, J. Meng, L. M. Wang, *Journal of Alloys and Compounds* **2007**, *430*, 252.
[73] I. P. Moreno, T. K. Nandy, J. W. Jones, J. E. Allison, T. M. Pollock, *Scripta Materialia* **2003**, *48*, 1029.
[74] E. Doernberg, A. Kozlov, R. Schmid-Fetzer, *Journal of Phase Equilibria and Diffusion* **2007**, *28*, 523.
[75] J. Y. Kim, E. J. Kim, J. W. Han, *Materials Science Forum* **2009**, *620-622*, 295.
[76] A. Luo, A. K. Sachdev, in *Mg Technology 2009* (Eds.: E. A. Nyberg, S. R. Agnew, N. R. Neelameggham, M. O. Pekguleryuz), TMS (Warrendale, PA), San Francisco, CA, **2009**, pp. 437.
[77] N. Hort, Y. Huang, T. Abu Leil, P. Maier, K. U. Kainer, *Advanced Engineering Materials* **2006**, *8*, 359.
[78] A. Kozlov, M. Ohno, T. Abu Leil, N. Hort, K. U. Kainer, R. Schmid-Fetzer, *Intermetallics* **2008**, *16*, 316.
[79] T. Abu Leil, K. P. Rao, N. Hort, Y. Huang, C. Blawert, H. Dieringa, K. U. Kainer, in *Magnesium Technology 2007* (Eds.: R. S. Beals, A. A. Luo, N. R. Neelameggham, M. O. Pekguleryuz), TMS, Orlando, FL, **2007**, pp. 257.

[80] A. Kozlov, M. Ohno, R. Arroyave, Z. K. Liu, R. Schmid-Fetzer, *Intermetallics* **2008**, *16*, 299.
[81] D. H. Kim, H. K. Lim, J. Y. Lee, W. T. Kim, D. H. Kim, in *Magnesium Technology 2008* (Eds.: M. O. Pekguleryuz, N. R. Neelameggham, R. S. Beals, E. A. Nyberg), TMS, New Orleans, LA, **2008**, pp. 417.
[82] N. Hort, K. P. Rao, T. Abu Leil, H. Dieringa, V. Y. R. K. Prasad, K. U. Kainer, in *Magnesium Technology 2008* (Eds.: M. O. Pekguleryuz, N. R. Neelameggham, R. S. Beals, E. A. Nyberg), TMS, New Orleans, LA, **2008**.
[83] B. R. Powell, A. A. Luo, V. Rezhets, J. J. Bommarito, B. L. Tiwari, *SAE Technical Paper 2001-01-0422*, SAE International, Detroit, MI, **2001**.
[84] B. R. Powell, V. Rezhets, A. A. Luo, B. L. Tiwari, General Motors, US Patent 6,264,763, **2001**.
[85] B. Bronfin, N. Moscovitch, V. Trostenetsky, G. Gerzberg, N. Nagar, R. Yehuda, in *Magnesium Technology 2008* (Eds.: M. O. Pekguleryuz, N. R. Neelameggham, R. S. Beals, E. A. Nyberg), TMS, New Orleans, LA, **2008**, pp. 411.
[86] B. Bronfin, E. Aghion, F. Von Buch, S. Schumann, M. Katzir, Dead Sea Magnesium Ltd and Volkswagen AG, US Patent 7,041,179 B2, **2006**.
[87] A. Suzuki, N. D. Saddock, J. W. Jones, T. M. Pollock, *Acta Materialia* **2005**, *53*, 2823.
[88] H. Cao, C. Zhang, J. Zhu, G. Cao, S. Kou, R. Schmid-Fetzer, Y. A. Chang, *Scripta Materialia* **2008**, *58*, 397.
[89] A. Suzuki, N. D. Saddock, J. W. Jones, T. M. Pollock, *Scripta Materialia* **2004**, *51*, 1005.
[90] M. O. P. a. A. A. Kaya, *Advanced Engineering Materials* **2003**, *5*, 866.
[91] A. Suzuki, N. D. Saddock, J. W. Jones, T. M. Pollock, *Metallurgical and Materials Transactions A* **2006**, *37A*, 975.
[92] A. A. Luo, M. P. Balogh, B. R. Powell, *Metallurgical and Materials Transactions* **2002**, *33A*, 567.
[93] A. Suzuki, N. D. Saddock, L. Riester, E. Lara-Curzio, J. W. Jones, T. M. Pollock, in *Magnesium Technology 2006* (Eds.: A. A. Luo, N. R. Neelameggham, R. S. Beals), TMS, San Antonio, TX, **2006**, pp. 523.
[94] H. Cao, J. Zhu, C. Zhang, K. Wu, N. D. Saddock, J. W. Jones, T. M. Pollock, R. Schmid-Fetzer, Y. A. Chang, *Int. J. Mat. Res.* **2006**, *97*, 422.
[95] M. Pekguleryuz, P. Labelle, D. Argo, *SAE Technical Paper 2003-01-0190*, SAE International, Detroit, MI, **2003**.
[96] A. Suzuki, N. D. Saddock, L. Riester, E. Lara-Curzio, J. W. Jones, T. M. Pollock, *Metallurgical and Materials Transactions A* **2007**, *38A*, 420.
[97] W. D. Callister, Jr, in *Materials Science and Engineering: An Introduction*, 5th ed., John Wiley & Sons, Inc., New York, **2000**, pp. 225.
[98] C. Herring, *Journal of Applied Physics* **1950**, *21*, 437.
[99] R. L. Coble, *Journal of Applied Physics* **1963**, *34*, 1679.
[100] T. G. Langdon, *Materials Science and Engineering* **2000**, *A283*, 266.
[101] T. G. Langdon, *Journal of Materials Science* **2006**, *41*, 597.
[102] W. Vickers, P. Greenfield, *Journal of Nuclear Materials* **1967**, *24*, 249.
[103] O. A. Ruano, O. D. Sherby, J. Wadsworth, J. Wolfenstine, *Scripta Materialia* **1998**, *38*, 1307.

[104] R. S. Kottada, A. H. Chokshi, *Metallurgical and Materials Transactions A* **2007**, *38A*, 1743.
[105] Y. Ishida, A. W. Mullendo, N. J. Grant, *Transactions of the Metallurgical Society of AIME* **1965**, *233*, 204.
[106] J. Koike, R. Ohyama, T. Kobayashi, M. Suzuki, K. Marayuma, *Materials Transactions* **2003**, *44*, 445.
[107] R. Bell, C. Graeme-Barber, T. G. Langdon, *Transactions of the Metallurgical Society of AIME* **1967**, *239*, 1821.
[108] R. L. Bell, T. G. Langdon, *Journal of Materials Science* **1967**, *2*, 313.
[109] W. Blum, Y. J. Li, X. H. Zeng, P. Zhang, B. Von Groβmann, C. Haberling, *Metallurgical and Materials Transactions* **2005**, *36A*, 1721.
[110] A. H. Cottrell, M. A. Jaswon, *Proceedings of the Royal Society of London. Series A, Mathematical and Physical Sciences* **1949**, *199*, 104.
[111] A. H. Cottrell, *Progress in Metal Physics* **1949**, *1*, 77.
[112] J. Lothe, *Journal of Applied Physics* **1960**, *31*, 1077.
[113] J. Weertman, *Journal of Applied Physics* **1955**, *26*, 1213.
[114] R. M. Thomson, R. W. Balluffi, *Journal of Applied Physics* **1962**, *33*, 803.
[115] R. W. Balluffi, *Phys. Stat. Sol.* **1969**, *31*, 443.
[116] H. Somekawa, K. Hirai, H. Watanabe, Y. Takigawa, K. Higashi, *Materials Science and Engineering A* **2005**, *407*, 53.
[117] V. Srivastava, K. R. McNee, G. W. Greenwood, H. Jones, *Materials Science and Technology* **2004**, *20*, 42.
[118] S. Spigarelli, M. Cabibbo, E. Evangelista, M. Talianker, V. Ezersky, *Materials Science and Engineering A* **2000**, *289*, 172.
[119] S. Ji, M. Qian, Z. Fan, *Materials Science and Engineering A* **2006**, *434*, 7.
[120] M. Regev, E. Aghion, A. Rosen, M. Bamberger, *Materials Science and Engineering A* **1998**, *252*, 6.
[121] K. Milicka, J. Cadek, P. Rys, *Acta Metall.* **1970**, *18*, 1071.
[122] C. J. Boehlert, K. Knittel, *Materials Science and Engineering A* **2006**, *417*, 315.
[123] J. G. Wang, L. M. Hsiung, T. G. Nieh, M. Mabuchi, *Materials Science and Engineering A* **2001**, *315*, 81.
[124] B. L. Mordike, I. Stulíková, B. Smola, *Metallurgical and Materials Transactions* **2005**, *36A*, 1729.
[125] M. Suzuki, H. Sato, K. Maruyama, H. Oikawa, *Materials Science and Engineering A* **2001**, *319-321*, 751.
[126] M. Suzuki, H. Sato, K. Maruyama, H. Oikawa, *Materials Science and Engineering A* **1998**, *252*, 248.
[127] S. M. Zhu, B. L. Mordike, J. F. Nie, *Materials Science and Engineering A* **2008**, *483-484*, 583.
[128] S. M. Zhu, B. L. Mordike, J. F. Nie, *Metallurgical and Materials Transactions A* **2006**, *37A*, 1221.
[129] M. Vogel, O. Kraft, E. Arzt, *Metallurgical and Materials Transactions* **2005**, *36A*, 1713.
[130] G. Levi, S. Avraham, A. Zilberov, M. Bamberger, *Acta Materialia* **2006**, *54*, 523.
[131] F. A. Mohamed, T. G. Langdon, *Acta Metall.* **1974**, *22*, 779.

[132] K. Maruyama, M. Suzuki, H. Sato, *Metallurgical and Materials Transactions* **2002**, *33A*, 875.
[133] X. Gao, S. M. Zhu, B. C. Muddle, J. F. Nie, *Scripta Materialia* **2005**, *53*, 1321.
[134] C. L. Mendis, C. J. Bettles, M. A. Gibson, C. R. Hutchinson, *Materials Science and Engineering A* **2006**, *435-436*, 163.
[135] X. Gao, J. F. Nie, *Scripta Materialia* **2008**, *58*, 619.
[136] J. F. Nie, *Scripta Materialia* **2003**, *48*, 1009.
[137] N. D. Saddock, A. Suzuki, J. R. TerBush, J. W. Jones, T. M. Pollock, J. E. Zindel, J. E. Allison, *SAE Technical Paper 2007-01-1027*, SAE International, Detroit, MI, **2007**.
[138] Y. M. Won, B. G. Thomas, *Metallurgical and Materials Transactions* **2001**, *32A*, 1755.
[139] D. A. Porter, K. E. Easterling, in *Phase Transformations in Metals and Alloys*, 2nd ed., Nelson Thornes Ltd, Cheltenham, **1992**, pp. 185.
[140] H. D. Brody, M. C. Flemings, *Transactions of the Metallurgical Society of AIME* **1966**, *236*, 615.
[141] T. F. Bower, H. D. Brody, M. C. Flemings, *Transactions of the Metallurgical Society of AIME* **1966**, *236*, 624.
[142] D. Mirkovic, R. Schmid-Fetzer, *Metallurgical and Materials Transactions A* **2009**, *40A*, 958.
[143] X. Yan, F. Xie, M. Chu, Y. A. Chang, *Materials Science and Engineering A* **2001**, *302*, 268.
[144] M. Ganesan, D. Dye, P. D. Lee, *Metallurgical and Materials Transactions* **2005**, *36A*, 2191.
[145] E. A. Feest, *Journal of the Institute of Metals* **1973**, *101*, 146.
[146] M. Gungor, *Metallurgical Transactions A* **1989**, *20*, 2529.
[147] S. C. Huang, L. Peluso, D. Backman, in *Solidification* (Eds.: W. H. Hofmeister, J. R. Rogers, N. B. Singh, S. P. Marsh, P. W. Vorhees), TMS, **1999**, pp. 163.
[148] M. Ganesan, L. Thuinet, D. Dye, P. D. Lee, *Metallurgical and Materials Transactions B* **2007**, *38B*, 557.
[149] D. Mirkovic, R. Schmid-Fetzer, *Metallurgical and Materials Transactions A* **2009**, *40A*, 974.
[150] C. Zhang, D. Ma, K. Wu, H. Cao, J. Zhu, G. Cao, S. Kou, Y. A. Chang, in *Magnesium Technology 2006* (Eds.: A. A. Luo, N. R. Neelameggham, R. S. Beals), TMS, San Antonio, TX, **2006**, pp. 45.
[151] C. Zhang, D. Ma, K.-S. Wu, H.-B. Cao, G.-P. Cao, S. Kou, Y. A. Chang, X.-Y. Yan, *Intermetallics* **2007**, *15*, 1395.
[152] D. Mirkovic, R. Schmid-Fetzer, in *Magnesium Technology 2009* (Eds.: E. A. Nyberg, S. R. Agnew, N. R. Neelameggham, M. O. Pekguleryuz), TMS, San Francisco, CA, **2009**, pp. 97.

Chapter 2

Experimental Procedures

In this chapter, the relevant experimental procedures are described in some detail. Alloy preparation and casting techniques are described. Microstructural characterization, thermal exposure/aging, measurements of elemental segregation and creep testing procedures are also presented.

2.1 Casting Procedures

Quaternary Mg-Al-Ca-Sn alloys were cast using an induction heated system designed to produce Mg alloys in 25-30g quantities. Starting materials consisted of a master alloy of either Mg-4Al (wt%) or Mg-4Al-4Ca. To the master alloy pure (99.9%) Mg ingot, (99.5%) Al lump and (99.99%) Sn ingot were added; in the cases where the Mg-4Al master alloy was used, elemental (99%) Ca shot was also added. Adding elemental Ca proved to be problematic; small Ca pieces would often vaporize during the casting process, leading to lower Ca concentrations than expected, while larger pieces would not melt completely. To avoid these problems, most of the samples cast utilized the Mg-4Al-4Ca master alloy. The casting setup is shown in Figure 2.1. Melting occurred in a low-carbon steel crucible under a cover gas of 1% SF_6 in Ar. A quartz tube surrounded the crucible to reduce oxidation of the sample during melting, although oxides could still be present from the starting materials. The temperature during the casting process was measured using a k-type thermocouple with a stainless steel sheath covering the exposed end, which was also used to stir the melt for several minutes prior to pouring. Twenty-five gram samples were prepared via this method. The melt was poured onto an unheated steel plate and allowed to cool under a cover gas of 1% SF_6 in Ar. Cooling rates of several degrees Celsius per second were measured. The target compositions for the quaternary alloys cast for this study are included in Table 2-1, as

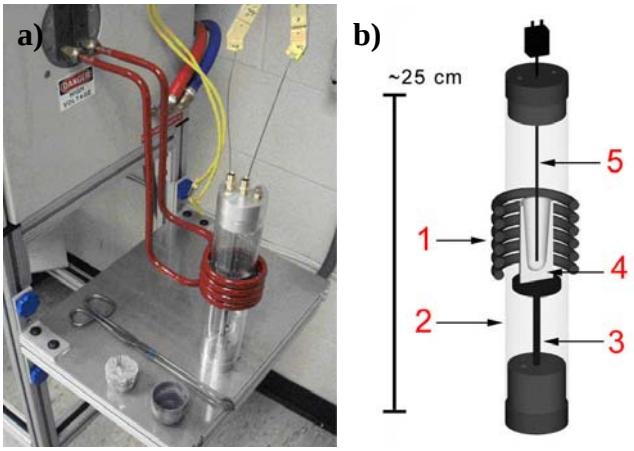

Figure 2.1 - a) Induction coil casting setup. b) Cut-away schematic of the environmental casting chamber: 1 – Induction coil, 2 – Quartz tube, 3 – Platform, 4 – Crucible, 5 – Thermocouple. Images from Saddock [1].

Table 2-1 - Composition of quaternary alloys cast (wt %)

Target Composition	Measured Average Composition
Mg-5Al-3Ca-0.25Sn*	Mg-5.54Al-2.40Ca-0.16Sn
Mg-5Al-3Ca-0.5Sn	Mg-5.07Al-2.88Ca-0.44Sn
Mg-5Al-3Ca-0.75Sn	Mg-5.46Al-2.90Ca-0.51Sn
Mg-5Al-3Ca-1Sn	Mg-5.59Al-3.16Ca-1.78Sn
Mg-5Al-3Ca-1.5Sn*	Mg-5.04A-3.15Ca-1.22Sn
Mg-5Al-3Ca-3Sn	Mg-4.95Al-2.39Ca-2.56Sn
Mg-6.5Al-3Ca-0.5Sn	Mg-6.33Al-2.65Ca-0.37Sn
Mg-6.5Al-2.25Ca-0.8Sn	Mg-6.25Al-2.03Ca-0.59Sn
Mg-8Al-3Ca-0.5Sn	Mg-7.91Al-2.82Ca-0.38Sn
Mg-8Al-1Ca-0.8Sn	Mg-7.79Al-0.92Ca-0.68Sn

* Cast with Mg-4Al master alloy instead of Mg-4Al-4Ca master alloy

well as the average composition measured experimentally from electron microprobe scans. Alloys too far from the target composition were recast. Some alloys were cast multiple times until an acceptable composition was obtained.

A similar casting procedure was used for MRI153M and MRI230D samples. In this case, the starting material consisted of die-cast specimens, made from original ingots produced by Dead Sea Magnesium. Twenty-five gram pieces were cut from the die-cast specimen and melted and cast as described above. The resulting castings had the same composition as the starting material, but larger average cell sizes of approximately 20

μm, facilitating composition measurement with the electron microprobe as described later in this chapter. Average cell size for the die-cast samples was ~ 11 μm. The linear intercept method was used for average cell size determination for both sets of samples.

In later chapters, comparison will also be made to permanent-mold cast AX44 and AXJ530. These samples were prepared by Saddock as part of his thesis research, and are described in more detail elsewhere [1-3] and relevant steps are summarized here. Ingots of AXJ530, provided by General Motors, and AX44, provided by Norsk Hydro, were melted in a Striko-Dynarad resistance furnace in an uncoated mild steel crucible and poured into a preheated permanent mold with a boron nitride coating. A cover gas of 0.5 vol% SF_6, 25 vol% CO_2 and a balance of dry air was used during casting, and the mold temperature increased from 200° to 400°C over the casting run. Cooling rates of ~10°C/s were observed, and an average cell size of 22 μm for AXJ530 and 18 μm for AX44 was measured [2, 3], comparable to the average cell sizes of the recast MRI230D and MRI153M described above.

2.2 Microstructural Characterization

Both scanning electron and transmission electron microscopy were used to examine the microstructure of the various alloys. Procedures for both are described in this section.

2.2.1 Scanning Electron Microscopy (SEM)

Bulk microstructures of as-crept and as-cast specimens were observed using scanning electron microscopy (SEM). Samples were cold mounted in Castolite resin and then metallographically prepared as follows. The samples were ground using 60-1200 grit silicon carbide paper with water lubrication and polished using diamond paste with particle sizes of 3, 1, and 0.25 μm on neoprene cloth. Ethanol was used as lubrication in the polishing process, and the samples were ultrasonically cleaned in ethanol between steps to remove any residue. Die-cast samples received a final polish with 0.05 μm colloidal silica, also on a neoprene cloth. Prior to SEM observation of the die-cast samples, the polished surface was etched to better distinguish the intermetallic phases present in the eutectic regions, given their smaller size. Samples were etched for five

seconds in a solution of 60 mL ethanol, 20 mL de-ionized H_2O, 50 mL glacial acetic acid and 5 mL 60M nitric acid. A Philips XL30 FEG SEM with a backscattered electron (BSE) detector and an accelerating voltage of 20 kV was used in this study. For the induction melted samples, microstructural observation was performed on polished, unetched specimens using a Philips XL30 SEM also in backscatter mode (BSE).

2.2.2 Transmission Electron Microscopy (TEM)

Transmission electron microscopy (TEM) was used to study the dislocation substructures of crept specimens. Slices 0.6 mm thick were cut from the gauge section of the crept specimen perpendicular to direction of loading. These slices were then ground by hand to a thickness of approximately 0.3 mm, at which time discs 3.0 mm in diameter were punched from each slice. These discs were then further ground by hand until they reached a thickness of approximately 0.11-0.12 mm. Final thinning to electron transparency was done with a twin-jet electropolisher using a solution of 8 vol% perchloric acid in methanol. The temperature of the electropolishing solution was kept at approximately -30°C using liquid nitrogen. A voltage of ~10-15 V and a current of ~10-20 mA were sufficient for proper thinning.

A Philips CM-12 scanning transmission electron microscope (STEM) with an operating voltage of 120 kV and a Gatan double-tilt specimen holder (which allowed a tilting range of ± 45° in the x direction and ± 25 in the y direction) were used in this investigation. This wide tilting angle allowed several different low index zone axes to be easily reached during dislocation and phase analysis.

During dislocation imaging, the foil was tilted to a major zone axis. An image of the diffraction pattern was taken for later indexing, and the foil then titled slightly away from the zone axis to a two-beam condition. Under these conditions only two beams – the through (incident) beam and one particular diffracted beam (**g**) – were used to form the image. The contrast in the image comes from diffraction only in the vicinity of a dislocation. When the invisibility criterion of $\mathbf{g}\cdot\mathbf{b} = 0$ is met for a particular dislocation, no contrast will be observed, allowing determination of the Burgers vector for that

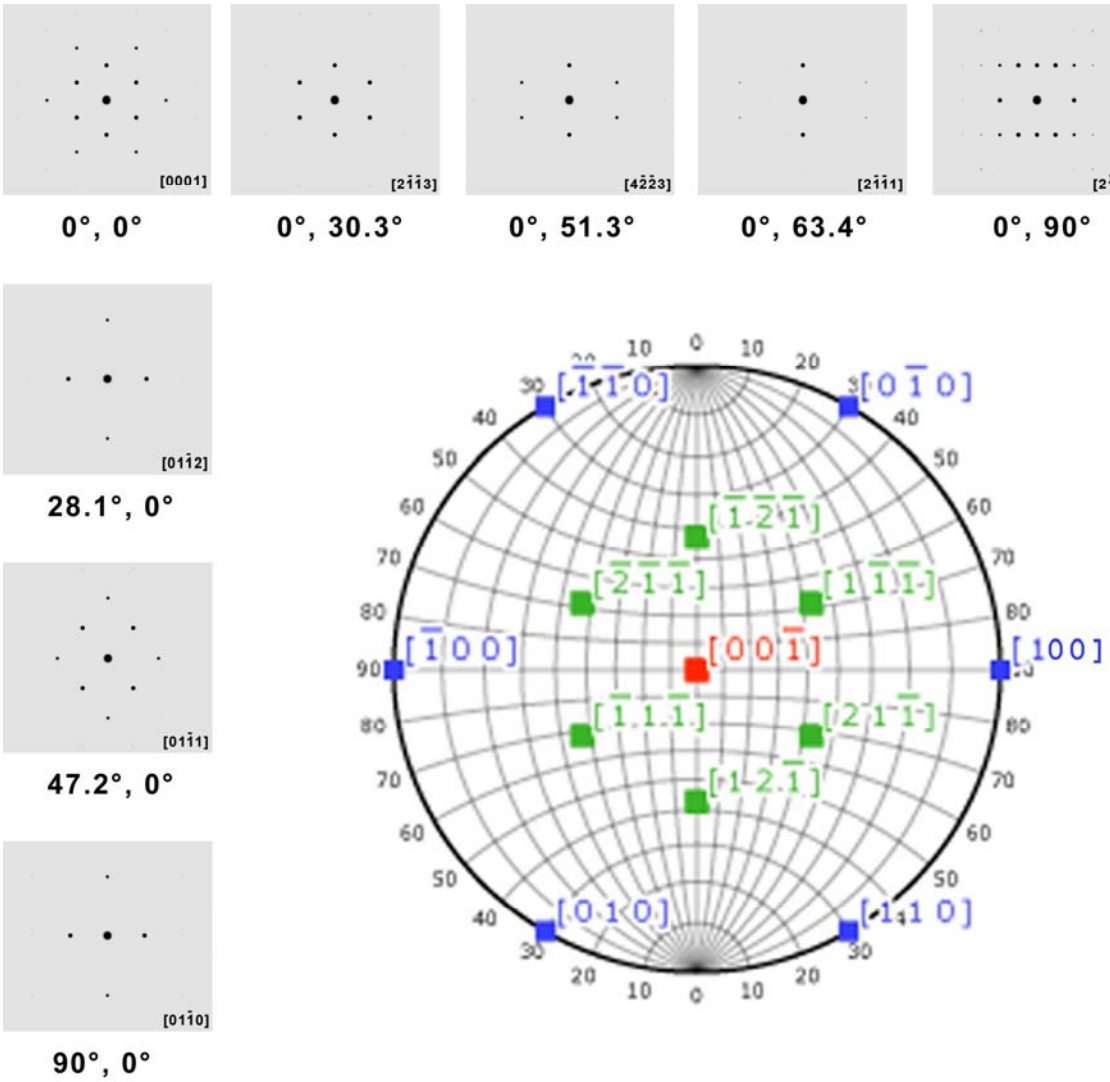

Figure 2.2 - Diffraction pattern map (simulated) for HCP Mg. Included in the lower corner is the stereographic projection.

dislocation. Thus, by tilting to multiple two-beam conditions and observing visibility/invisibility for the dislocation, the dislocation type can be determined. For example, <a> type dislocations will be invisible when **g** = (0002). A zone axis of $[11\bar{2}0]_{\alpha-Mg}$ was used for most dislocation imaging in this investigation. Figure 2.2 shows the diffraction pattern map constructed for Mg, which was used to locate the various zone axes during tilting.

Selected area diffraction patterns from the TEM were also used to identify phases present in the alloys. Patterns were simulated using JEMS or CrystalMaker's

SingleCrystal™ programs. An example of a simulated diffraction pattern is shown in Figure 2.3, along with an experimental diffraction pattern from the same phase.

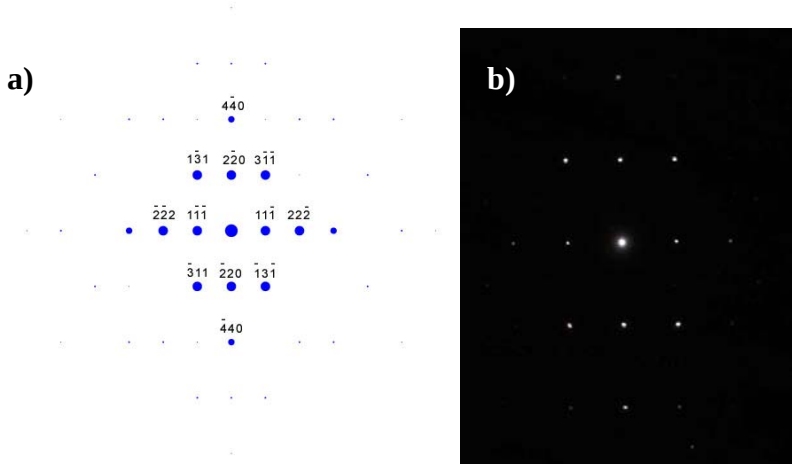

Figure 2.3 - a) Simulated [112] diffraction pattern for Al_2Ca phase. b) Actual diffraction pattern taken from a crept sample of MRI230D.

2.2.3 EDS Mapping

To aid in phase identification, energy dispersive spectroscopy (EDS) was used to examine a bulk sample of the remelted and cast MRI230D. During EDS, the electron beam impinges on the material, causing x-rays to be emitted which have energies characteristic of the elements in the irradiated region. By scanning an area, it is possible to construct an elemental map of that region, where areas with high concentrations of a particular element will appear bright and areas of low concentration will appear dark. This technique can aid in determining qualitatively where a particular element is partitioning during solidification. For this investigation, an FEI Quanta 200 SEM/FIB with a Noran XEDS detector was used to collect elemental maps using an accelerating voltage of 20 kV and with approximately 33,000 cps (counts per second). The 30 mm^2 EDS detector was capable of detecting elements with $Z > 5$ (boron) at a resolution of 128-143 eV.

2.3 Thermal Exposures

To observe microstructural changes that occur in the α-Mg cells at elevated temperatures, particularly the formation of precipitates, thermal aging studies were conducted. Die-cast samples supplied by the USAMP program were sectioned and aged

at temperatures ranging from 175-350°C for times ranging from 10 s to 500 hr. Samples 3x3x10 mm were cut from specimens with nominal dimensions 40x40x10 mm for hardness testing, while samples 3x9x10 mm were used when both hardness and microstructure were examined. A fluidized bed furnace utilizing a fine silica media was used for the aging, and the samples were water quenched to room temperature following the heat treatment. Hardness was measured using a micro-Vickers indenter with a 500 g load and a load time of 15 s. Seven to ten measurements were made for each specimen and the results averaged. TEM was performed for selected specimens to observe the presence of precipitates and the microstructure of the aged specimens. A similar procedure was also used for Mg-5Al-3Ca-0.75Sn and Mg-5Al-3Ca-1.5Sn specimens, which were aged at 250°C for the time range listed above.

2.4 Elemental Segregation

For elemental segregation studies, samples were ground and polished as described previously for SEM. Samples were not etched, however, since a flat surface with minimal scratches is required for microprobe analyses. The entire top surface of the epoxy mount was painted with colloidal graphite, and several millimeters down the side of the mount were also coated to avoid sample charging from the electron beam during long scans.

A Cameca SX100 electron microprobe was used for compositional analysis. A scanning electron microscope with backscatter and EDS detectors was attached to the microprobe. The electron microprobe utilizes wavelength dispersive spectroscopy (WDS) to determine composition at a given point. When the electron beam hits the surface, characteristic x-rays are emitted and collected by the WDS detectors. The counts from the experimental sample are then compared to the calibrated counts from known standards. These standards typically consist of pure metals, alloys and mineral samples. The standards used in this particular study are listed in Table 2-2, along with the x-ray line, crystal type and background levels for each element of interest. The Mg-4Al standard used for Mg calibration was homogenized for 26 days at 400°C.

Table 2-2 – EMPA standards and parameters

Element	Line	Crystal Type	Background	Standard
Mg	Kα	TAP	-600 / +1100	Homogenized Mg-4Al
Al	Kα	TAP	-500 / +800	100% Al
Ca	Kα	LPET/PET	-800 / +700	Wollastonite (34.2% Ca)
Mn	Kα	LLIF	+/- 500	Rhodonite (29.27% Mn)
Zn	Kα	LLIF	+/- 500	100% Zn
Sr	Lα	PET	-1200 / +500	Celestite (47.7% Sr)
Sn	Lα	LPET/PET	+/- 500	100% Sn
O	Kα	LPCO	+/- 2500	SiO_2 (53.3% O)

Area scans consisting of at least 400 points were collected from several regions on the sample surface, following the method of Gungor [4], Tin et al. [5] and Huang et al. [6]. One such area is illustrated in Figure 2.4. A voltage of 20 kV and beam current of 15 nA were used, resulting in a electron beam spot size of approximately 2 μm. In order to minimize overlap between points, a step size of 10 μm was used for most samples. For a small number of samples, the 10 μm step size was not appropriate because it sampled mainly the near-eutectic region, inappropriately skewing the data toward higher solute concentrations. In these instances, the samples were rescanned with smaller step sizes of 3-5 μm. The data was assumed to be accurate when the degree of segregation obtained did not vary with step size. The cell size of the die-cast specimens was too fine for this technique, but the specimens melted with the induction furnace had average cells sizes at least 10x larger than the electron beam. This allowed more accurate composition determination for the experimental samples by decreasing the likelihood of sampling both the α-Mg and eutectic phases during a single microprobe measurement. Only points with total concentrations between 99 and 101 wt% were used for subsequent analysis. Totals outside this range could be caused by sampling more than one phase simultaneously or by oxide films or inclusions. For a given series of scans, 10-30% of the data may fall outside the acceptable range.

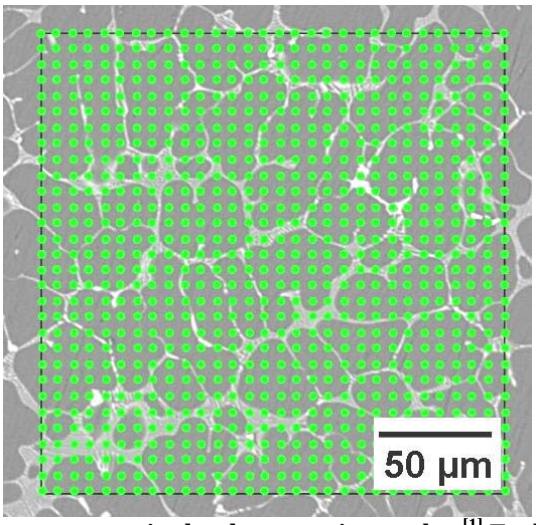

Figure 2.4 – Illustration of an area scan in the electron microprobe. [1] Each green point corresponds to a composition measurement.

Partitioning during solidification causes the Mg concentration to vary from the cell interior to the near-boundary region. Based on the binary phase diagrams the solid that initially forms will have the highest Mg concentration, and the last point to solidify will have the lowest. This is demonstrated in Figure 2.5 for a binary Mg-Al alloy. Accordingly, the raw data from the electron microprobe can be sorted based on decreasing Mg concentration, keeping the concentrations of higher order alloying elements linked to the corresponding Mg concentration as illustrated in Tables 2-3 and 2-4. Each point is then assigned a number based on Mg concentration (where point 1 has the highest Mg concentration, 2 the second highest, and so forth), and this point number is then divided by the total number of points to obtain the apparent fraction solid. Using this scheme, an apparent fraction solid can be determined at each collection point, and the concentration of selected elements can be plotted against this apparent fraction solid to show the segregation that occurs during solidification of the alloy as shown in Figure 2.6.

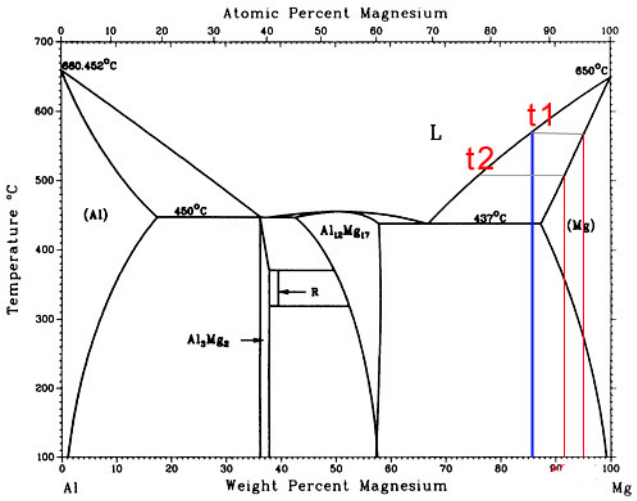

Figure 2.5 – Variation of Mg concentration in a binary Mg-Al alloy, modified from [7]. The solid that forms at t1 has a higher Mg concentration than the solid that forms at t2 for an alloy with the nominal composition indicated by the blue line. (t2 > t1)

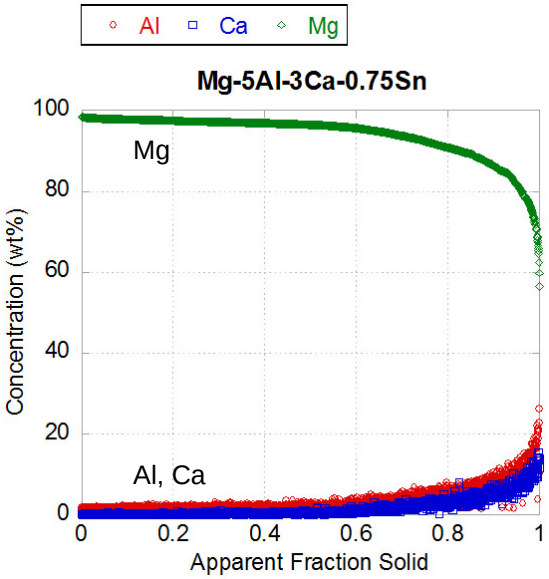

Figure 2.6 - Sample partitioning curves obtained for an Mg-Al-Ca alloy. The Mg curve (green) illustrates an element with $k > 1$, while Al and Ca have the typical shape for elements with $k < 1$.

Table 2-3: Raw data from the electron microprobe

Raw Data						
Data Point	Mg	Al	Ca	Mn	Sn	Total
1	97.068	1.972	0.189	0.009	0.055	99.293
2	97.435	2.051	0.155	0.007	0.043	99.691
.	.	.	.	.	.	.
.	.	.	.	.	.	.
399	97.945	1.705	0.156	0.003	0.067	99.877
400	97.851	1.756	0.196	0.007	0.05	99.86

Table 2-4: Processed data from the electron microprobe

Sorted Data							
Apparent Fraction Solid		Mg	Al	Ca	Mn	Sn	Total
1/1081	0.001	98.324	1.426	0.161	0	0.107	100.018
2/1081	0.002	98.319	1.736	0.182	0.01	0.077	100.324
.	.	.	.	.	.	.	.
.	.	.	.	.	.	.	.
1080/1081	0.999	59.748	26.134	13.806	0.031	0.049	99.769
1081/1081	1.000	56.467	10.166	11.614	0.051	22.882	101.181

2.5 Tensile and Compressive Creep Testing

Constant-load tensile creep tests were conducted by Westmoreland Mechanical Testing and Research Inc. for die-cast specimens of AXJ530, MRI230D and MRI153M. Stress levels of 70 and 110 MPa were used, and testing temperatures ranged from 100-180°C. The creep tests were discontinued after 500 hours unless rupture occurred prior to this time. Crept samples were provided for further analysis courtesy of the USAMP program.

Specimens for compressive creep testing were cut from induction melted samples of MRI230D, Mg-5Al-3Ca-0.75Sn, Mg-5Al-3Ca-1.5Sn and Mg-6.5Al-2.25Ca-0.8Sn. Parallelepiped shaped samples measuring approximately 4x4x8 mm^3 or 5x5x10 mm^3 in size were cut from the as-cast samples using a diamond saw. The samples were then ground using 400 grit SiC paper with water lubrication until all sides were flat and parallel. A compressive specimen is shown schematically in Figure 2.7.

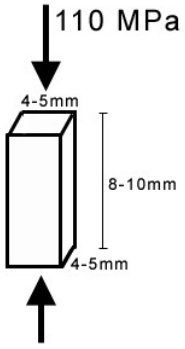

Figure 2.7 - Schematic of parallelepiped compression creep specimen.

Compression cages were inserted into two Arc-weld constant-load tensile creep frames for testing, Figure 2.8. The frames had a lever arm ratio of approximately 20:1. With the cages, a tensile load applied to the connecting rods moves the center platens

closer together, thus creating a compressive load on the specimen. The compressive cage assembly was placed into the frame with just enough tension applied to hold the assembly in place and still keep the lever arm level. A specimen was then loaded into the center of the platens. Care had to be taken to place the specimen as close to the center as possible; otherwise, uneven load distribution could result. The front crank was used to add minor tension to the assembly, bringing the platens just to rest on the top of the specimen, and the LVDT extensometer was recalibrated to zero strain (voltage) at this point. A clam shell furnace brought the assembly to the selected testing temperature (150-180°C), at which point the platform at the back of the frame was lowered to fully load the specimen to 110 MPa. Displacement was measured with a single attached LVDT (linear variable differential transducer), where displacement were indicated by a change in voltage recorded, and a LabView VI was used to convert this voltage to strain. In order to accurately measure temperature, a K type thermocouple was bent and inserted between the platens, so that it was contacting the creep specimen. Temperature variations of 1-2°C were observed during testing. Tests were interrupted after strain accumulation of 0.1 or after 400 hours, and specimens were cooled to room temperature under load to minimize rearrangement of dislocations generated during creep. For selected crept specimens, dislocation substructures that developed during testing were examined by TEM.

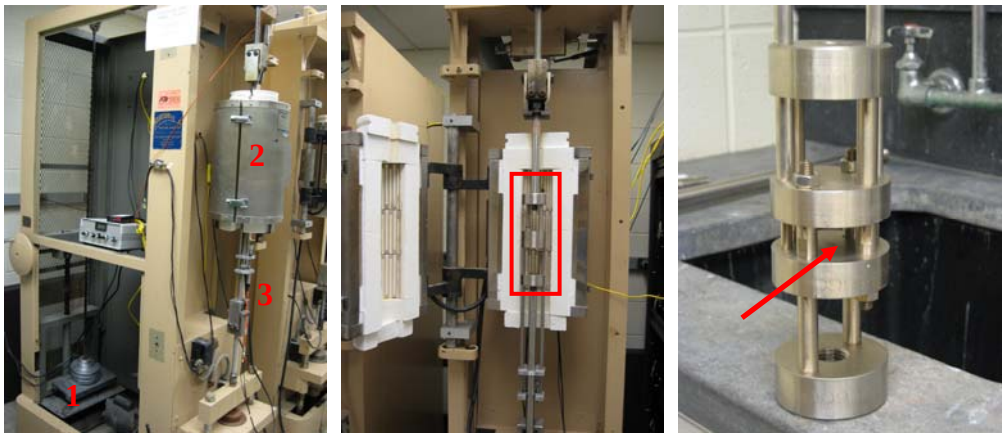

Figure 2.8 - Compression creep setup: a) Side view, showing loading platform (1), furnace (2) and LVDT (3) during a test, b) view inside the clam shell furnace prior to loading, c) close-up of the compression cage, highlighted by the red rectangle in b). The arrow indicates where the specimen is placed.

References

[1] N. D. Saddock, Ph.D. thesis, University of Michigan (Ann Arbor, MI), **2007**.

[2] N. D. Saddock, A. Suzuki, J. R. TerBush, E. C. Heininger, J. Zindel, J. E. Allison, T. M. Pollock, J. W. Jones, in *Magnesium Technology 2006* (Eds.: A. A. Luo, N. R. Neelameggham, R. S. Beals), TMS, San Antonio, TX, **2006**, pp. 77.

[3] N. D. Saddock, A. Suzuki, J. R. TerBush, J. W. Jones, T. M. Pollock, J. E. Zindel, J. E. Allison, *SAE Technical Paper 2007-01-1027*, SAE International, Detroit, MI, **2007**.

[4] M. Gungor, *Metallurgical Transactions A* **1989**, *20*, 2529.

[5] S. Tin, T. M. Pollock, W. Murphy, *Metallurgical and Materials Transactions A* **2001**, *32*, 1743.

[6] S. C. Huang, L. Peluso, D. Backman, in *Solidification* (Eds.: W. H. Hofmeister, J. R. Rogers, N. B. Singh, S. P. Marsh, P. W. Vorhees), TMS, **1999**, pp. 163.

[7] *ASM Handbook, Vol. 3 - Alloy Phase Diagrams*, ASM International, **1992**.

Chapter 3

Creep Deformation Behavior of Mg-Al-Ca-xSr-ySn Alloys

This chapter describes the creep behavior of several alloys based on the Mg-Al-Ca system. The differences observed in their creep resistance are discussed in terms of microstructure and the dislocation substructures that develop during creep. The behavior of the commercial alloys studied motivated investigations of elemental partitioning, described in more detail in Chapter 4, as well as an investigation of alloys with systematic variations in Mg, Al, Ca and Sn that will be discussed in Chapter 5.

3.1 Creep Behavior of Mg-Al-Ca-based Alloys

As part of USAMP's Magnesium Powertrain Cast Component (MPCC) program [1], the creep behavior of nine alloys considered for inclusion in a prototype automotive powertrain was evaluated. Three of these alloys were selected for the study described in this chapter: AXJ530 (developed by General Motors) and MRI230D and MRI153M (developed by Dead Sea Magnesium). All three alloys are based on the Mg-Al-Ca system, which has shown promise for die-cast powertrain applications [2]. The two MRI alloys were selected in part because of their potential for automotive application; they were selected for prototype engine components in the USAMP program [1]. Importantly for the purposes of the current study, the three alloys came from the same region of the ternary Mg-Al-Ca phase diagram, where the effect of composition, Table 3-1, on microstructure and creep behavior could be systematically examined. Aluminum concentration ranged from approximately 5% in AXJ530 to 8% in MRI153M, while calcium content varied from 3% to 1%, respectively. It is important to note that MRI230D also contained approximately 0.8% tin.

Table 3-1 – Compositions (wt%) of Mg-Al-Ca-xSr-ySn alloys, determined by ICP (courtesy of B.R. Powell)

Alloy	Mg	Al	Ca	Mn	Sr	Zn	Sn
AXJ530	Bal.	4.81	3.02	0.30	0.17	< 0.01	< 0.01
MRI230D	Bal.	6.45	2.25	0.27	0.25	< 0.01	0.84
MRI153M	Bal.	7.95	0.98	0.20	0.27	< 0.01	< 0.01

Figure 3.1 shows three representative creep curves for specimens of die-cast AXJ530, MRI153M, and MRI230D tested in tension at 110 MPa and temperatures of 100 and 180°C. At 100°C, the creep behavior of AXJ530 and MRI230D is similar and the curves have the same basic shape. Furthermore, the minimum creep rates for both alloys, listed in Table 3-2, differ by a factor of only 1.5-2. MRI153M is significantly less creep resistant, even at this low temperature, and has a minimum creep rate an order of magnitude higher than AXJ530 and MRI230D. At 100°C, the creep tests were interrupted after 500 hours, so the true minimum creep rate may not have been reached. At 180°C, AXJ530 and MRI230D have similar creep rates, again differing by approximately a factor of 1.5-2, although the creep curves have a slightly different shape since AXJ530 has a much longer secondary creep regime than MRI230D in the test shown. MRI153M is much less creep resistant at this temperature, and creep failure occurred after only 6 hours at 110 MPa. MRI153M exhibits a minimum creep rate two orders of magnitude higher than the other two alloys at this temperature. As will be discussed in Chapter 4, this difference in creep behavior was attributed to differences in the local concentration of the α-Mg phase, caused by elemental partitioning during solidification. It is worth noting that MRI153M has been intentionally designed for lower creep resistance in favor of improvements in other properties, e.g. higher strength. The creep resistance of MRI153M is still superior to that of AZ91 or AM60 [3] however.

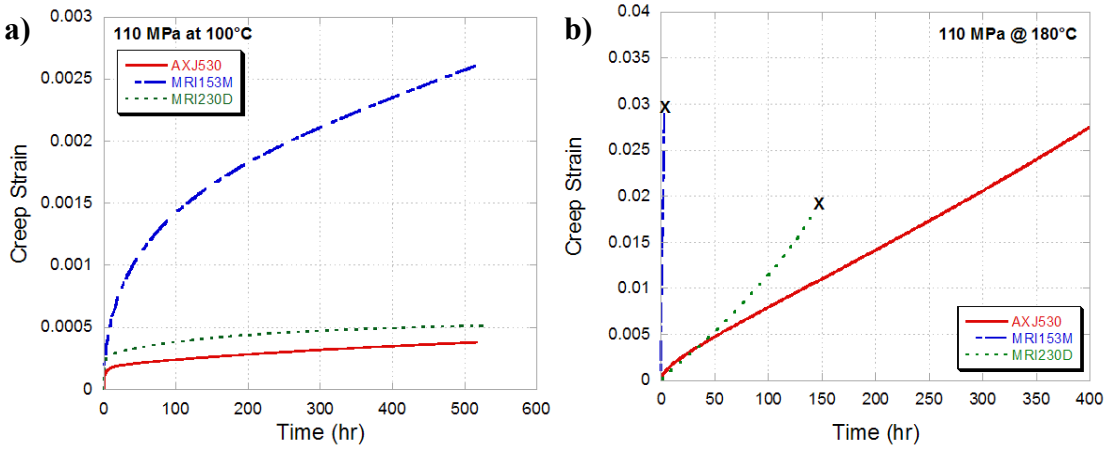

Figure 3.1 - Representative creep curves for AXJ530, MRI153M and MRI230D tested at 110 MPa at: a) 100° and b) 180°C. The specimens shown in a) did not fail, but were interrupted after 500 hours of testing.

Table 3-2 - Creep test statistics for selected specimens tested at 110 MPa

Alloy	Stress (MPa)	T (°C)	Time at end (h)	Strain at end (%)	Rupture?	Minimum creep rate (s^{-1})
AXJ530	110	100	516.8	0.04	N	6.68×10^{-11}
	110	180	517.5	3.64	N	1.71×10^{-8}
MRI153M	110	100	514.7	0.26	N	6.08×10^{-10}
	110	180	3.1	2.90	Y	1.21×10^{-6}
MRI230D	110	100	524.5	0.05	N	3.70×10^{-11}
	110	180	37.8	0.70	Y	3.91×10^{-8}
	110	180	144.2	1.85	Y	2.73×10^{-8}

3.2 Tensile Properties of AXJ530, MRI230D and MRI153M

Tensile tests were also conducted as part of the USAMP program. Tests were conducted at room temperature and 180°C in the as-die-cast condition, and at RT temperature for samples aged 1000 hours at 180°C. Stress-strain curves for all three conditions are presented in Figure 3.2 for AXJ530, MRI153M and MRI230D. The yield strength, ultimate tensile strength, Young's Modulus and elongation to failure are compared in Figure 3.3. For the as-cast samples, MRI153M has the highest strength at both room and elevated temperature, while AXJ530 has the lowest. After aging, however, this trend is reversed: AXJ530 has the highest strength and MRI153M the lowest. MRI153M also has the smallest increase in strength from the as-cast to aged condition, while MRI230D and AXJ530 show a greater increase in strength produced by

aging. The aging behavior of these alloys will be examined in more detail in Chapter 4. Interestingly, the creep resistance is negatively correlated to as-cast tensile strength, but is positively correlated with aged tensile strength.

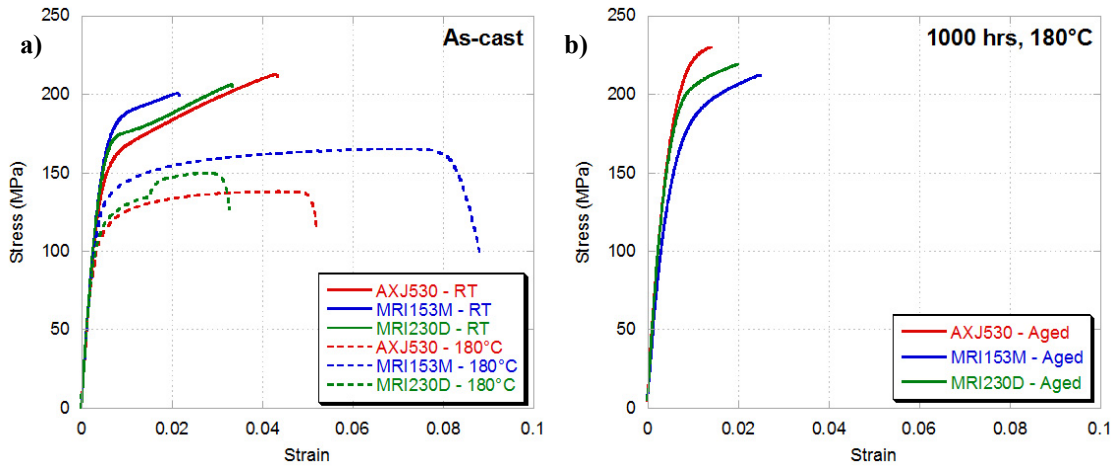

Figure 3.2 - Tensile stress-strain curves for a) as-cast and b) aged samples of AXJ530, MRI153M and MRI230D. The data presented is the average of 15 tests for each condition.

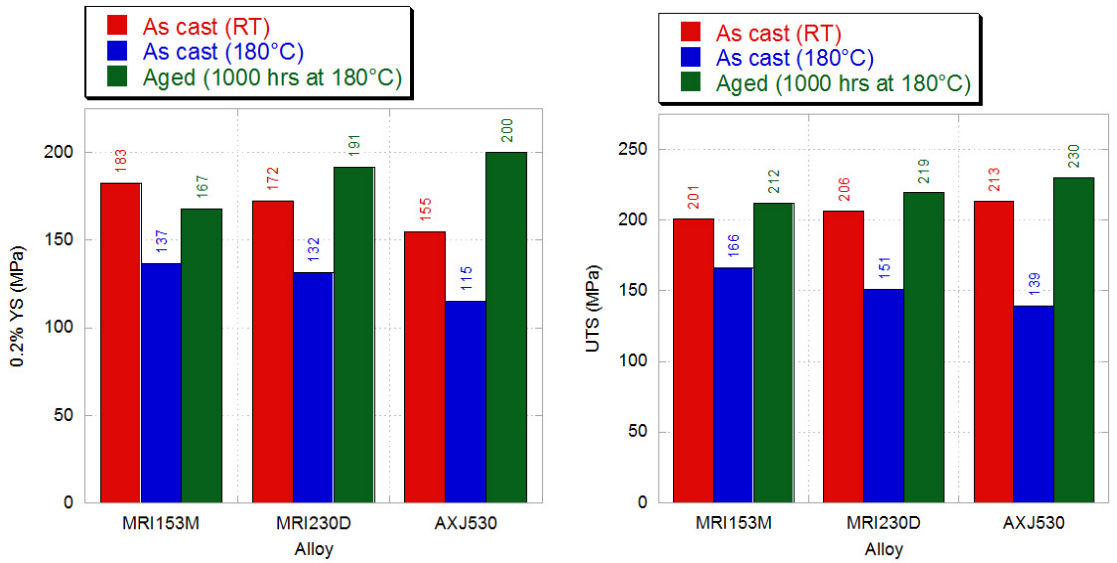

Figure 3.3 - Tensile properties of AXJ530, MRI153M and MRI230D in both the as-cast and aged state: a) Yield Strength, b) Ultimate Tensile Strength, c) Modulus, and d) Elongation to Failure. Figure continued on next page.

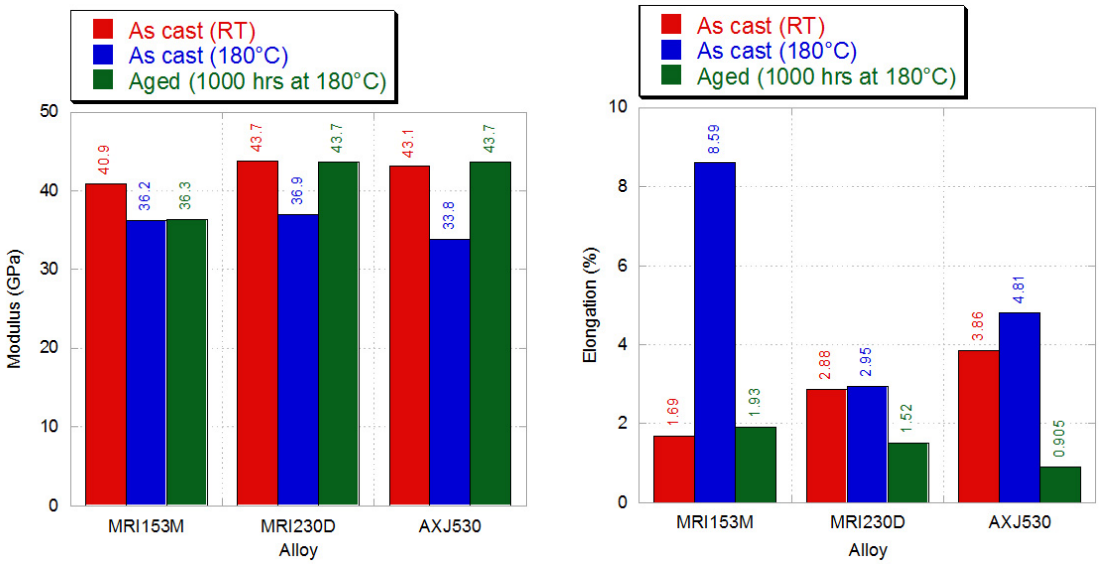

Figure 3.3 continued - Tensile properties of AXJ530, MRI153M and MRI230D in both the as-cast and aged state: a) Yield Strength, b) Ultimate Tensile Strength, c) Modulus, and d) Elongation to Failure.

3.3 Microstructure of Die-cast AXJ530, MRI230D and MRI153M

Microstructures were examined to determine if the differences in creep rate that were observed for AXJ530, MRI230D and MRI153M could be attributed to differences in phase type or grain/cell size between alloys, Figure 3.4. Samples were cut from the grip section of crept die-cast samples, and images were made of the core region using the back-scattered electron (BSE) detector in the SEM. In each of these alloys, the microstructure consists of cells of primary α-Mg (dark gray contrast) surrounded by intermetallic(s) in the interdendritic regions. The composition of the three alloys is indicated on the liquidus surface shown in Figure 3.5, adapted from Suzuki [4]. Note that all three alloys fall into the same compositional field initially. Based on previous studies and the liquidus surface published by Suzuki et al. [4], the predominant intermetallic phase has been identified as $(Mg,Al)_2Ca$ with a dihexagonal C36 structure. This has also been experimentally confirmed for the two MRI alloys using selected area diffraction (SAD) in the TEM, Figure 3.6. Because the same major intermetallic phase exists on the cell boundaries for these alloys, the differences in creep behavior cannot be attributed to the phases present in the interdendritic region.

Saddock observed that the creep rate for AXJ530 was dependent on the grain/cell size of the alloy [5]. Permanent mold cast specimens solidified with a slower rate and larger cell size and had a minimum creep rate that was an order of magnitude higher than

for the faster cooled die-cast specimens with smaller cell size [5]. The average cell size for all three alloys in the current study was approximately 11 μm as determined by the linear intercept method. The average grain size for die-cast AXJ530 was reported to be approximately 20 μm and based on EBSD scans, a grain may be comprised of more than one cell in this alloy [5]. The grain sizes for MRI230D and MRI153M were not measured. However, given that the alloys in this study were processed with comparable casting parameters, the grain size is not expected to vary significantly for the specimens examined, and the observed differences in creep resistance cannot be explained by grain size differences.

3.4 Dislocation Substructures of the Crept Specimens

Dislocation substructures produced by creep at 100°C and 180°C at a stress of 110 MPa were examined for specimens of AXJ530, MRI230D and MRI153M. Accumulated creep strain and test duration are listed in Table 3-2, along with minimum creep rate after 500 hours for each of the selected specimens. For some specimens, especially those tested at the lower temperature, this may not be the true minimum creep rate since 500 hours was not always sufficient to reach the true minimum.

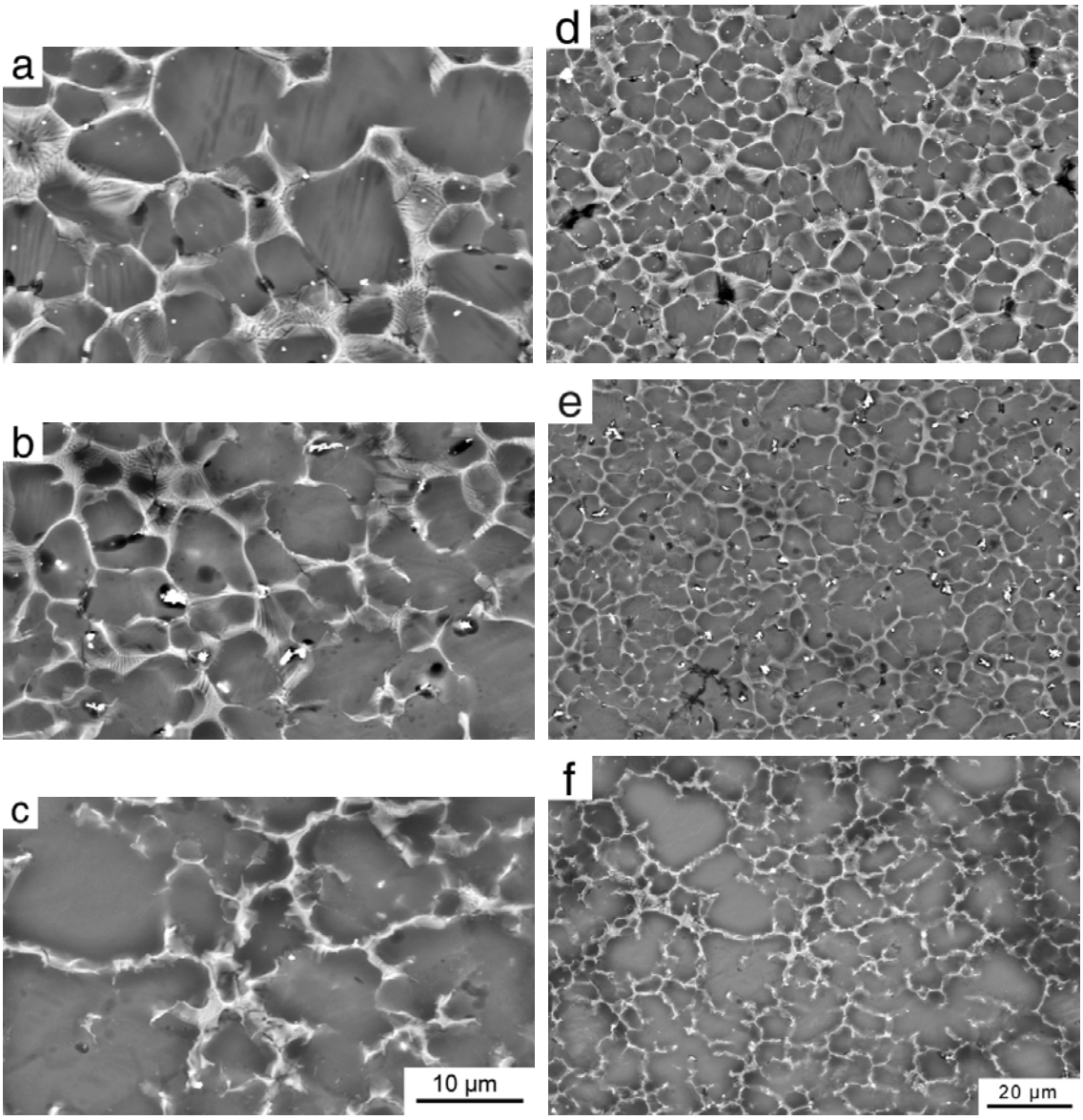

Figure 3.4 – SEM (BSE) micrographs of die-cast specimens of: a) AXJ530, b) MRI230D and c) MRI153M. d-f) Same alloys, but at a lower magnification. All specimens were etched for 5s prior to imaging.

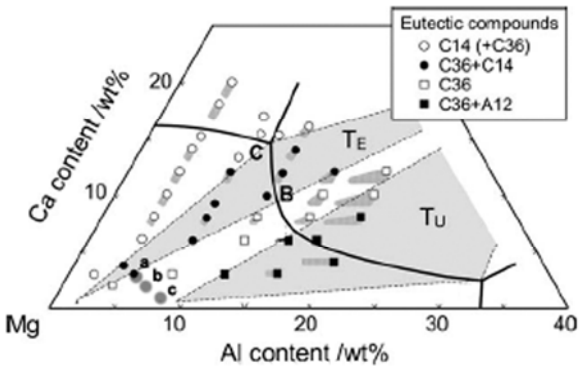

Figure 3.5 - Liquidus projection of the Mg-Al-Ca system [4], including expected eutectic phases. The compositions of the three alloys studied are indicated: a) AXJ530, b) MRI230D and c) MRI153M.

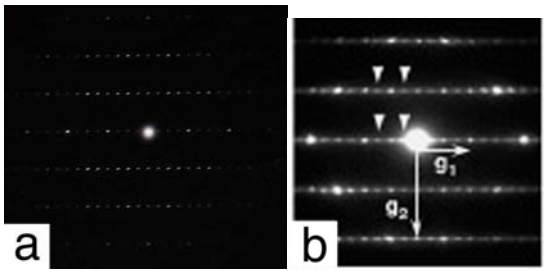

Figure 3.6 - a) SAD pattern from C36 phase, taken from a foil of MRI230D. b) C36 diffraction pattern from AXJ530 [6], with the extra spots of the dihexagonal phase indicated by the arrows.

3.4.1 Analysis of Specimens Crept at 110 MPa and 100°C

Bright field (BF) TEM images taken from a zone axis of $[11\bar{2}0]$ are shown in Figure 3.7 for a specimen of AXJ530. This specimen had accumulated 0.04% creep strain when the test was interrupted after 500 hours. The image in Figure 3.7a was made with $\mathbf{g} = (1\bar{1}01)$, while that shown in Figure 3.7b used $\mathbf{g} = (0002)$. Under the conditions in Figure 3.7a, all dislocation types are visible. However, under the conditions in Figure 3.7b, <a> type dislocations are invisible, and any dislocations present in this image are therefore either <c> or <c+a> type dislocations. Examining Figure 3.7b, no dislocations are present under the second set of conditions, indicating that the dislocations visible in Figure 3.7a are all <a> type dislocations. The majority of the dislocations present can be further identified as basal <a> type dislocations, since they lie parallel to the basal trace included in Figure 3.7a. Given the low testing temperature and low overall strains, this was anticipated, since the basal slip system is the primary one activated at low temperatures. There is no evidence of sub-grain or sub-boundary formation at this

temperature. Similarly, the dislocations present in Figure 3.7c can be identified as <a> type dislocations after comparison with Figure 3.7d. Again, comparison with the basal trace shows they are basal <a> dislocations.

In Figure 3.7a, it can also be seen that the dislocations observed primarily lie in the near-interdendritic region; the dislocations are confined to the α-Mg and do not appear to interact with the intermetallic phase (band of dark contrast) in the interdendritic region. In Figure 3.7c, however, the dislocations were located in the cell interiors. A more systematic study of this phenomenon is needed before any conclusions can be drawn on the behavior of near-boundary vs. grain interior areas and any differences that may exist between dislocation densities in the two areas. Although little interaction was observed in Figure 3.7a, some interaction must occur between dislocations in the α-Mg phase and the intermetallic phases in the interdendritic region for continuous deformation to occur.

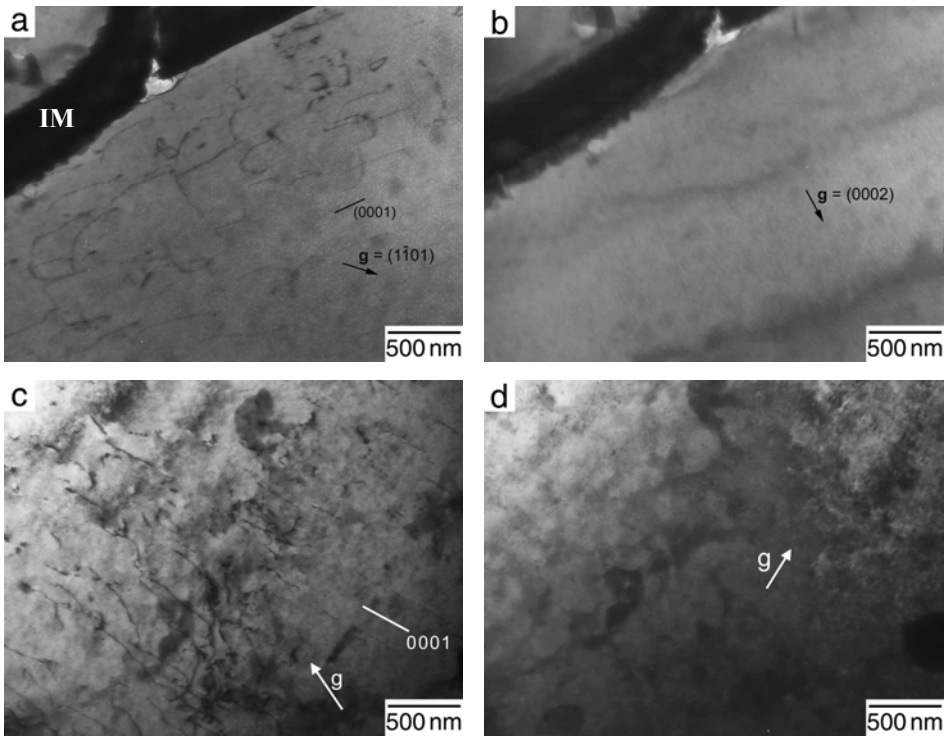

Figure 3.7 – BF TEM images of an AXJ530 specimen crept at 110 MPa and 100°C - test discontinued after 517 h and creep strain of 0.04%. Zone axis = $[11\bar{2}0]$. a and c) g = $(1\,\bar{1}\,01)$, b and d) g = (0002). Images taken within the α-Mg cells. IM = intermetallic phase.

In Figure 3.8, BF TEM images from a specimen of MRI153M that had accumulated 0.26% creep strain when the test was stopped after 500 hours are shown. BF TEM images from a specimen of MRI230D tested under these same conditions are shown in Figure 3.9. In this instance, the specimen had accumulated 0.05% creep strain when the test was stopped after 500 hours. Again, in both Figure 3.8 and 3.9 the majority of the dislocations present are basal <a> type dislocations. For the MRI153M, a limited number of non-basal <a> type dislocations are also present. These are visible in Figure 3.8c as dislocations not parallel to the basal trace.

In some of the TEM images from the crept MRI230D specimens, Figure 3.9a-d, spherical features are present. There is evidence that the <a> dislocations present can interact with these features, as indicated by the block arrow in Figure 3.9a. However, these features were not observed in every foil (Figure 3.9e-f), and are believed to be artifacts, perhaps from foil preparation or degradation. They were also not observed at higher temperatures, Figure 3.10.

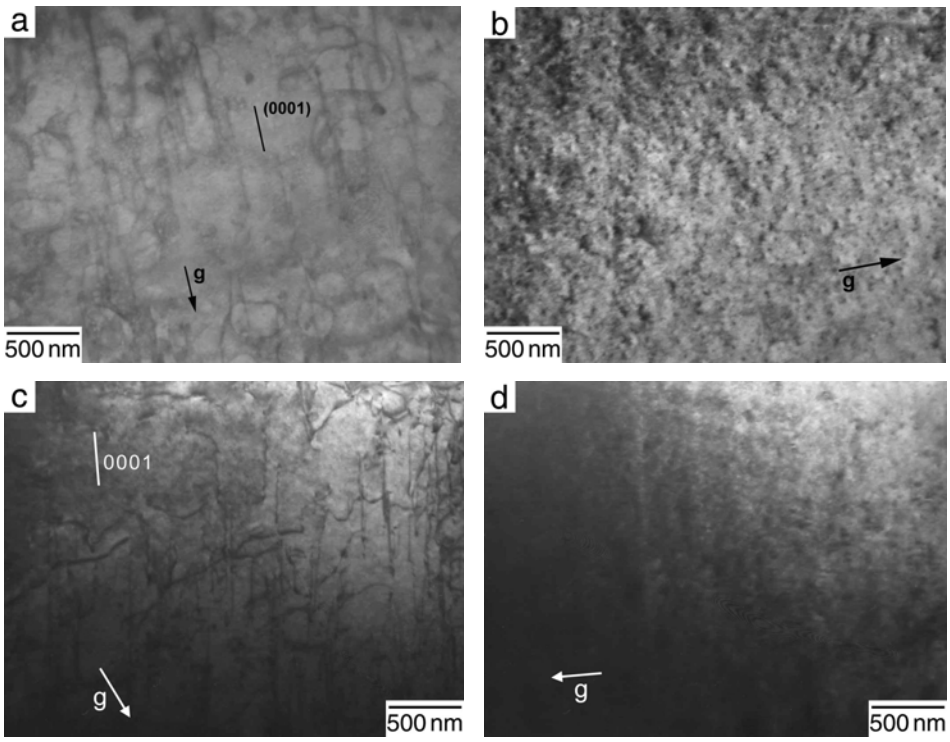

Figure 3.8 – BF TEM images of an MRI153M specimen crept at 110 MPa and 100°C – test discontinued after 514 h and creep strain of 0.26%. Zone axis = $[11\bar{2}0]$**. a) g =** $(\bar{1}100)$**, b and d) g =** (0002) **and c) g =** $(1\bar{1}01)$**.**

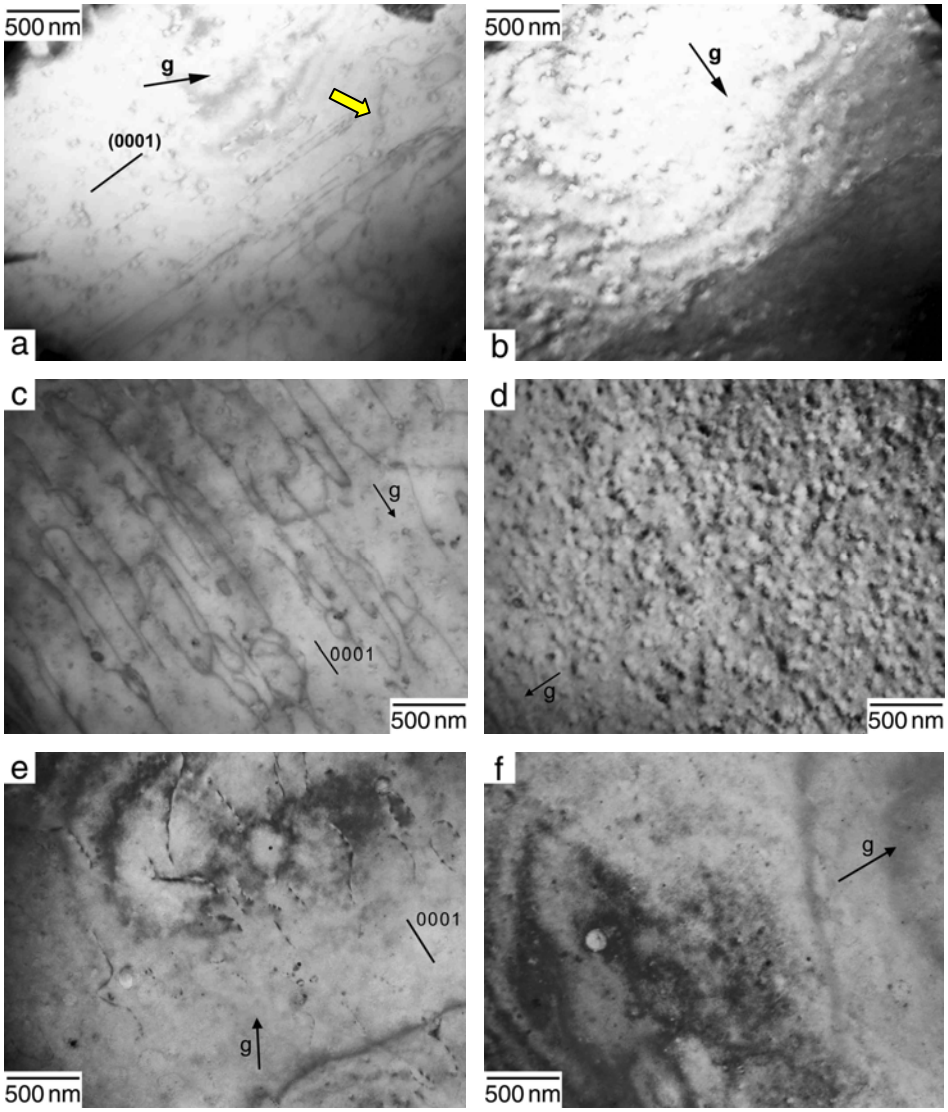

Figure 3.9 – BF TEM images of an MRI230D specimen crept at 110 MPa and 100°C – test discontinued after 524 h and creep strain of 0.05%. Zone axis = $[11\bar{2}0]$**. a and e) g =** $(1\,\bar{1}\,01)$**, b,d and f) g =** (0002) **and c) g =** $(\bar{1}100)$**.**

3.4.2 Analysis of Specimens Crept at 110 MPa and 180°C

A zone axis of $[11\bar{2}0]$ was also used to examine the dislocations present for specimens tested at 110 MPa and 180°C. BF TEM images from a specimen of MRI230D that ruptured after approximately 38 hours and a creep strain of 0.70% are shown in Figure 3.10. In this instance, Figure 3.10a was taken with **g** = $(\bar{1}101)$, while Figure 3.10b was made with **g** = (0002). Again, any <a> dislocations present would be invisible in Figure 3.10b and visible in Figure 3.10a. Thus, by comparing the two images, the

majority of the dislocations present are identified as <a> type dislocations. Dislocations oriented parallel to the basal trace are basal <a> dislocations, while those not parallel are non-basal <a> dislocations, most likely moving on prismatic or pyramidal planes. However, unlike at 100°C, there are also dislocations visible in Figure 3.10b and 3.10d, indicating that some <c> or <c+a> dislocations are present. The dislocations are mostly randomly distributed in the α-Mg cell, although an isolated sub-boundary may be present in Figure 3.10c-d.

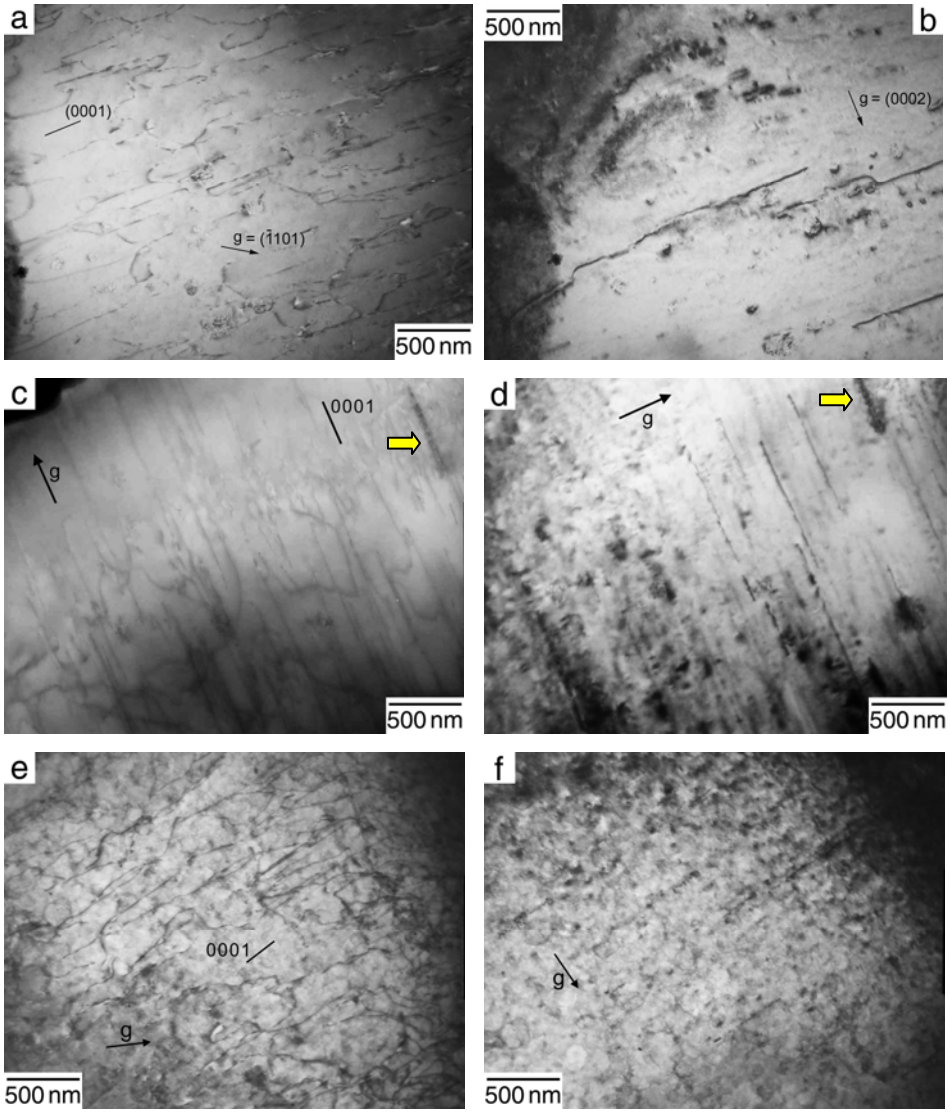

Figure 3.10 - BF TEM images of an MRI230D specimen crept at 110 MPa and 180°C – specimen failed after 38 h and creep strain of 0.7%. Zone axis = $[11\bar{2}0]$. a and e) g = $(1\bar{1}01)$, b,d and f) g = (0002) and c) g = $(\bar{1}100)$. Possible sub-boundary indicated by yellow block arrow in c) and d).

TEM images of a specimen of AXJ530 crept under these same conditions are shown in Figure 3.11. This specimen accumulated 3.64% creep strain before the test was terminated at 500 hours. The images in Figure 3.12 are from a specimen of MRI153M that ruptured after approximately 3 hours and 2.90% creep strain. Again, the majority of the dislocations present are <a> type, both basal and non-basal, with a limited number of <c> or <c+a> dislocations also present. Qualitatively, the sample of MRI153M appears to have a greater number of gliding dislocations compared with the other two alloys, although this also varies on a grain-to-grain basis for a particular alloy.

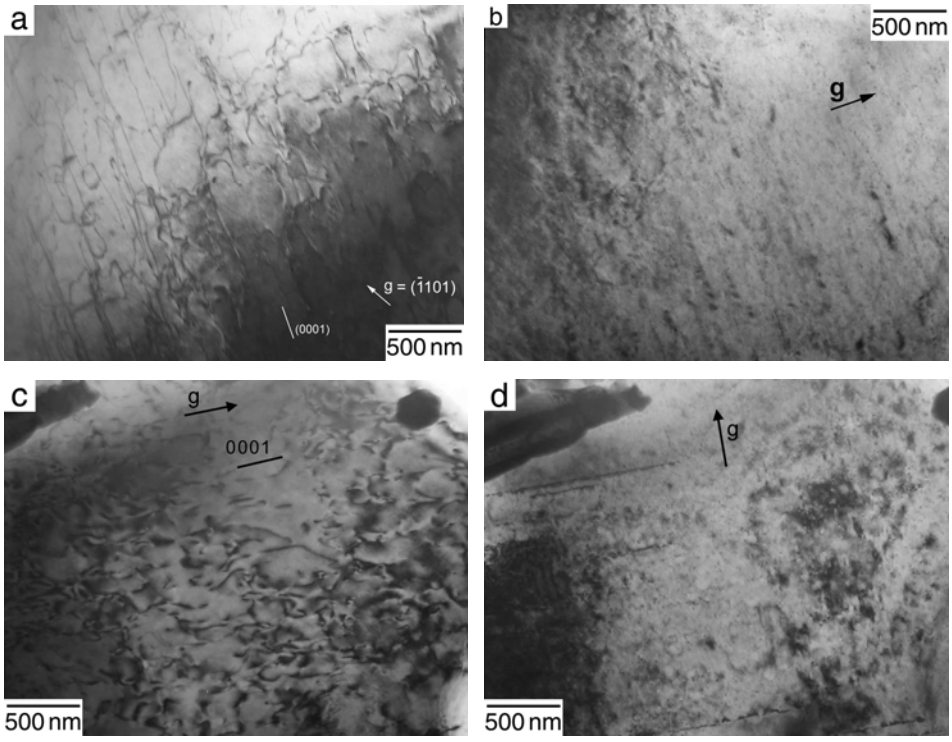

Figure 3.11 - BF TEM images of an AXJ530 specimen crept at 110 MPa and 180°C - test discontinued after 517 h and creep strain of 3.6%. Zone axis = $[11\bar{2}0]$**. a) g =** $(1\bar{1}01)$**, b and d) g =** (0002) **and c) g =** $(\bar{1}100)$**.**

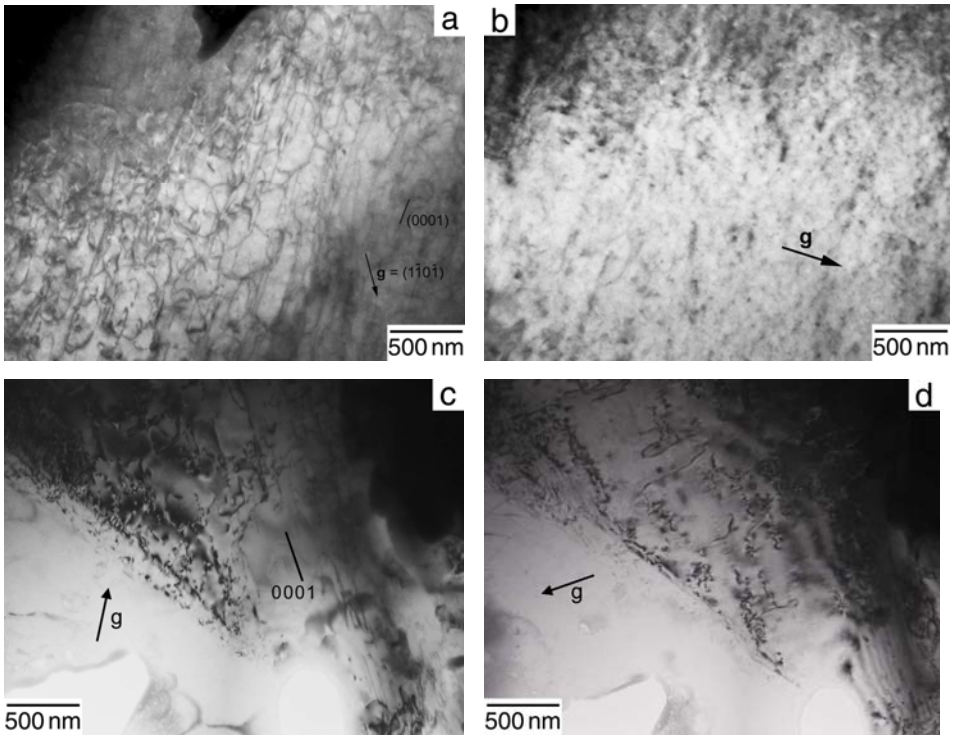

Figure 3.12 - BF TEM images of an MRI153M specimen crept at 110 MPa and 180°C – specimen failed after 3.1 h and creep strain of 2.9%. Zone axis = $[11\bar{2}0]$**. a and c) g =** $(1\,\bar{1}\,01)$**, b and d) g =** (0002)**.**

3.4.3 Dislocation Substructures and Creep Deformation Mechanisms

Despite the differences in the nominal aluminum and calcium concentrations in the three alloys and the presence of tin in the MRI230D, the dislocation substructures produced by creep are similar, with the same types of dislocations observed. At 180°C, the majority of the dislocations present are <a> dislocations, both basal and non-basal, with a limited number of <c> or <c+a> dislocations also present. And at 100°C, the majority of the dislocations are basal <a> dislocations, although a limited number of non-basal <a> dislocations are also observed. A higher percentage of non-basal <a> and <c+a> dislocations were present at 180°C than at 100°C. A similar substructure consisting of a random distribution of <a> dislocations was observed in an Mg-0.8%Al solid solution alloy by Vagarali and Langdon [7]. In this study the creep mechanism was identified as viscous glide of basal dislocations; the same deformation mechanism appears to be operative for the Mg-Al-Ca-xSr-ySn alloys studied here. Further studies described in Chapter 5 identify viscous glide as the operative creep mechanism in quaternary Mg-Al-Ca-Sn alloys as well.

Saddock concluded that during the early stages of creep in Mg-Al-Ca alloys, strain accumulates in the α-Mg grains and is not strongly affected by cell boundaries [5]. Resistance to dislocation motion in the primary alpha magnesium is thus of greater importance to creep behavior than the influence of the interdendritic phases in these alloys. The creep resistance of the primary α-Mg phase will be influenced by presence of solute and/or precipitates in the grain interiors. Recent studies [8-11] have shown that thermally stable precipitates in the primary alpha Mg phase can increase the creep resistance of an alloy. For example, Suzuki et al. reported an increase in creep resistance by a factor of ~1.5-2 in die-cast AXJ530 that was aged at 250°C, with precipitation of Al_2Ca observed on basal planes [12]. However, Al_2Ca precipitates were not observed in the as-crept microstructures of these alloys under the current testing conditions. If creep rate is therefore controlled by viscous glide, which is affected by the atomic size difference, solute atom concentration, and diffusivity [13, 14], the differences in creep behavior observed here can be explained, at least in part, by differences in solute element and concentration, as was suggested by Nie [15]. Differences in elemental partitioning for these Mg-Al-Ca-based alloys will be examined in Chapter 4 through aging experiments and measurement of solute concentration. Elemental partitioning and the subsequent effect on creep rate will also be examined in Chapter 5 for model quaternary alloys based on the Mg-Al-Ca-Sn system, and the implications for solute and precipitation strengthening during creep in this system will be described.

3.5 Summary

Microstructure and dislocation substructures for die-cast AXJ530, MRI230D and MRI153M crept at 110 MPa were observed. The same major phases are observed for all three alloys: α-Mg and C36 $(Mg,Al)_2Ca$. Although the creep resistance differed by at least an order of magnitude between MRI153M and the other alloys, the dislocation substructures observed were similar for a given temperature, indicating that the same deformation mechanism is operative for all three alloys – viscous glide of <a> type dislocations. The differences in creep resistance observed are thus not due to differences in creep mechanism, major intermetallic phases present, or cell size. Solute

concentrations in the α-Mg phase will be examined in more detail in the next chapter to explain this difference in creep resistance.

References

[1] J. A. Hines, R. C. McCune, J. E. Allison, B. R. Powell, L. J. Ouimet, W. L. Miller, R. Beals, L. Kopka, P. P. Ried, *SAE Technical Paper 2006-01-0522*, SAE International, Detroit, MI, **2006**.

[2] A. A. Luo, *International Materials Reviews* **2004**, *49*, 13.

[3] S. M. Zhu, B. L. Mordike, J. F. Nie, *Metallurgical and Materials Transactions A* **2006**, *37A*, 1221.

[4] A. Suzuki, N. D. Saddock, J. W. Jones, T. M. Pollock, *Acta Materialia* **2005**, *53*, 2823.

[5] N. D. Saddock, Ph.D. thesis, University of Michigan (Ann Arbor, MI), **2007**.

[6] A. Suzuki, N. D. Saddock, J. W. Jones, T. M. Pollock, *Scripta Materialia* **2004**, *51*, 1005.

[7] S. S. Vagarali, T. G. Langdon, *Acta Metall.* **1982**, *30*, 1157.

[8] A. Suzuki, N. D. Saddock, J. R. TerBush, B. R. Powell, J. W. Jones, T. M. Pollock, in *Magnesium Technology 2007* (Eds.: R. S. Beals, A. A. Luo, N. R. Neelameggham, M. O. Pekguleryuz), TMS, Orlando, FL, **2007**, pp. 375.

[9] X. Gao, S. M. Zhu, B. C. Muddle, J. F. Nie, *Scripta Materialia* **2005**, *53*, 1321.

[10] J. F. Nie, X. Gao, S. M. Zhu, *Scripta Materialia* **2005**, *53*, 1049.

[11] M. Vogel, O. Kraft, E. Arzt, *Scripta Materialia* **2003**, *48*, 985.

[12] A. Suzuki, N. D. Saddock, J. R. TerBush, B. R. Powell, J. W. Jones, T. M. Pollock, *Metallurgical and Materials Transactions A* **2008**, *39A*, 696.

[13] M. E. Kassner, M.-T. Perez-Prado, *Fundamentals of Creep in Metals and Alloys*, 1st ed., Elsevier, Amsterdam, **2004**.

[14] A. H. Cottrell, M. A. Jaswon, *Proceedings of the Royal Society of London. Series A, Mathematical and Physical Sciences* **1949**, *199*, 104.

[15] J. F. Nie, *Scripta Materialia* **2003**, *48*, 981.

Chapter 4

Aging Behavior and Elemental Partitioning of Mg-Al-Ca-xSr-ySn Alloys

In Chapter 3, viscous glide of dislocations was identified as the operative creep mechanism for three die-cast alloys based on the Mg-Al-Ca ternary system. Creep behavior for these alloys necessarily depends primarily on dislocation motion in the primary alpha-Mg, which means that creep resistance can be influenced by solute and precipitation strengthening. Because both processes are dependent on the concentration and distribution of key elements (e.g. Al and Ca) produced during solidification, a systematic investigation of elemental partitioning and aging behavior in AXJ530, MRI230D and MRI153M was conducted to better understand the origin of the differences in creep behavior that were observed.

The distribution of elements in the final solidified structure was first examined using EDS mapping for a specimen of MRI230D to provide insight into the microsegregation behavior of this alloy. To better understand the possibility of precipitation strengthening from Al and Ca in the primary α-Mg, the aging behavior of the commercial Mg-Al-Ca-based alloys was examined. Aging allows observation of the formation and growth of precipitate phases, and provides qualitative information on the solute content of the alpha-Mg phase. In MRI230D and AXJ530 precipitates of Al_2Ca formed during the aging process, while β-$Mg_{17}Al_{12}$ formed in MRI153M, indicating differences in Al and Ca concentrations in the primary α-Mg cells of the alloys. Partitioning of elements during solidification was therefore examined in greater detail for the alloys using electron microprobe measurements of composition. Increased partitioning of Al and Ca was observed in the Sn-containing MRI230D, which motivated further studies, described in Chapter 5, on the effect of Sn additions on elemental partitioning in the ternary Mg-Al-Ca system.

4.1 Distribution of Elements in Remelted MRI230D

The distribution of elements in recast MRI230D was examined using the EDS (energy dispersive spectroscopy) mapping capabilities of the Quanta dual beam SEM/FIB. The spectrum generated for this analysis is shown in Figure 4.1. To facilitate later compositional analysis, a die-cast sample of MRI230D was remelted with an induction furnace and crucible described in Chapter 2 and solidified at a slower cooling rate to obtain a sample with a larger average cell size, Figure 4.2a, than that produced by die-casting. The EDS maps collected from this sample are shown in Figures 4.2b-i. Mg is predominantly measured in the alpha phase as expected, although lower levels of Mg are present in some of the intermetallic phases, Figure 4.2b. The majority of the Al and Ca measured in Figures 4.2c and 4.2d is found in the C36 phase, although there may also be some enrichment in the α-Mg phase near the cell boundaries. From Figures 4.2c and 4.2f, some of the intermetallic observed in the SEM image (Figure 4.2a) is an Al-Sr phase, possibly Al_4Sr [1-3]. Likewise, Figures 4.2d and 4.2e indicate that the bright white phase observed in the SEM micrograph is a Ca-Sn phase, likely the $Ca_{2-x}Mg_xSn$ phase reported by Kozlov et al. [4, 5]. The other bright contrast phase appears to be an Al-Mn phase, Figures 4.2c and 4.2g. Oxygen and carbon, shown in Figures 4.2h and 4.2i, respectively, are surface contaminants for Mg alloys. Some oxygen is observed over the entire surface, although slightly higher concentrations are measured near the intermetallic phases, especially the Sn-containing phases. The carbon in Figure 4.2i is likely from the colloidal graphite used to coat the epoxy mount prior to SEM observation or a result of deposition from the electron beam.

The phases inferred from EDS mapping can be compared with thermodynamic predictions using the Pandat Mg8 database. The equilibrium phase predictions are shown in Figure 4.3. The volume fraction of each phase from a Scheil prediction, which more accurately reflects the non-equilibrium cooling rates featured in the casting process and the dendritic structure that is observed, are given in Table 4-1. The expected major phases (α-Mg, C36/C15, β-$Mg_{17}Al_{12}$, and Al_4Sr/τ-AlMgSr) correspond fairly well with the results of the EDS maps, although Pandat does predict some τ-AlMgSr along with Al_4Sr. The τ phase was identified by Janz et al., although the crystal structure of the phase was not determined [6]. The presence of Ca_2Sn is also predicted instead of

$Ca_{2-x}Mg_xSn$, but these phases have the same crystal structure, and the $Ca_{2-x}Mg_xSn$ phase is considered by some to be the ternary solid solution of Ca_2Sn [5]. The agreement is not as good between the volume fractions predicted and those observed experimentally. For example, little β-$Mg_{17}Al_{12}$ is observed in the area shown in Figure 4.2a. With the exception of C36, C15 and β-$Mg_{17}Al_{12}$, the volume fraction of most of the secondary phases present is predicted to be much less than 1%; even the most prevalent secondary phase, C36, has a predicted volume fraction of less than 3%. The very small volume fraction of secondary phases, combined with the submicron scale of any precipitates present, provides a challenge from the point of view of characterization.

Based on the EDS maps, Al, Ca and Sn segregate more strongly to the interdendritic region, while Mg preferentially partitions to the cell (dendrite) interiors as expected from the binary phase diagram. The magnitude of the segregation will be examined in more detail in Section 4.3, where microprobe measurements of elemental segregation will be described. The enrichment of Al and Ca that was observed in the primary α-Mg phase with the EDS map suggests that precipitation of Al_2Ca may be possible during high temperature exposure. This will be examined in Section 4.2 through an investigation of the aging behavior of MRI230D.

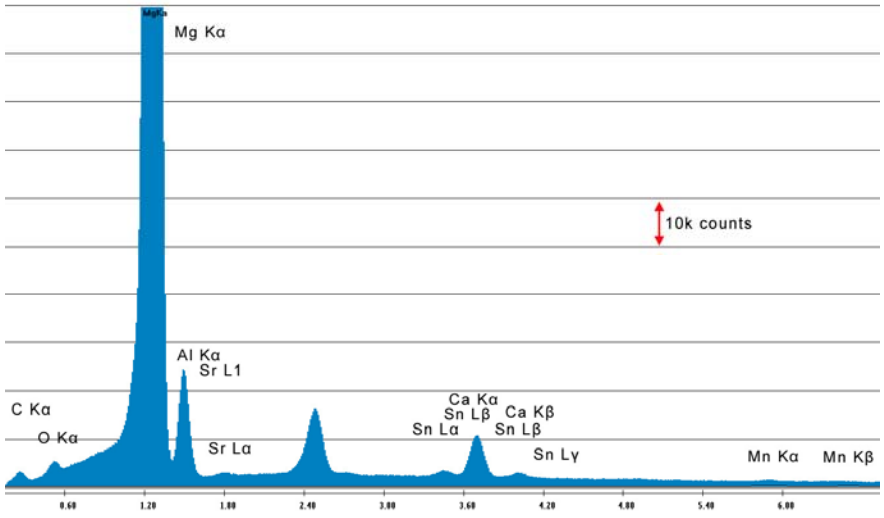

Figure 4.1 - EDS spectrum of the remelted MRI230D, at a voltage of 20kV and rate of 33k cps. The spectrum has been cropped to focus on the lower (weaker) peaks.

Table 4-1 - Pandat Scheil predictions of phase fractions in MRI230D

Phase	Al_8Mn_5	α-Mg	Ca_2Sn	C36 $(Mg,Al)_2Ca$	C15 (Al_2Ca)	Al_4Sr	$Al_{11}Mn_4$	Al_4Mn	τ-AlMgSr	β-$Mg_{17}Al_{12}$
Fraction	0.001	0.933	0.004	0.026	0.013	0.002	1.3×10^{-5}	7.7×10^{-6}	0.002	0.018

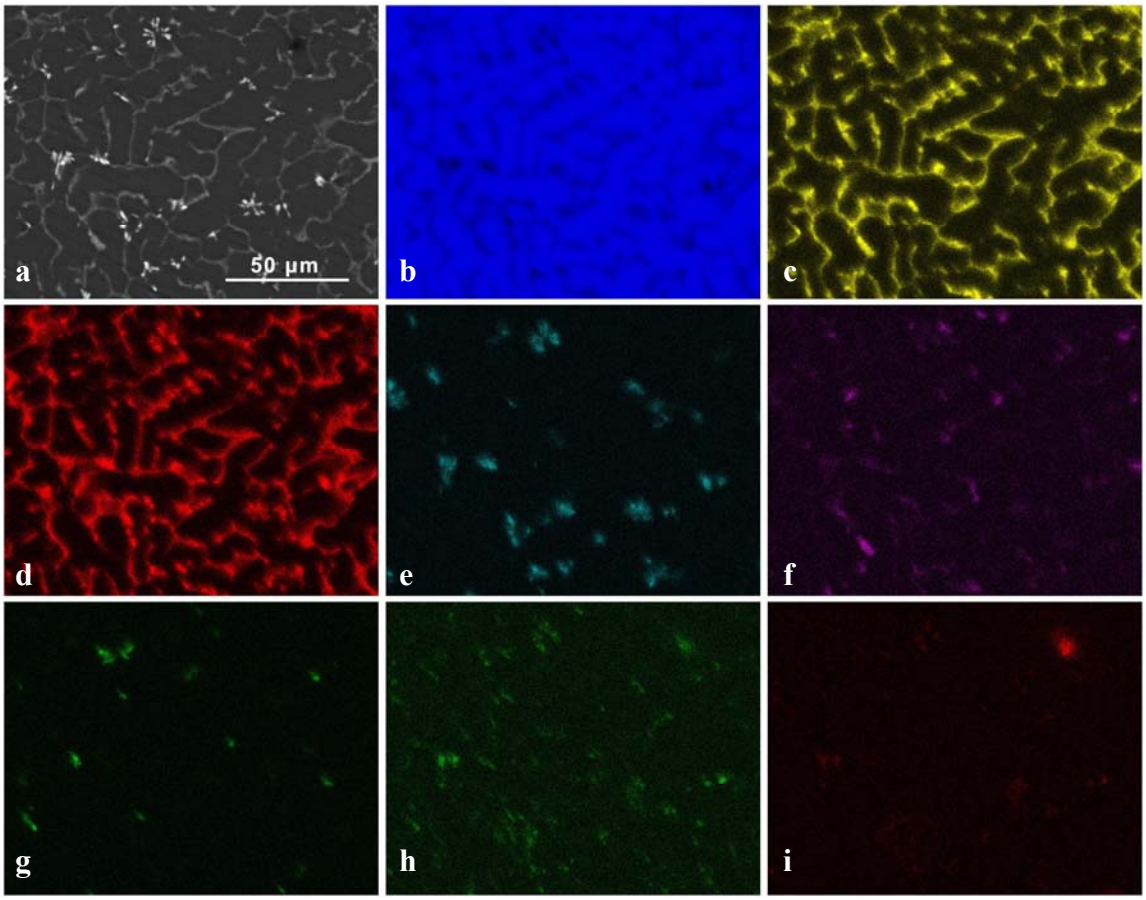

Figure 4.2 – EDS elemental maps of remelted MRI230D alloy: a) SEM BSE image, b) Mg, c) Al, d) Ca, e) Sn, f) Sr, g) Mn, h) O and i) C.

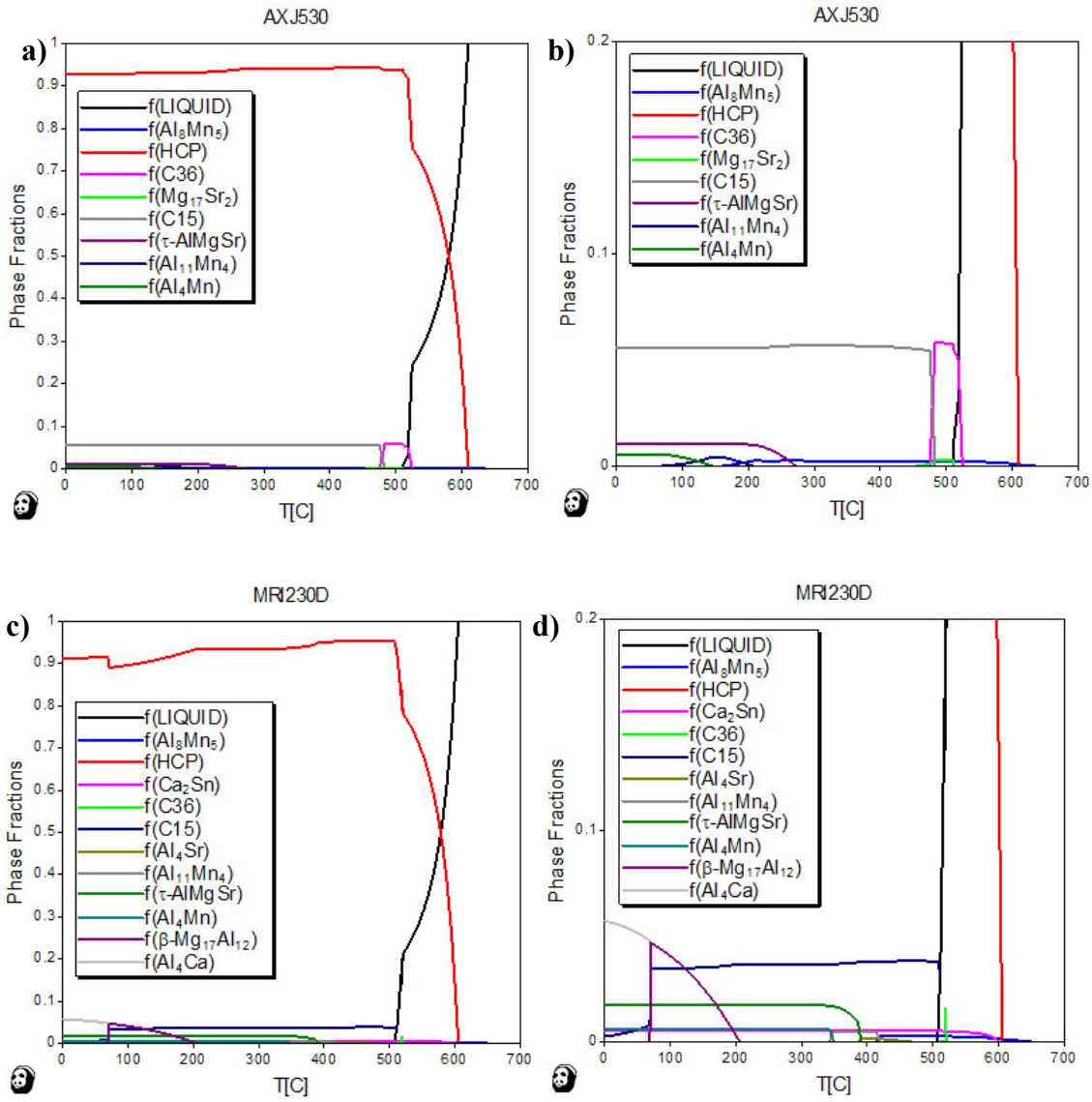

Figure 4.3 - Pandat predictions of equilibrium phase fractions for: a-b) AXJ530, c-d) MRI230D and e-f) MRI153M. b,d,f) Same plots, but focused lower phase fractions. Figure continues on next page.

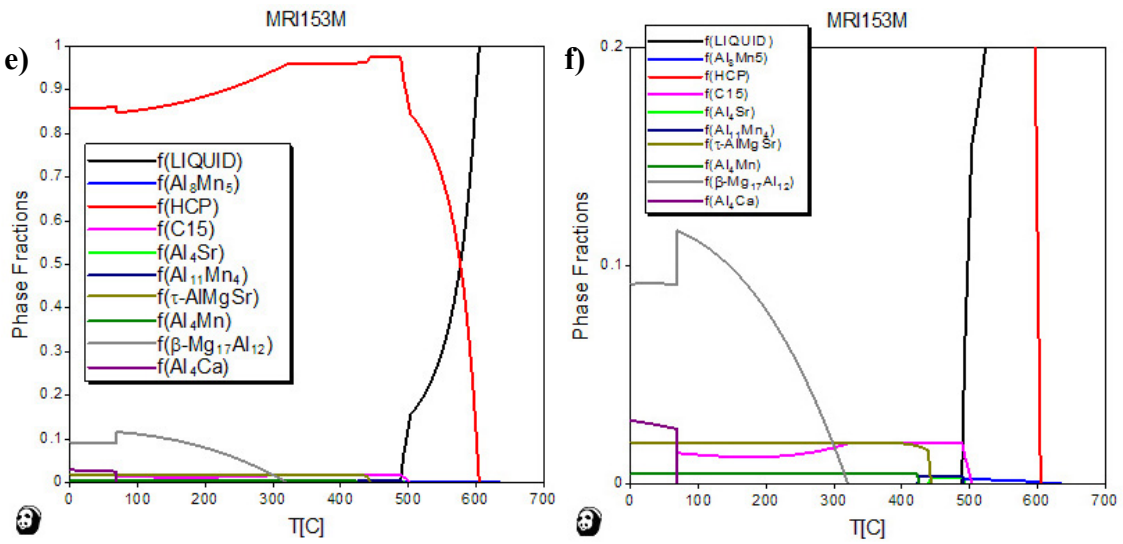

Figure 4.3 continued - Pandat predictions of equilibrium phase fractions for: a-b) AXJ530, c-d) MRI230D and e-f) MRI153M. b,d,f) Same plots, but focused lower phase fractions.

4.2 Aging Behavior

In an investigation of the creep behavior of permanent mold cast AXJ530 conducted by Saddock et al. [7], the minimum creep rates were found to vary by an order of magnitude over the range of mold temperatures used during casting. This was attributed to the formation of Al_2Ca precipitates in the primary α-Mg phase during the casting process. Higher mold temperatures were associated with lower creep resistance [7, 8]; the larger size and spacing of precipitates obtained at these higher temperatures created less effective obstacles to dislocation motion than at lower mold temperatures. An aging study conducted by Suzuki et al. showed that it was also possible to form precipitates of Al_2Ca in die-cast AXJ530, although these precipitates had a much smaller effect on creep resistance, decreasing the minimum creep rate by a factor of 1.5-2 [9]. The patent for MRI230D also mentions that the alloy exhibits "a marked response to aging at 250°C wherein… creep resistance increase [sic]." [10] No further details are given, however. The aging response and the details of the associated precipitation process may thus provide insight into the differences in creep resistance that were observed in die-cast AXJ530, MRI230D and MRI153M.

The variation in hardness of die-cast MRI230D with aging time and temperature is shown in Figure 4.4a. An average hardness of 68.4 Hv was measured in the as-cast state. For the aging times and temperatures used in our study, the peak hardness

measured was 74.7 Hv after aging 100 hours at 250°C, an increase of ~9%. The standard deviation ranged from ~2-6 Hv for the data set. Classical age hardening curves were observed, where the hardness initially decreases, increases up to a peak, and then decreases again with overaging. The peak position is approximated based on the experimental data; theoretically, the aging time to peak hardness should decrease for the higher temperatures (300-350°C). At higher temperatures, the increased diffusion rate combined with increased solid solubility of Al (Figure 4.5) and Ca, will lead to faster growth and coarsening of any precipitates present. MRI230D did not show significant aging hardening at 175°C for times up to 500 hours, which is approximately the temperature used for the creep tests shown in Figure 3.3 (180°C).

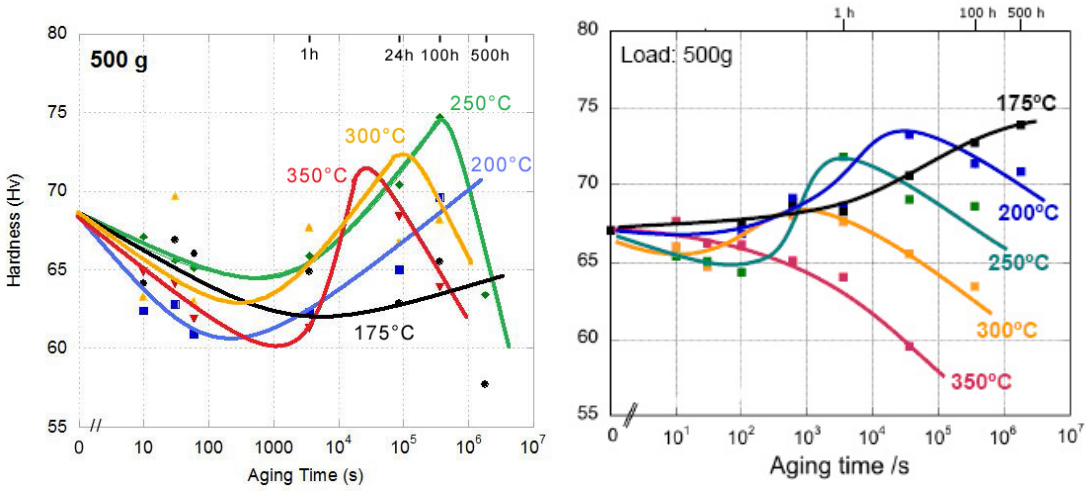

Figure 4.4 - Hardness variation with aging time and temperature for a) MRI230D and b) AXJ530 [11].

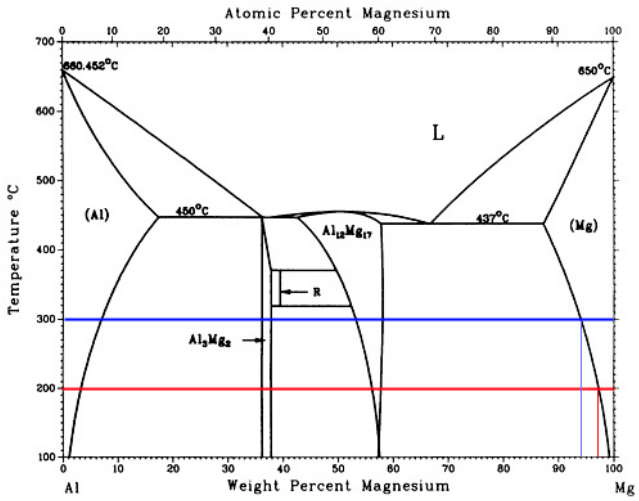

Figure 4.5 - Illustration of the variation in solute content with temperature. More solute is available at higher temperatures (blue line) than lower (red). Modified from [12].

The hardness of aged MRI230D was compared with the results of a similar study conducted by Suzuki et al. [11], Figure 4.4b. The hardness of both as-cast MRI230D and AXJ530 are very similar, at 68 and 67 Hv, respectively. The peak hardness observed for both alloys is similar, 74 Hv for MRI230D and approximately 73 Hv for AXJ530, an increase of ~9% for both alloys. Aging temperatures of 200-250°C yielded measurable changes in hardness for both alloys. However, the onset of overaging at these intermediate temperatures appears to be delayed in MRI230D compared with AXJ530. It is possible that the kinetics of precipitate coarsening leading to overaging is influenced by the presence of Sn in MRI230D if tin affects the diffusion rates and/or solubility of Al and Ca. The diffusion rate of Sn in Mg [13] is an order of magnitude lower than that of Al in Mg [14] at 180°C, although the exact rate of diffusion in these complex alloys is not known.

Figure 4.6 is a BF TEM image of an as-cast MRI230D specimen; the original specimen was a die-cast block of nominal dimensions 40x40x10 mm, not one of the cylindrical creep specimens imaged in Section 3.4. The image is from the α-Mg phase and a zone axis of $[11\bar{2}0]$ and $\mathbf{g} = [0002]$ was used. No <a> type dislocations are visible under these conditions. Al_2Ca (C15) precipitates ~40 nm in size, lying parallel to the basal plane, are observed in the primary α-Mg. These precipitates were not observed in every foil prepared from the specimen, indicating that the precipitates had just started to appear during the casting process. Not every feature with dark contrast in this image is a C15 precipitate, however. These additional features have not been positively identified, but the more spherical particles with dark gray contrast may be CaMgSn, while the larger features with black contrast could potentially be oxides from the foil preparation process. No extra spots corresponding to these phases could be distinguished in the diffraction patterns, however.

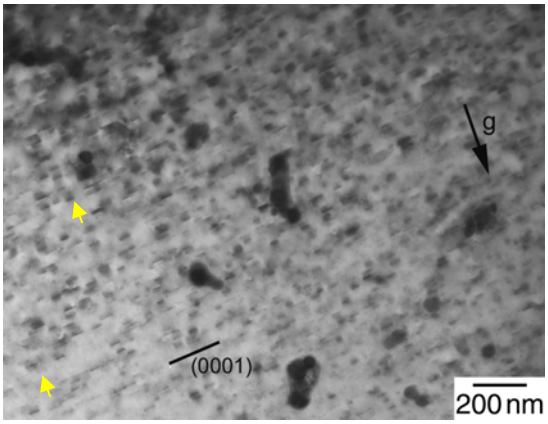

Figure 4.6 - As-cast MRI230D with Al_2Ca precipitates present in the α-Mg cells. B= $[11\bar{2}0]$ and g= (0002). Several precipitates are indicated by the yellow arrows.

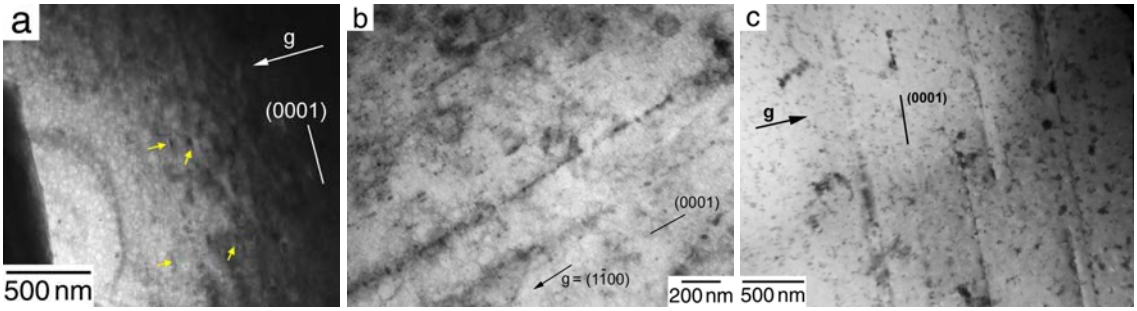

Figure 4.7 - BF TEM images of MRI230D aged at 250C for a) 1h, b) 100 h and c) 500 h. The yellow arrows indicate precipitates in a). B= $[11\bar{2}0]$ and g= (0002) for a) and c).

The microstructure for samples aged at 250°C at various times was also characterized by TEM, Figure 4.7. All images were made using a zone axis of $[11\bar{2}0]$, although the **g** vector used varied. The precipitates observed in the as-cast state are still present, although they have grown in size compared with the as-cast condition. The precipitates are still aligned with the basal trace, much like in the as-cast state. As the aging time increases, the precipitates continue to grow in size. Although it is not known if the volume fraction of precipitates remains constant after 500 hours, coarsening of the precipitates may have occurred for this specimen. For samples aged at 250°C, peak hardness was measured at 100 hours of aging, and the hardness decreased for the sample aged 500 hours, an indication of precipitate coarsening.

The microstructures of MRI230D samples aged 100 hours at 175°C and 300°C are shown in Figure 4.8. At both temperatures, precipitates of Al_2Ca are again observed in the primary α-Mg cells, aligned with the basal trace. The precipitates increase in size

as aging the temperature increases. After 100 hours at 175°C, the precipitates are ~70 nm in length. At 300°C, they range in size from ~85-255 nm in length. The precipitates have a disc-shaped morphology, so in cross-section, the length observed will vary depending on how the viewing plane sections the disc. No β-$Mg_{17}Al_{12}$ phase was observed to form in MRI230D with aging.

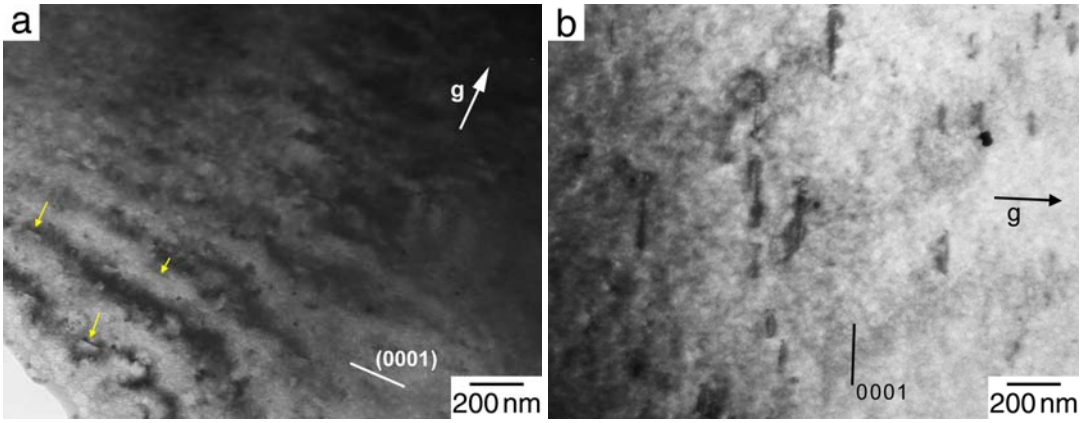

Figure 4.8 - Variation in precipitate size in MRI230D with aging temperature after 100 hours: a) 175°C and b) 300°C. Thickness fringes are visible in a), so precipitates are highlighted with a yellow arrow in this image. B= $[11\bar{2}0]$ **and g=** (0002) **for both images.**

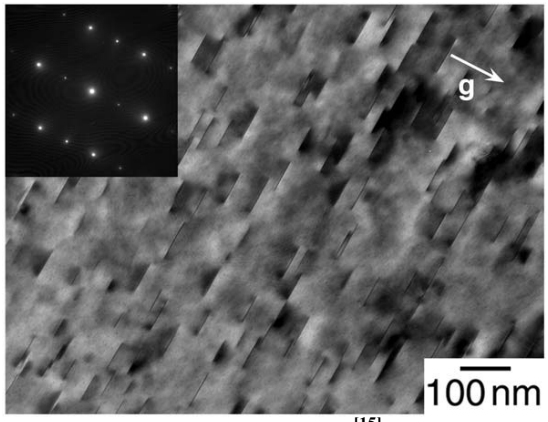

Figure 4.9 - TEM BF image of AXJ530 aged 1 h at 300°C [15].

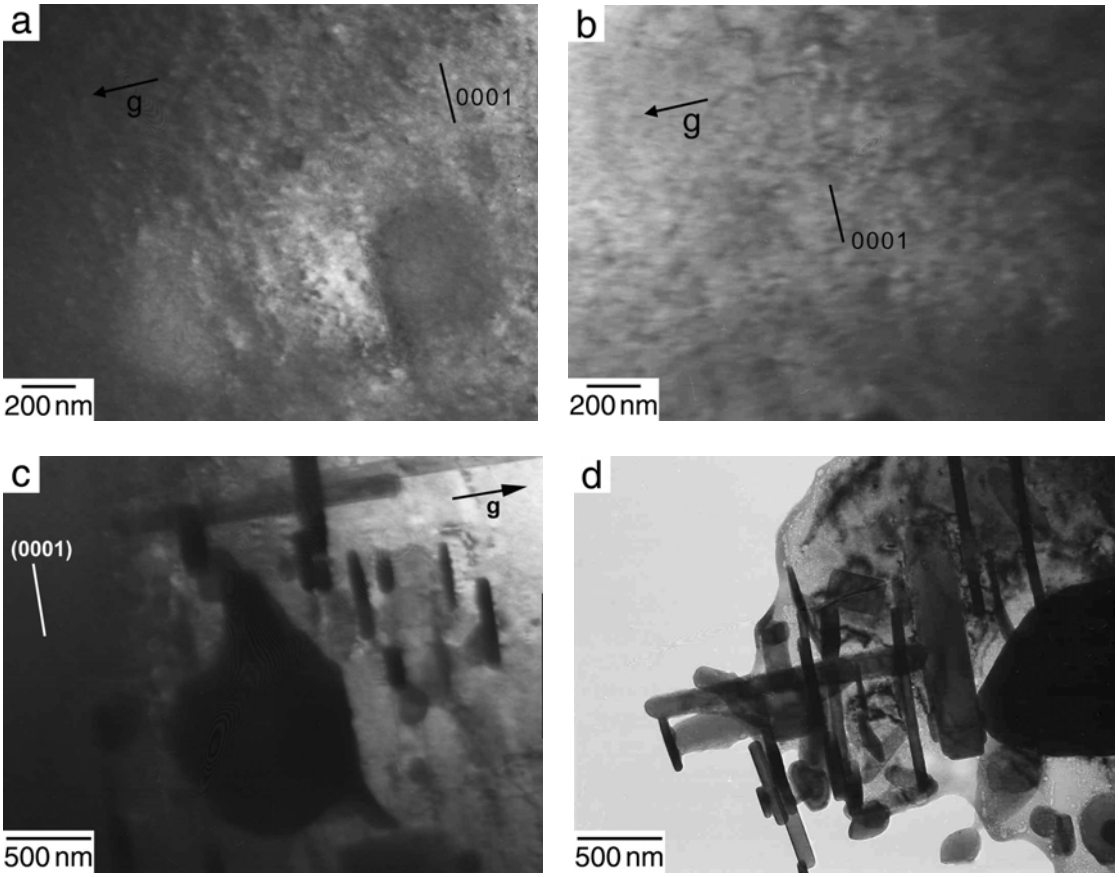

Figure 4.10 - TEM BF images of MRI153M aged for 100 h at 250C: a-b) cell interiors, c) near interdendritic region and d) interdendritic region. B = $[11\bar{2}0]$ and g = (0002) for a-c).

In aged AXJ530, Figure 4.9, precipitates of Al_2Ca form, aligned with the basal trace [11, 15], much like what is observed for MRI230D. For comparison, a sample of MRI153M (which has a higher nominal Al and lower nominal Ca concentration) was also aged for 100 hours at 250°C. The resulting microstructure is shown in Figure 4.10. In the aged MRI153M, no C15 precipitates were observed in the cell interiors, Figure 4.10a-b, although more areas should be examined to verify the actual number density. Instead, blocky precipitates were found to form in the near-interdendritic region, Figure 4.10c-d. These were identified as continuous precipitates of β-$Mg_{17}Al_{12}$, and lie both parallel and perpendicular to the basal direction, similar to Celotto's observations for an aged sample of AZ91 [16], Figure 4.11. The difference in precipitation behavior between MRI153M and MRI230D (and AXJ530) indicates a compositional difference in the primary alpha magnesium in this alloy. Based on the liquidus projection developed by Suzuki et al. [17], aluminum concentration in the primary phase has been estimated as 1.5 wt% for AXJ530,

3.7 wt% for MRI230D and approximately 7.2 wt% for MRI153M. Pandat Scheil calculations predict that the α-Mg phase will have an average Al concentration of 1.77 wt% for AXJ530, 5.54 wt% for MRI230D and 6.61 wt% for MRI153M. Since the concentration of the primary α-Mg phase is expected to differ for each alloy, local composition measurements are required to understand the precipitation behavior observed during aging.

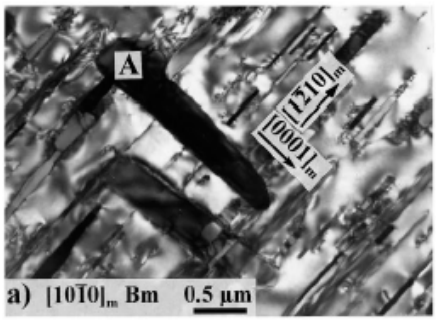

Figure 4.11 - TEM micrograph of aged AZ91 with precipitates of β-$Mg_{17}Al_{12}$ [16].

The precipitation behavior observed during aging correlates well with the aged tensile properties, described in Section 3.2. Aged MRI153M had the lowest tensile strength, and aged AXJ530 had the highest. MRI153M was the only alloy that had significant β-$Mg_{17}Al_{12}$ phase formation during aging (Figure 4.10c). AXJ530 and MRI230D, which formed precipitates of Al_2Ca during aging, also had a larger change in strength from the as-cast to aged state. The equilibrium phase fractions predicted by Pandat for AXJ530, MRI230D and MRI153M are shown in Figure 4.3 as a function of temperature, and the fractions predicted at 250°C are listed in Table 4-2. The τ-AlMgSr phase included in this table is a ternary phase identified by Janz et al. in the Mg-Al-Sr ternary system [6], although it was not included in the liquidus surface calculated by Cao et al. [3]. A higher fraction of C15 is predicted for AXJ530 and MRI230D, while MRI153M has a high fraction of β-$Mg_{17}Al_{12}$. Although some C15 is predicted for MRI153M, the amount is much lower than for the other alloys.

In summary, the as-cast and peak hardness of AXJ530 and MRI230D are almost identical. In both alloys, precipitates of Al_2Ca form and grow in the primary α-Mg phase during high temperature exposure. These precipitates have a disc-shaped morphology and lie parallel to the basal plane of the α-Mg. Only a modest increase in hardness (5-6 Hv) was realized with aging because of the low volume fraction and precipitate

orientation, which will be discussed in more detail in Section 5.4.2. In aged MRI153M, precipitates of β-$Mg_{17}Al_{12}$ were observed in the near-interdendritic region; these precipitates were aligned both parallel and perpendicular to the basal direction of the α-Mg. Beta precipitates were not observed in either AXJ530 or MRI230D. Only limited evidence of Al_2Ca precipitation was observed in aged MRI153M. Therefore, on the basis of the precipitation behavior observed during aging, the Al and Ca concentrations in the α-Mg phase are expected to differ for the alloys. The actual solute concentration was measured using an electron microprobe technique, and is described in more detail in the next section.

Table 4-2 - Pandat predictions of equilibrium phase fractions at 250°C

	Phase Fraction				
Alloy	**α-Mg**	**C15 (Al_2Ca)**	**β-$Mg_{17}Al_{12}$**	**τ-AlMgSr**	**Ca_2Sn**
AXJ530	0.936	0.056	-	0.008	-
MRI230D	0.940	0.037	-	0.018	0.005
MRI153M	0.905	0.013	0.065	0.018	-

4.3 Elemental Partitioning During Solidification

The solute concentrations in the α-Mg phase will differ over the course of solidification, and nominal compositions alone are not an accurate indicator of the solute and precipitation strengthening that can occur during creep. To understand the precipitation behavior that was described in the previous section, the partitioning behavior must be examined. The segregation profiles of the three major elements (Mg, Al and Ca) are shown in Figure 4.12 for remelted samples of MRI230D and MRI153M and permanent mold cast AXJ530 and AX44 from Saddock [7]. The casting procedures for these samples are described in more detail in Section 2.1. AX44 is included as a baseline for comparison of an Mg-Al-Ca-based alloy containing no major quaternary additions. For each element, two profiles are presented. The first, shown in Figure 4.12(a, c and e) are least-mean squares fits of the experimental data simplified for comparison. The second column, Figure 4.12(b, d and f), shows the as-sorted data. The scatter observed in the as-sorted data is a result of the sorting process used during data analysis. Because the Mg concentration is used for sorting (i.e. a single element sort was utilized, as described in Section 1.6), errors in the Mg concentration measurements lead to scatter in both the Al and Ca profiles as shown. If the Al concentration were used for

sorting, the Al profile would be smooth and scatter would be observed in both the Mg and Ca profiles. However, as explained in Section 2.4, α-Mg is the primary phase and therefore decreasing Mg concentration is the appropriate sorting criterion.

The Al segregation profiles, shown in Figure 4.12c, are especially of interest, since Al can contribute to both solute and precipitation strengthening in Mg alloys [1, 11, 18]. However, it is not possible to distinguish between the two forms of strengthening with microprobe compositional measurements alone since the electron beam will sample both the matrix and any nanometer-scale precipitates present. The Al concentrations at three points during solidification are also plotted in Figure 4.13 for all four alloys. In Figure 4.12c, AX44 and AXJ530 have similar levels of Al in the primary α-Mg, while MRI230D and MRI153M both have higher levels of Al. Part of this difference may result from the higher bulk concentration of Al in the two MRI alloys, 6.5-8 wt% as compared with the 4-5 wt% in AX44 and AXJ530, respectively. However, it is also interesting to note that for the MRI230D, the shape of the Al segregation profile differs from the Al segregation profiles of the other three alloys. The profile was more linear for MRI230D, which suggests increased partitioning in this alloy. This will be discussed in more detail later in this section.

The exact shape of the Al concentration profile for MRI230D was somewhat sensitive to the step size used for data collection. For most scans, a step size of 10 μm between points was used. However, for some scans it was found that this sampled mainly the near-eutectic region, causing the curve to be skewed toward higher Al values at lower fraction solid. The average cell size for this alloy was approximately 20 μm, so if the first point sampled was in the near-eutectic region, then every other point would likely fall in this same region if a step size of 10 μm was used. To confirm that the data for MRI230D was accurate, scans with smaller step sizes were run, and the resulting profiles were plotted together for comparison, Figure 4.14. When the degree of segregation (i.e. the measured concentrations and shape of the segregation curve) did not vary with step size it was assumed that the degree of segregation was accurately captured with this technique. The MRI230D data that are presented in Figures 4.12 and 4.13 for both Al and Ca are thus a combination of scans of step sizes ranging from 3-10 μm, but

accurately reflect the elemental partitioning that occurs in this alloy given the large number of areas sampled.

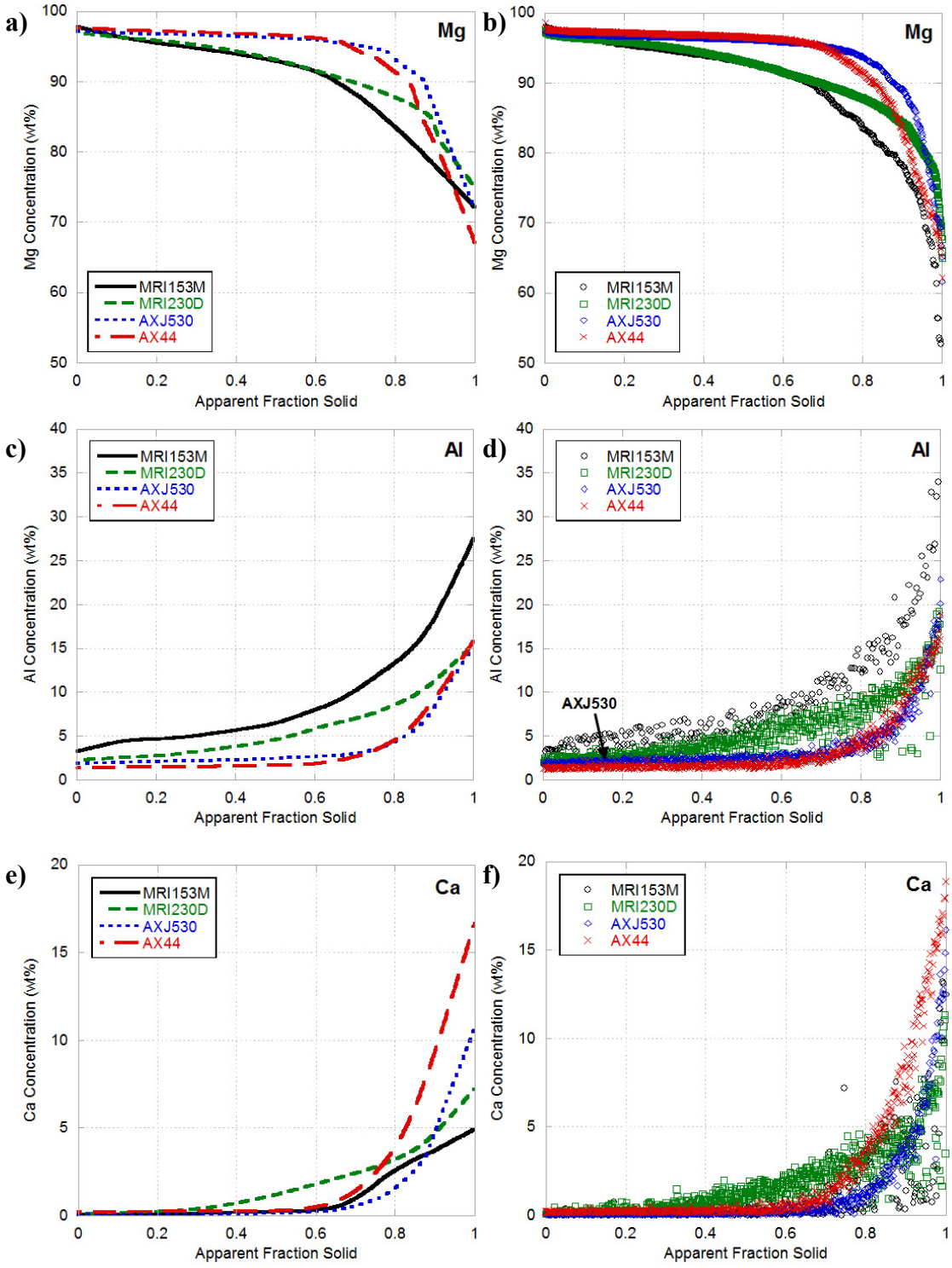

Figure 4.12 - Elemental partitioning curves: a-b) Mg, c-d) Al, and e-f) Ca. a,c,e) Least-mean-squares fit for the data. b,d,f) Sorted data illustrating the scatter that results from the sorting method. AXJ530 and AX44 data from Saddock [7].

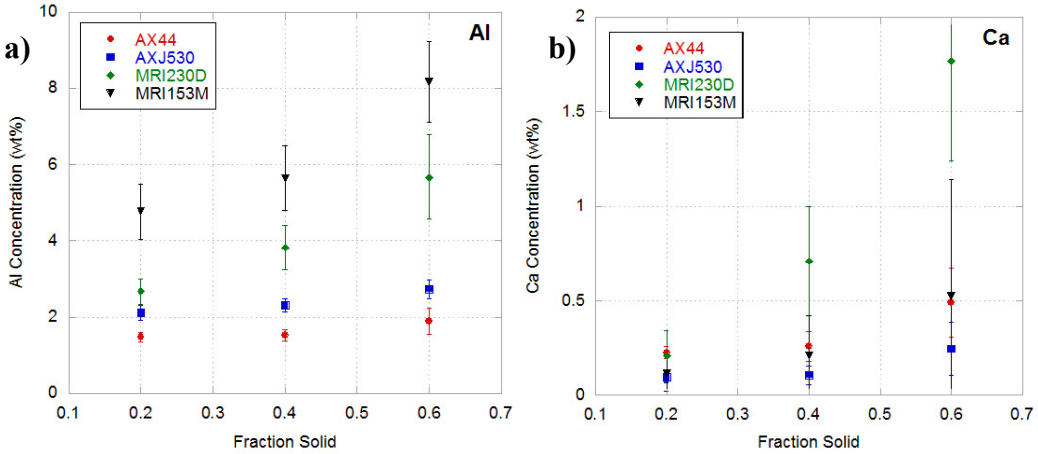

Figure 4.13 - Comparison of a) Al and b) Ca concentration at various fractions solid for the Mg-Al-Ca-based alloys.

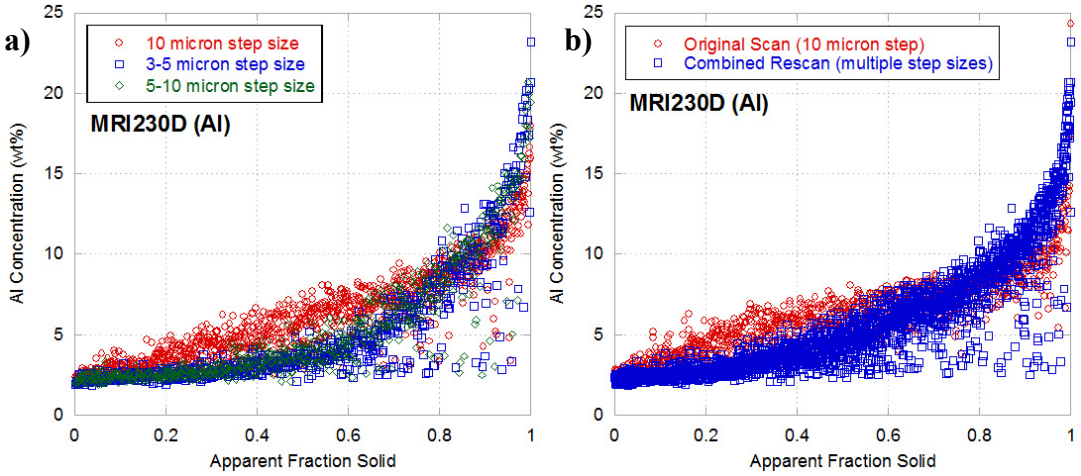

Figure 4.14 - a) Comparison of microprobe scans of various step sizes. b) Combined rescan data (blue) plotted against the original data for MRI230D.

The Ca segregation profiles are shown in Figure 4.12e, and the Ca concentration at three points during solidification is again examined, Figure 4.13. Ca has a lower solubility than Al in Mg but its larger atomic misfit will still give rise to solute strengthening during creep [19, 20], which will be discussed further in Section 4.4. Ca also contributes to precipitation strengthening; for example, precipitates of Al_2Ca were found to form in aged samples of AXJ530 [11] and MRI230D as described earlier. In Figure 4.12e, the Ca profiles of MRI153M, AX44 and AXJ530 are fairly similar. Significantly, more Ca was present in the primary α-Mg of the MRI230D. This is in spite of the fact that MRI230D has a lower bulk Ca concentration than either AX44 or AXJ530. As

observed for Al, the Ca segregation profile for MRI230D is more linear than that of the other three alloys, suggesting increased Ca partitioning to the α-Mg phase.

The segregation profiles included in Figure 4.12 are from alloys solidified with a slower cooling rate. However, in the automotive industry, alloys are most commonly die cast with higher cooling rates than in the current investigation. To confirm that the profiles measured are representative of die-cast alloys as well, electron microprobe measurements of composition were also completed for die-cast MRI230D and MRI153M. Line scans across several cells with step sizes of ~3-5 μm between points were conducted for these samples, and the same data analysis routine (as described in Section 2.4) was followed. The resulting segregation profiles are shown in Figure 4.15. In the near-eutectic region, most of the data was outside the acceptable range (99-101 total wt%) because of concurrent sampling of multiple phases, so the measured data is less accurate at higher fractions solid. For lower fractions solid (less than 0.5) the die-cast Al and Ca segregation profiles are essentially identical to the recast profiles for both MRI153M and MRI230D. Thus, the partitioning profiles included in Figure 4.12 are also representative of the grain interiors of die-cast specimens of these same alloys. Greater differences may exist in the near-interdendritic region, however, since lower Al and Ca concentrations were measured in this region for the die-cast samples of the MRI alloys. Given the relative ease of data collection in samples with larger average cell sizes, partitioning curves from the more slowly cooled samples will be used for subsequent analysis in both this chapter and in Chapter 5. The microprobe technique used in this study is likely not the ideal technique for materials with smaller microstructural features (e.g. die-cast alloys).

To determine whether the Al and Ca partitioning to the α-Mg actually increased in MRI230D, as suggested by the shape of the segregation profiles, further quantification was necessary. This was accomplished with a Scheil analysis to determine the partitioning coefficients for Al and Ca. A Scheil equation was fit to the experimental data from the microprobe, and is shown in Fig. 4.16 for the Mg, Al and Ca concentrations of the induction melted MRI230D. The partitioning coefficients determined from the fit of the segregation data for the major elements of MRI230D and the other alloys are also summarized in Table 4-3. For the induction melted MRI153M, the calculated Al

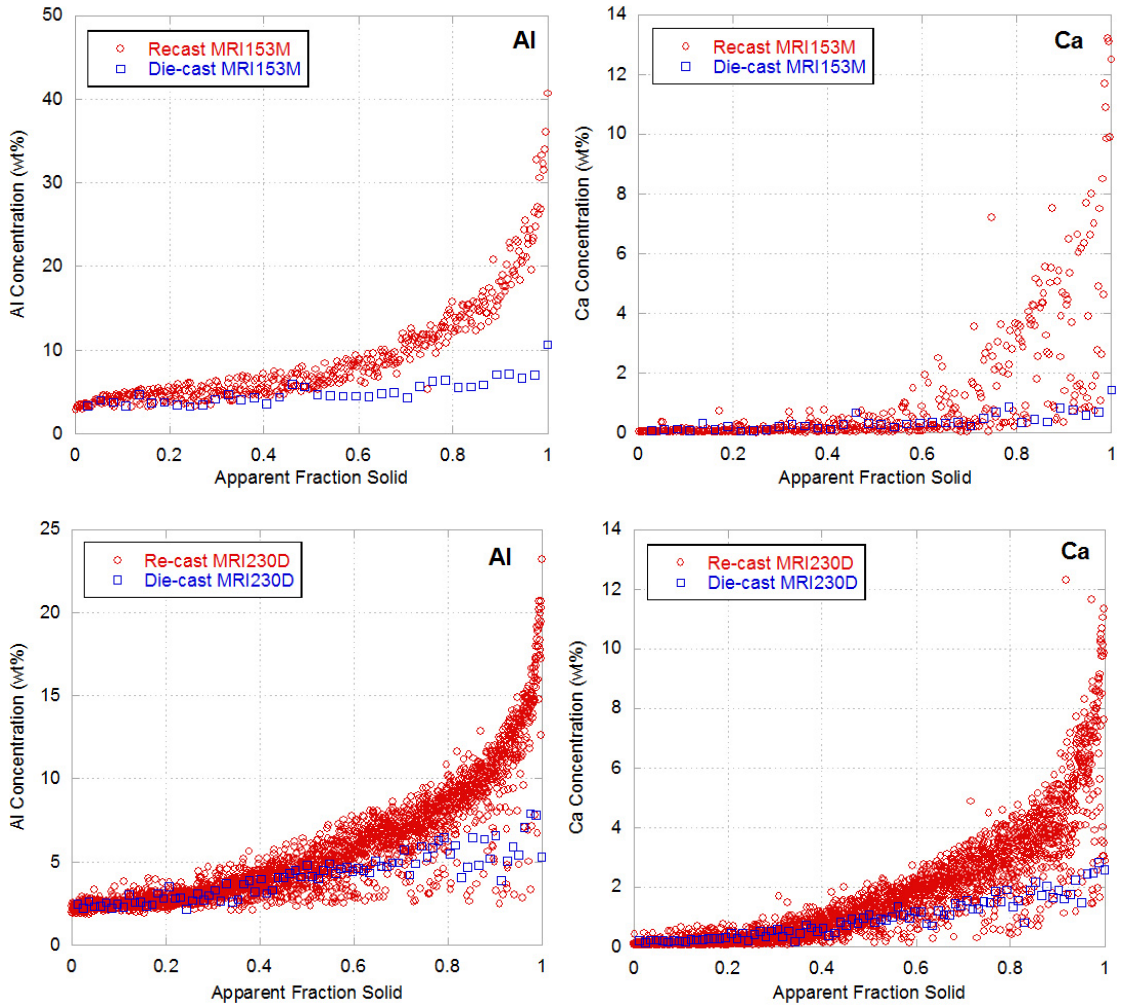

Figure 4.15 - Microsegregation comparison of a slowly cooled re-cast specimen (red) and more quickly cooled die-cast specimen (blue) of a-b) MRI153M and c-d) MRI230D.

partitioning coefficient is higher and the Ca partitioning coefficient is approximately the same as that of AX44 and AXJ530. This is expected, based on the shape of the segregation profile for MRI153M. Two sets of values are included for MRI230D for the Scheil fit. The first are average coefficients that were determined using the first 10% to solidify, and the fit is not as good at high fraction solid, Figure 4.16. Based on the overall shape of the segregation curve for MRI230D compared with AX44 and AXJ530, one would expect the *k* values for both Al and Ca to be significantly different for MRI230D. In particular, the Ca partitioning coefficient is expected to be highest for MRI230D given the segregation profile. The *k* values are an indication of how strongly an element segregates to either the interdendritic region or cell interior. Since Ca usually segregates preferentially to the interdendritic region, higher values of *k* would indicate that more is

segregating to the α-Mg phase. However, the partitioning coefficients calculated with this first method are actually very similar, suggesting that for the first solid to form, segregation is fairly similar for these alloys. If the later stages of solidification are considered, from 10%-60% solidified, partitioning to the α-Mg is much stronger in MRI230D. However, higher *k* values that reflect this stronger partitioning do not capture the shape of the entire segregation profile in Figure 4.16.

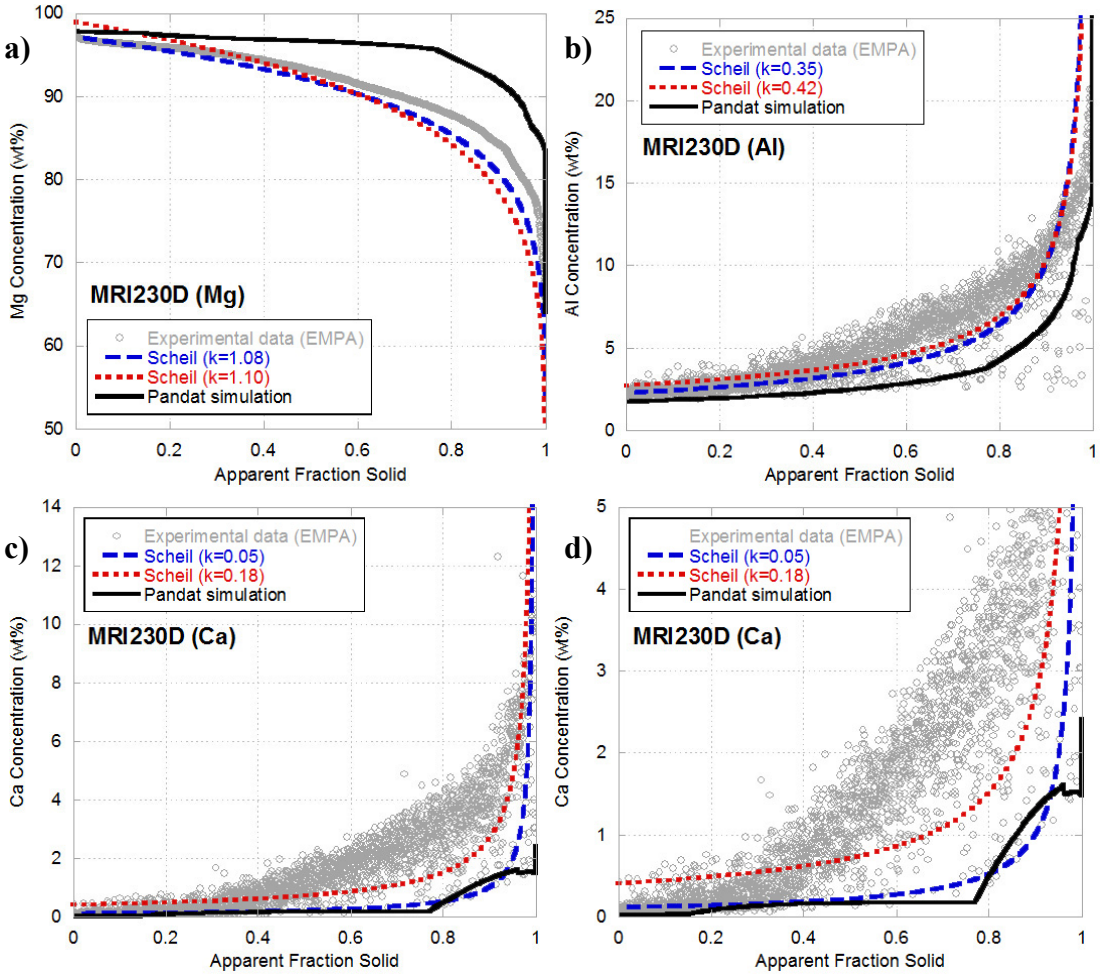

Figure 4.16 - Comparison of fitted Scheil and Pandat simulations to experimental partitioning data. a) Mg, b) Al, c) Ca and d) close-up of lower concentrations for Ca.

Table 4-3 – Calculated Scheil partitioning coefficients

Alloy	k_{Mg}	k_{Al}	k_{Ca}
AX44 [7]	1.05	0.32	0.05
AXJ530 [7]	1.03	0.38	0.06
MRI230D (0-10%)	1.08	0.35	0.05
MRI230D (0-60%)	1.10	0.42	0.18
MRI153M	1.07	0.50	0.06

For MRI230D, neither Scheil curve determined from the fit of the experimental data accurately reflects the entire solidification range; both underestimate the Al and Ca concentration at high fraction solid. Scheil segregation curves calculated using the Pandat™ thermodynamic database are also shown in Figure 4.16. The Pandat curves, while fairly similar to the experimental data for the first part of solidification, also underestimate the amount of Al and Ca for larger fraction solid. Curvature in the phase field boundaries can lead to non-linear variation in both C_s and C_L and thus changes in the partitioning coefficient. Back diffusion in the solid can also change the shape of the segregation profile, and the Scheil equation does not account for this.

To account for the presence of back diffusion in the solid, a modified Scheil equation (Equations 1.7-1.8) was fit to the Al data, Figure 4.17. Only Al is considered at this time due to the lack of diffusion data for Ca in Mg. Back diffusion is incorporated into the Scheil equation through the Fourier coefficient (α), which in turn depends on the diffusivity (D), solidification time (t), and length scale of solidification (L). For this analysis, the solidification time has been estimated as 100 s and the length scale approximated as 200 μm [7]. The Al diffusivity was calculated from data from Moreau [14] for temperatures of 400, 500, 600 and 700°C. These values were then averaged to yield an approximate diffusivity during solidification of 1.7×10^{-8} cm^2/s, which corresponds to a Fourier coefficient of 0.0043. However, when this is plotted against the unmodified Scheil equation that does not take back diffusion into account (with $k = 0.42$), the curves are essentially identical. Thus, back diffusion is not expected to have much impact on the partitioning curves for this alloy. Only when the diffusivity is increased by two orders of magnitude (to 1.7×10^{-8} cm^2/s, or an α of 0.43) is there a significant change in the shape of the curve. Even in this instance, however, there is not a good correlation

between the calculated modified Scheil curve and the experimentally measured data. Instead, the differences between the Scheil (both fitted and thermodynamically calculated) and the experimentally measured partitioning curves in Figure 4.16 is most likely due to curvature in the phase field boundaries, since this violates the assumption of the Scheil analysis that the phase boundaries are linear.

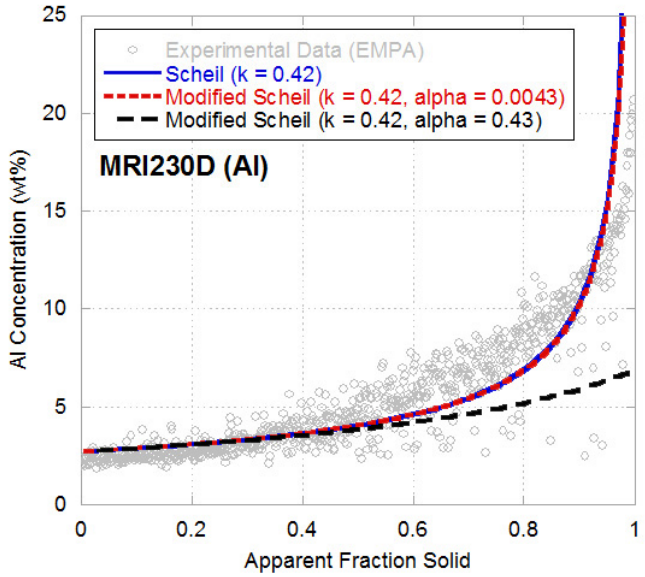

Figure 4.17 - Comparison of experimentally measured Al segregation profile of MRI230D with Scheil profiles that have been modified to account for back diffusion in the solid.

The presence of Sn in MRI230D may account for the difference in partitioning during solidification that is observed in this alloy, and this will be examined in more detail in Chapter 5. Sn is likely to affect the diffusion and solubility of the other alloying elements, increasing the amount of Al and Ca that remain in the primary phase. At this time, the lack of diffusion data for these complex systems makes it difficult to draw a definitive conclusion. However, as described in Section 4.1, slower aging kinetics were observed for MRI230D compared with AXJ530, indicating that Sn can affect interdiffusion in this alloy. The presence of Sn may also change the solidification path of the alloy as illustrated in Figure 4.18, where the calculated solidification paths for AX44 and Mg-6.5Al-2.25Ca (the ternary composition of MRI230D) are shown; with the addition of Sn to the MRI230D base composition, the solidification path may be modified to more closely resemble the dashed line.

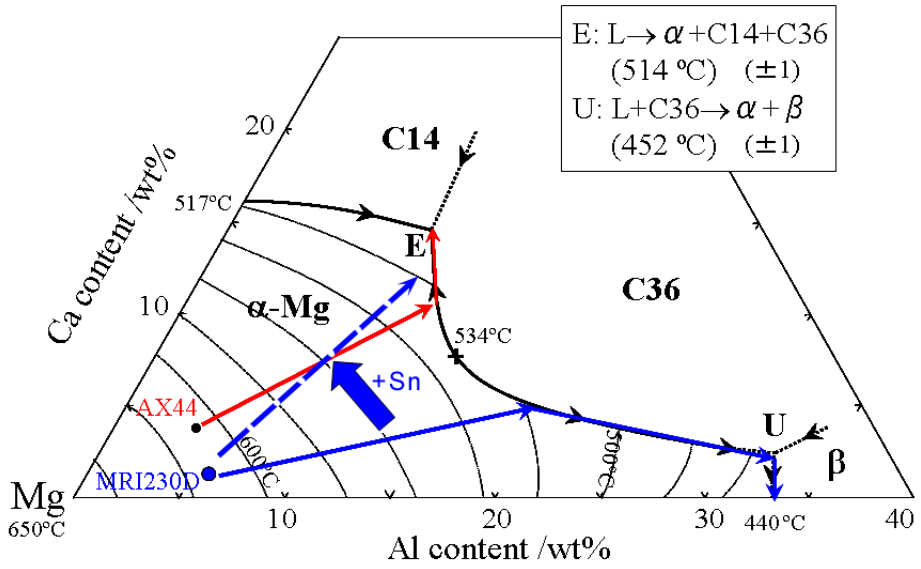

Figure 4.18 - Illustration of the possible change in solidification path with the addition of Sn to Mg-6.5Al-2.25Ca. Modified from Suzuki et al. [17]

Isolating the effect of Sn in these alloys is complicated by the different bulk Al and Ca concentrations for each alloy. Too many variables exist to conclusively attribute the increased Al and Ca segregation to the α-Mg phase in MRI230D to the presence of Sn. It is interesting to note, however, that AX44, AXJ530 and MRI153M, which do not contain Sn, have very similar concentration profiles, with the increased Al in the primary phase of the MRI153M most likely due to the higher bulk Al concentration in this alloy. A more systematic study of Sn additions has therefore been conducted and will be described in the next chapter, where the partitioning in quaternary Mg-Al-Ca-Sn alloys with systematic variations in (nominal) Mg, Al, Ca and Sn concentration is examined.

4.4 Implications of Partitioning Behavior on Creep Resistance

In Chapter 3, the minimum creep rate for MRI153M was observed to be 1-2 orders of magnitude higher than that of AXJ530 and MRI230D under the same creep conditions. Viscous glide of dislocations was identified as the operative creep mechanism, for which the creep rate can be assumed to depend strongly on dislocation motion in the primary α-Mg phase. Variation in Al and Ca partitioning to the primary α-Mg in AXJ530, MRI230D and MRI153M offers a reasonable explanation for differences in creep behavior observed in these alloys, since increased solute can lead to increased solute strengthening during creep. Saddock has calculated that the influence of solute

alone can account for differences in creep rate of up to three orders of magnitude [7]. In a recent study by Zhu et al. [21], the creep resistance of die-cast Mg-4Al-2RE was reported to be related to the amount of Al solute in the primary α-Mg after casting. For creep controlled by viscous glide, Mohamed and Langdon [19] proposed the following model relating creep rate, $\dot{\varepsilon}$, to solute concentration:

$$\dot{\varepsilon} \approx \frac{\pi(1-\nu)kT\tilde{D}}{6e^2cb^5G}\left(\frac{\sigma}{G}\right)^3, \tag{4.1}$$

where ν is Poisson's ratio, σ is the applied stress, k is Boltzmann's constant, T is the absolute temperature, $\tilde{D}$ is the interdiffusion coefficient for the solute, G is the shear modulus, b is the Burgers vector, e is the solute-solvent size difference and c is the concentration of solute. When comparing the alloys studied, the dependence of the material parameters in Eqn. (4.1) on small changes in composition is negligible with the exception of e, c and $\tilde{D}$. These terms can thus be evaluated to estimate the influence of solute concentration on creep, and the alloy with the largest $e^2c/\tilde{D}$ is expected to have the lowest creep rate. However, because the interdiffusion coefficients are not known for most elements in this complex alloy system, only e^2c will be considered at this time. The diffusivity of Al and Ca may be greatly different, however, so the contribution from the elements will not have equal weight. The diffusivity will also differ from alloy to alloy, allowing only rough approximation to be made. Based on the delay of overaging in MRI230D, this alloy may have very different Al and Ca diffusivity than AXJ530 or MRI153M, which do not contain Sn.

The values of e^2c for Al and Ca are included in Table 4-4 for the four alloys studied. The atomic misfit (e) of Al in Mg is -12.4% (0.124) and 20.4% (0.204) for Ca in Mg [22]. The solute concentrations used for this calculation are approximations taken from the near boundary region of the microstructure, which corresponds to a fraction solid of ~ 0.7. Al and Ca concentrations in the α-Mg will be near maximum in this region based on the shape of the segregation curves, and Pandat simulations predict that eutectic phases will start to form at a fraction solid of just over 0.75. Based on the solute contributions in Table 4-4, one would expect MRI153M to have a low creep rate;

however, this fails to take into account any precipitation that occurs at creep temperatures.

Table 4-4 - Contribution of solute concentration (in atomic fraction) to creep strengthening

Alloy	Al		Ca	
	c_{max}	e^2c ($\times 10^{-4}$)	c_{max}	e^2c ($\times 10^{-4}$)
AX44	0.023	3.51	0.007	2.83
AXJ530	0.028	4.24	0.003	1.17
MRI230D	0.061	9.35	0.015	6.41
MRI153M	0.100	15.4	0.006	2.29

Suzuki et al. have suggested that by increasing the solid-solubility of Ca in the α-Mg matrix of Mg-Al-Ca-based alloys at elevated temperatures, the volume fraction of precipitates present can be increased to improve the precipitation strengthening of the alloy [11]. MRI230D has high levels of both Al and Ca, and during exposure to high temperatures precipitates of Al_2Ca can form in the cell interiors, as observed in the aging study in Section 4.2. For MRI153M, however, while the level of Al in the primary phase is as high as in MRI230D, the Ca concentration is much lower. Thus, a lower volume fraction of Al_2Ca precipitates can form in the cell interiors. In the near-boundary region, the Al concentration of MRI153M exceeds the equilibrium amount of Al that can be dissolved in Mg, about 12.9 wt% according to the binary Mg-Al phase diagram [12]. Thus, precipitates of β-$Mg_{17}Al_{12}$ can form in this region, which is again supported by the aging study described earlier. Beta precipitates have been reported to coarsen rapidly at creep temperatures, resulting in lower creep resistance [21]. Although automotive alloys are mostly used in the as-cast condition, they are still subjected to long-term thermal exposure during use, and it is important to consider the precipitates that may form. Alloys such as AXJ530 and MRI230D that retain sufficient Al in the primary phase to avoid the formation of β-$Mg_{17}Al_{12}$ during high temperature exposure and which also have sufficient Ca available for precipitate formation offer a viable approach to improving creep resistance in Mg-Al-based alloys.

4.5 Summary

The segregation of Al and Ca has been examined for three Mg-Al-Ca-based alloys. Al and Ca were determined from EDS maps to preferentially segregate to the interdendritic region in remelted MRI230D. An enrichment of Al and Ca was observed in the near-interdendritic region of the microstructure, and lower concentrations were measured in the cell interiors. However, this level of solute was sufficient for precipitation to occur during aging. In MRI230D and AXJ530, precipitates of Al_2Ca formed during high temperature exposure; these precipitates were oriented parallel to the basal plane of the α-Mg phase and had a disc-shaped morphology. In MRI230D, peak hardness occurred after aging 100 hours at 250°C, while peak hardness occurred after only 1 hour of aging at 250°C for AXJ530. The delayed onset of overaging in MRI230D offers evidence that Sn can slow the kinetics of precipitate coarsening either through decreased diffusivity or the increased solute concentration. However, only modest increases in hardness (~9%) were observed in both AXJ530 and MRI230D. MRI153M, which has a higher nominal Al and lower nominal Ca concentration than AXJ530 and MRI230D, also had precipitates of β-$Mg_{17}Al_{12}$ form in the near-interdendritic region during aging. The precipitation behavior suggests that MRI153M had lower Ca and higher Al concentrations in the primary α-Mg phase.

To measure the actual Al and Ca concentrations in the α-Mg, and quantify the elemental partitioning that occurs during solidification, an electron microprobe technique was employed. MRI153M had higher levels of Al in the primary α-Mg phase than AXJ530 or MRI230D, which was attributed to the higher nominal Al composition, but had similar Al partitioning behavior to AXJ530. Similarly, the Ca concentration was lower in MRI153M due to lower bulk Ca concentration, but the partitioning behavior was again similar to AXJ530. However, MRI230D, which unlike the other alloys contains Sn, had increased Al and Ca partitioning to the α-Mg phase. The increase in Al and Ca partitioning due to Sn additions will be examined in more detail in the next chapter for Mg-Al-Ca-Sn alloys of simplified compositions, i.e. with systematic variation of the Mg, Al, Ca and Sn concentrations. The differences in minimum creep rate that were observed in Chapter 3 for MRI153M, MRI230D and AXJ530 are attributed to the differences in Al

and Ca partitioning that were measured, which can be related to increased solute and precipitation strengthening in MRI230D and AXJ530 as compared with MRI153M.

References

[1] A. Suzuki, N. D. Saddock, L. Riester, E. Lara-Curzio, J. W. Jones, T. M. Pollock, *Metallurgical and Materials Transactions A* **2007**, *38A*, 420.

[2] A. Janz, J. Grobner, R. Schmid-Fetzer, *Journal of Phase Equilibria and Diffusion* **2009**, *30*, 157.

[3] H. Cao, J. Zhu, C. Zhang, K. Wu, N. D. Saddock, J. W. Jones, T. M. Pollock, R. Schmid-Fetzer, Y. A. Chang, *Int. J. Mat. Res.* **2006**, *97*, 422.

[4] A. Kozlov, M. Ohno, T. Abu Leil, N. Hort, K. U. Kainer, R. Schmid-Fetzer, *Intermetallics* **2008**, *16*, 316.

[5] A. Kozlov, M. Ohno, R. Arroyave, Z. K. Liu, R. Schmid-Fetzer, *Intermetallics* **2008**, *16*, 299.

[6] A. Janz, J. Grobner, D. Mirkovic, M. Medraj, J. Zhu, Y. A. Chang, R. Schmid-Fetzer, *Intermetallics* **2007**, *15*, 506.

[7] N. D. Saddock, Ph.D. thesis, University of Michigan (Ann Arbor, MI), **2007**.

[8] N. D. Saddock, A. Suzuki, J. R. TerBush, J. W. Jones, T. M. Pollock, J. E. Zindel, J. E. Allison, *SAE Technical Paper 2007-01-1027*, SAE International, Detroit, MI, **2007**.

[9] A. Suzuki, N. D. Saddock, J. R. TerBush, B. R. Powell, J. W. Jones, T. M. Pollock, in *Magnesium Technology 2007* (Eds.: R. S. Beals, A. A. Luo, N. R. Neelameggham, M. O. Pekguleryuz), TMS, Orlando, FL, **2007**, pp. 375.

[10] B. Bronfin, E. Aghion, F. Von Buch, S. Schumann, M. Katzir, Dead Sea Magnesium Ltd and Volkswagen AG, US Patent 7,041,179 B2, **2006**.

[11] A. Suzuki, N. D. Saddock, J. R. TerBush, B. R. Powell, J. W. Jones, T. M. Pollock, *Metallurgical and Materials Transactions A* **2008**, *39A*, 696.

[12] *ASM Handbook, Vol. 3 - Alloy Phase Diagrams*, ASM International, **1992**.

[13] S. Cohen, G. Goren-Muginstein, S. Avraham, B. Rashkova, G. Dehm, M. Bamberger, *Z. Metallkd.* **2005**, *96*, 1081.

[14] G. Moreau, J. A. Cornet, D. Calais, *Journal of Nuclear Materials* **1971**, *38*, 197.

[15] A. Suzuki, N. D. Saddock, J. R. TerBush, B. R. Powell, J. W. Jones, T. M. Pollock, *SAE Technical Paper 2007-01-1025*, SAE International, Detroit, MI, **2007**.

[16] S. Celotto, *Acta Materialia* **2000**, *48*, 1775.

[17] A. Suzuki, N. D. Saddock, J. W. Jones, T. M. Pollock, *Acta Materialia* **2005**, *53*, 2823.

[18] M. S. Dargusch, K. Pettersen, K. Nogita, M. D. Nave, G. L. Dunlop, *Mat Trans* **2006**, *47*, 977.

[19] F. A. Mohamed, T. G. Langdon, *Acta Metall.* **1974**, *22*, 779.

[20] K. Maruyama, M. Suzuki, H. Sato, *Metallurgical and Materials Transactions* **2002**, *33A*, 875.

[21] S. M. Zhu, M. A. Gibson, J. F. Nie, M. A. Easton, T. B. Abbott, *Scripta Materialia* **2008**, *58*, 477.

[22] T. Uesugi, M. Kohyama, K. Higashi, *Materials Science Forum* **2003**, *426-432*, 599.

Chapter 5

Effect of Tin Additions on Elemental Partitioning and Creep Deformation of Mg-Al-Ca-based Alloys

In Chapter 4 it was shown that Al and Ca partitioned to the primary α-Mg phase during solidification in MRI230D to a greater extent than that observed in AXJ530, AX44 and MRI153M. This was attributed to the presence of Sn in MRI230D, although differences in nominal Al and Ca concentrations between these alloys made isolating the effect of Sn difficult. To address this issue, model alloys with simplified compositions (i.e. with systematic variations in nominal Mg, Al, Ca and Sn concentrations) were cast to explore the effect of Sn additions on partitioning and microstructure development. Three series of alloys were prepared: Mg-5Al-3Ca-xSn (based on the ternary Mg-Al-Ca base composition of AXJ530), Mg-xAl-3Ca-0.5Sn and Mg-xAl-yCa-0.8Sn, where x and y are based on the ternary Mg-Al-Ca compositions of MRI230D and MRI153M.

The microstructures of the cast alloys are presented in Section 5.1, and phase fractions will be compared with predictions made using the Pandat™ thermodynamic database. The elemental partitioning of the quaternary alloys was studied using the electron microprobe technique described previously. The effect of Sn additions on microsegregation will be described in Section 5.2. Compressive creep results will be presented in Section 5.3 for three quaternary alloys (Mg-5Al-3Ca-0.75Sn, Mg-5Al-3Ca-1.5Sn and Mg-6.5Al-2.25Ca-0.8Sn) and MRI230D for tests conducted at 150 and 180°C at 110 MPa. Creep behavior in these alloys will be discussed in terms of solute and precipitate strengthening. Finally, implications for alloy design based on the results presented in this chapter and in Chapter 4 will be examined.

5.1 Microstructure of Mg-Al-Ca-Sn Alloys

Twenty-five gram samples of Mg-Al-Ca-Sn alloys were prepared in an induction furnace using an Mg-4Al-4Ca master alloy with additions of pure Mg, Al and Sn.

Microstructures for the as-cast Mg-5Al-3Ca-(0.25-3.0)Sn series obtained by SEM are shown in Figure 5.1. The microstructures of the alloys are morphologically similar, consisting of the α-Mg phase (dark gray contrast) surrounded by C36 in the interdendritic region (lighter gray contrast). Also present is a phase appearing as white and similar to that observed in MRI230D, which is likely the $Ca_{2-x}Mg_xSn$ phase reported in the literature [1, 2]. The fraction of this Sn-containing phase (hereafter referred to as CaMgSn) increases as the Sn concentration increases, and the phase was heterogeneously distributed for the alloys with higher nominal Sn concentrations, e.g. Figure 5.1f. Average cell sizes for the alloys were similar (~20-30 μm) except for the Mg-5Al-3Ca-1.5Sn alloy, which experienced a slightly slower cooling rate during solidification that led to an increased cell size of 57 μm. The predicted volume fraction of each phase, as determined by Scheil simulations with the Pandat thermodynamic software, is compared with the measured volume fractions in Table 5-1. There is generally good agreement between the predicted and measured volume fractions, although alloys with higher nominal Sn concentrations contain less β-$Mg_{17}Al_{12}$ than predicted. The amount of C36 that forms is relatively constant for alloys with less than 1.5wt% Sn, but is predicted to decrease for the higher Sn containing alloys. The amount of CaMgSn and β-$Mg_{17}Al_{12}$ that forms is also predicted to increase as the nominal Sn concentration increases. Furthermore, the solidification path of the alloy changes when the bulk Sn concentration reaches 1wt% Sn. For alloys with greater than 1wt% Sn, Pandat predicts that the CaMgSn phase will be the first phase to solidify, although the α-Mg phase is still the predominant phase in terms of volume fraction. The CaMgSn phase that solidifies first is carried with the α-Mg as it subsequently solidifies, creating the heterogeneous distribution of CaMgSn that is observed in the higher Sn samples. For the alloy with 3wt% Sn, the increase in concentration of CaMgSn and β-$Mg_{17}Al_{12}$ and the decrease in C36 are related; more CaMgSn initially forms during the early part of the solidification process because of the higher nominal Sn concentration, and its precipitation removes Ca from the liquid. Thus, less Ca is available to form C36 later in the solidification process, and because of the decreased fraction of C36, more Al is available in the liquid to form β-$Mg_{17}Al_{12}$ at the end of the solidification process.

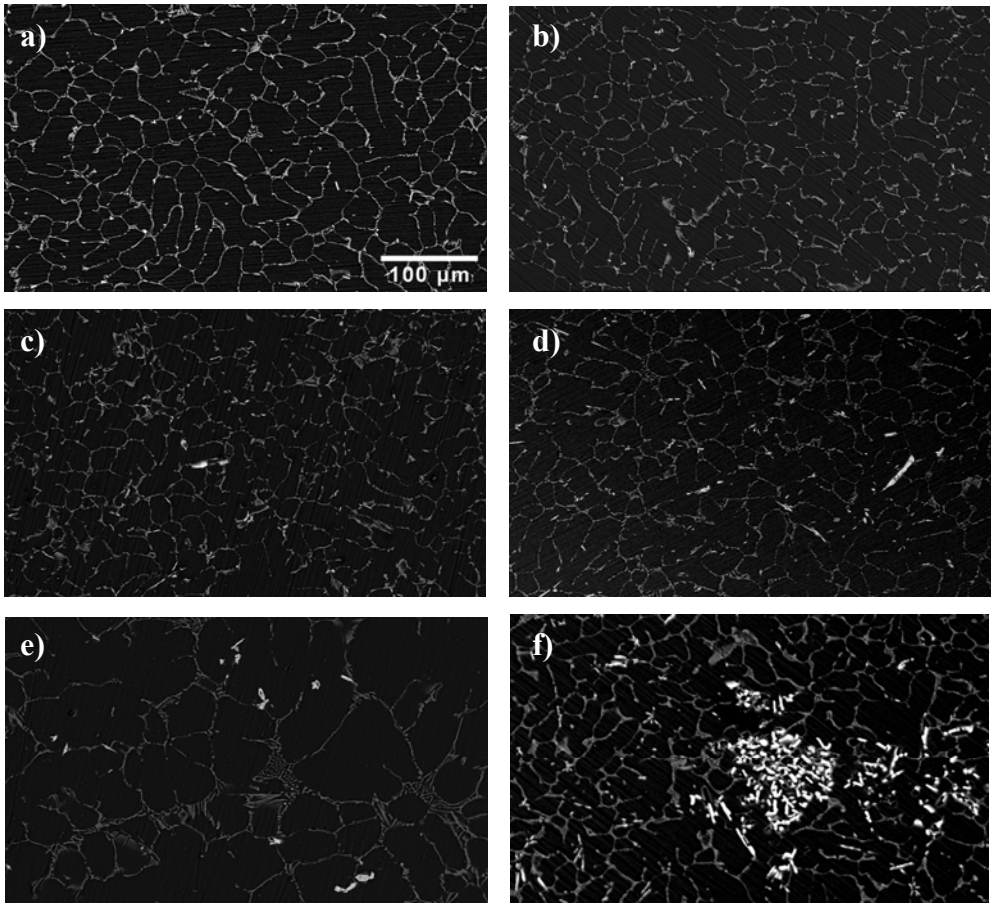

Figure 5.1 - SEM (BSE) micrographs of as-cast Mg-5Al-3Ca-xSn alloys: a) 0.25Sn, b) 0.5Sn, c) 0.75Sn, d) 1Sn, e) 1.5Sn and f) 3Sn. Surfaces were not etched prior to imaging.

Table 5-1 - Percent of each phase in Mg-5Al-3Ca-xSn alloys (non-equilibrium)

	α-Mg		C36		CaMgSn		β-$Mg_{17}Al_{12}$	
Wt% Sn	**Predicted**	**Measured**	**Predicted**	**Measured**	**Predicted**	**Measured**	**Predicted**	**Measured**
0.25	94.3	91.8	5.6	8.0	0.1	0.3	0	0
0.50	94.3	91.8	5.5	8.0	0.3	0.3	0	0
0.75	94.0	90.7	5.5	9.0	0.4	0.4	<0.1	0
1.0	93.8	92.6	5.5	6.3	0.6	0.6	0.1	0
1.5	94.0	94.7	5.2	4.9	0.5	0.4	0.3	0
3.0	92.9	89.2	4.3	8.6	1.9	2.3	0.9	0

The fraction of eutectic for each alloy predicted by Pandat Scheil simulations is included in Table 5-2. The Mg-5Al-3Ca-xSn alloys all have a lower fraction eutectic than AXJ530, but an increased fraction of eutectic compared with MRI230D, with the exception of the Mg-5Al-3Ca-3Sn alloy. Within the quaternary series, the fraction of

eutectic is highest for the 0.25Sn, 0.75Sn and 1Sn alloys, and decreases as the Sn concentration increases above 1wt%, as shown in Figure 5.2.

Table 5-2 - Predicted fraction of eutectic from Pandat Scheil simulation

Alloy Composition (wt%)	Fraction of Eutectic
Mg-5Al-3Ca-0.25Sn	0.245
Mg-5Al-3Ca-0.5Sn	0.240
Mg-5Al-3Ca-0.75Sn	0.244
Mg-5Al-3Ca-1Sn	0.243
Mg-5Al-3Ca-1.5Sn	0.234
Mg-5Al-3Ca-3Sn	0.207
Mg-6.5Al-3Ca-0.5Sn	0.284
Mg-8Al-3Ca-0.5Sn	0.321
Mg-6.5Al-2.25Ca-0.8Sn	0.248
Mg-8Al-1Ca-0.8Sn	0.179
AXJ530 (Mg-5Al-3Ca-0.15Sr)	0.254
MRI230D (Mg-6.5Al-2.25Ca-0.25Sr-0.8Sn)	0.232
MRI153M (Mg-8Al-1Ca-0.27Sr)	0.192

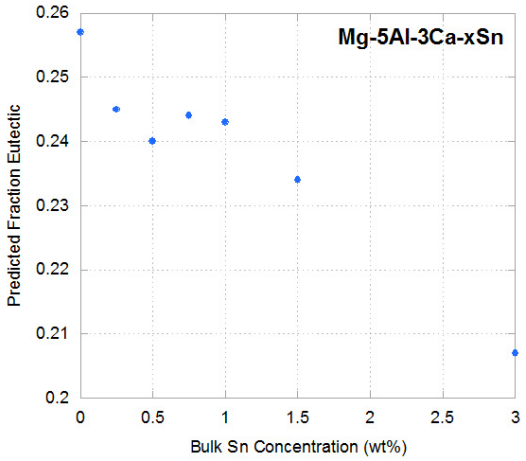

Figure 5.2 - Variation in the fraction eutectic with the bulk Sn concentration in Mg-5Al-3Ca-xSn alloys. The fraction eutectic was determined from Pandat calculations.

Two additional alloys were cast to examine the effect of increased Al concentration at a given Ca and Sn concentration; their compositions were Mg-6.5Al-3Ca-0.5Sn and Mg-8Al-3Ca-0.5Sn. These higher Al alloys have microstructures (Figure

5.3) that are similar morphologically to the microstructure of the Mg-5Al-3Ca-0.5Sn alloy shown in Figure 5.1b. As expected, the volume fraction of β-$Mg_{17}Al_{12}$ (Table 5-3) and the fraction of eutectic (Table 5-2) increases with increasing bulk Al concentration as predicted by the simulations.

Two alloys with similar composition to MRI230D and MRI153M were also cast, Mg-6.5Al-2.25Ca-0.8Sn and Mg-8Al-1Ca-0.8Sn, respectively. These correspond to MRI230D without the 0.25wt% Sr and the ternary Mg-Al-Ca composition of MRI153M with an addition of Sn. Microstructures obtained by SEM are shown in Figure 5.4, and Table 5-3 includes phase fraction predictions from Pandat simulations. MRI230D and Mg-6.5Al-2.25Ca-0.8Sn have similar microstructures, although the quaternary alloy lacks the Sr-containing phases present in MRI230D. The Mg-6.5Al-2.25Ca-0.8Sn quaternary alloy has a higher fraction of eutectic than MRI230D, Table 5-2. However, greater differences in microstructure are observed between MRI153M and Mg-8Al-1Ca-0.8Sn. For the quaternary alloy, less C36 is present and the volume fraction of β-$Mg_{17}Al_{12}$ is increased compared with MRI153M, which is predicted to have 1.4% C36 and 5.8% β-$Mg_{17}Al_{12}$. Addition of 0.8wt% Sn is apparently ineffective in decreasing the volume fraction of β-$Mg_{17}Al_{12}$ in an Mg-8Al-1Ca-based alloy. The fraction of eutectic also decreases with the addition of 0.8wt% Sn, Table 5-2.

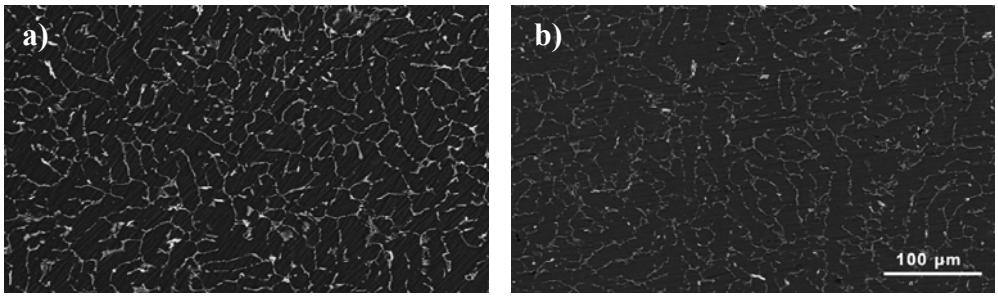

Figure 5.3 - SEM (BSE) micrographs of a) Mg-6.5Al-3Ca-0.5Sn and b) Mg-8Al-3Ca-0.5Sn.

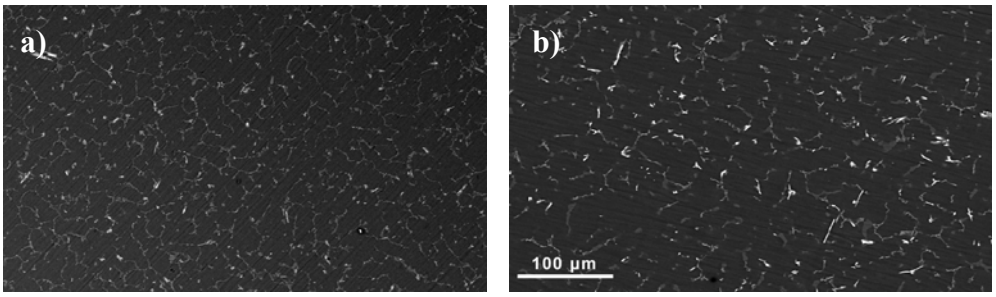

Figure 5.4 - SEM (BSE) micrographs of a) Mg-6.5Al-2.25Ca-0.8Sn and b) Mg-8Al-1Ca-0.8Sn.

Table 5-3 – Pandat predicted percent of each phase (non-equilibrium)

Alloy	α-Mg	C36	CaMgSn	β-$Mg_{17}Al_{12}$
Mg-6.5Al-3Ca-0.5Sn	92.6	5.9	0.3	1.2
Mg-8Al-3Ca-0.5Sn	90.8	6.0	0.3	2.9
Mg-6.5Al-2.25Ca-0.8Sn	93.0	4.0	0.4	2.5
Mg-8Al-1Ca-0.8Sn	90.8	1.0	0.4	7.8

5.2 Elemental Partitioning of Quaternary Mg-Al-Ca-Sn Alloys

Although the microstructures of the quaternary Mg-Al-Ca-Sn alloys were essentially the same, this does not preclude the possibility that microsegregation could still differ greatly among alloys. Therefore, elemental partitioning during solidification in these alloys has been investigated using the electron microprobe technique that was used for the segregation studies presented in Section 4.3.

5.2.1 Mg-5Al-3Ca-xSn Alloys

The Al and Ca partitioning curves for the Mg-5Al-3Ca-(0.25-3.0)Sn alloys are shown in Figures 5.5-5.7 for the as-sorted data, showing the scatter from the sorting method, and the resulting least-mean-squares fits to the raw data. Figure 5.5 includes the curves for the alloys with 0.7Sn or less, where α-Mg is the first phase to solidify, while Figure 5.6 includes the curves for the alloys with 1Sn or higher, where the CaMgSn phase is the first to solidify. Figure 5.7 incorporates the curves for all six alloys into one plot for Al and one for Ca, for ease of comparison. The Al and Ca concentrations at three different fractions solid (f_s = 0.2, 0.4, and 0.6) have also been plotted in Figure 5.8 for more detailed comparison. For these plots, the Al and Ca concentrations have been averaged for $f_s \pm 0.01$, e.g. from 0.19-0.21 for 0.2. A spike in the Al and Ca concentration in the α-Mg phase is observed at higher fractions solid for alloys with 0.75-1wt% Sn, suggesting partitioning may be greater for these alloys. It seems likely that this

higher solute concentration in the near-interdendritic region will affect dislocation motion differently than the lower solute concentration in the grain interiors, although further study is needed to fully characterize the difference.

To quantify the partitioning that occurs in the Mg-5Al-3Ca-xSn alloys, a Scheil equation has been fit to the experimental data for 10-60% solidified, as in Section 4.3. The partitioning coefficients (k) calculated from this analysis are listed in Table 5-4. The alloys with 0.25Sn, 0.75Sn and 3Sn had higher Al partitioning coefficients than the other Mg-5Al-3Ca-xSn alloys, while the 0.25Sn, 0.75Sn and 1Sn alloys had higher Ca partitioning coefficients. The highest Ca partitioning to the α-Mg phase was observed for Mg-5Al-3Ca-0.75Sn, while the lowest was observed for Mg-5Al-3Ca-1.5Sn. The Sn partitioning coefficient is highest for alloys with less than 1wt% Sn, where α-Mg is the first phase to solidify. Less Sn partitions to the α-Mg phase in the alloys where CaMgSn solidifies first, as could be expected.

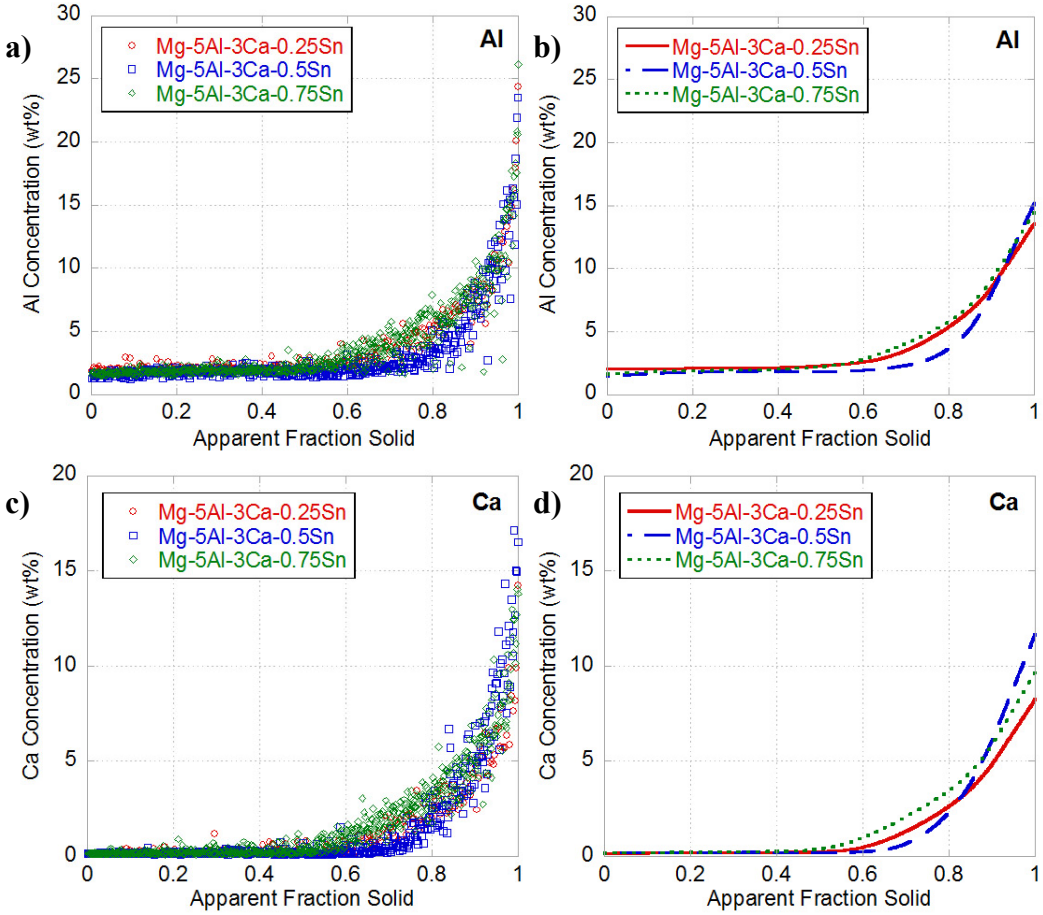

Figure 5.5 - Partitioning curves for alloys with Mg as the first phase to solidify. a) Al - as sorted, b) Al - LMS fit, c) Ca - as sorted and d) Ca- LMS fit.

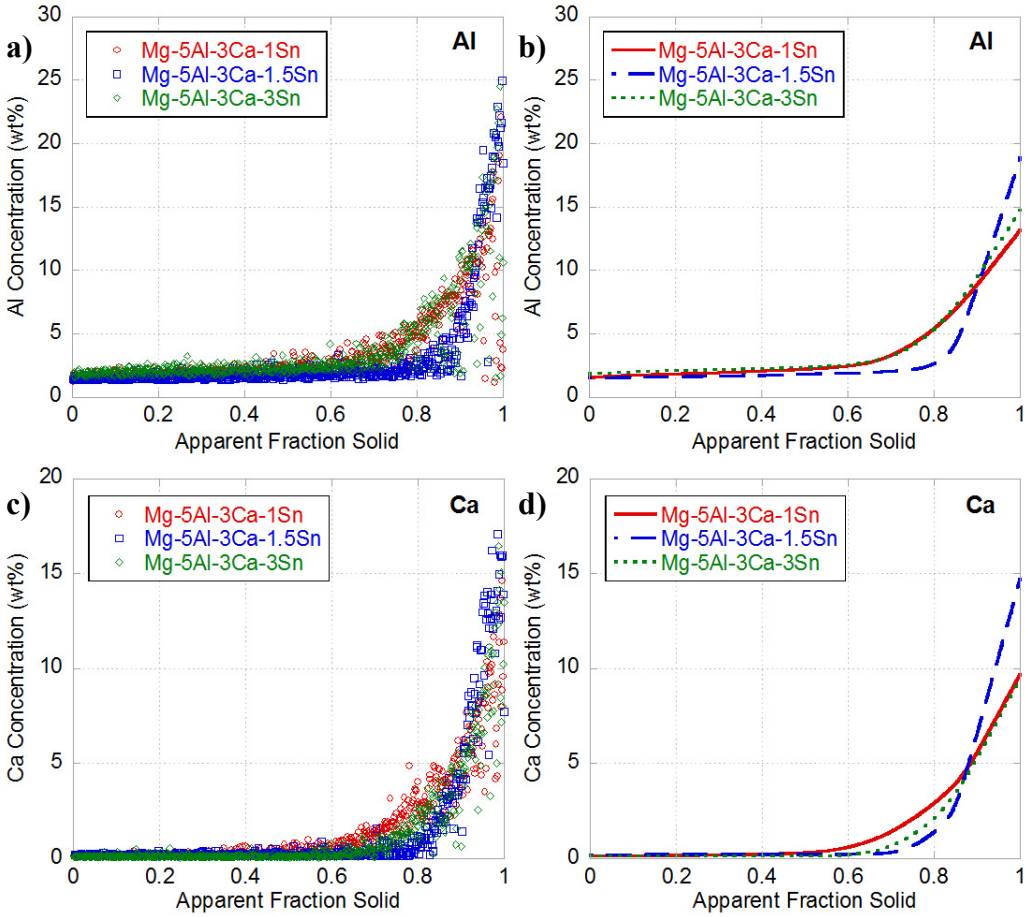

Figure 5.6 - Partitioning curves for alloys with CaMgSn as the first phase to solidify. a) Al - as sorted, b) Al - LMS fit, c) Ca - as sorted and d) Ca - LMS fit.

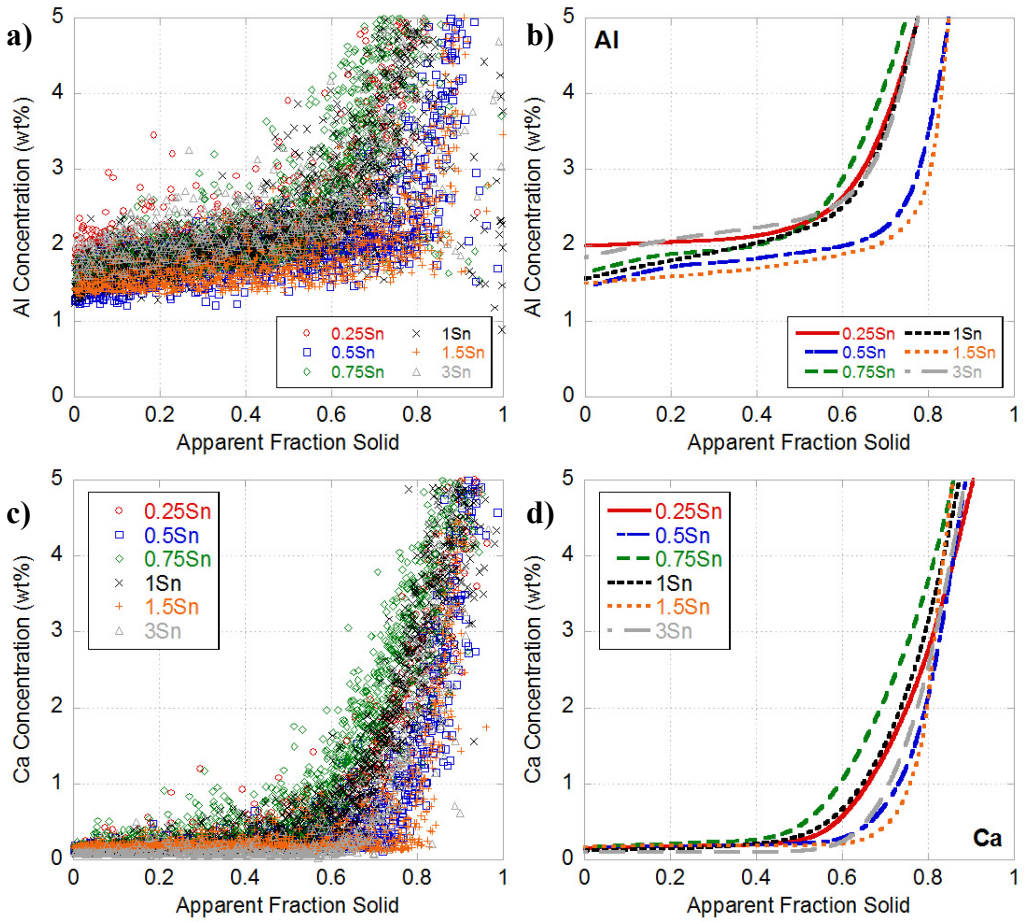

Figure 5.7 - Elemental partitioning curves for all Mg-5Al-3Ca-xSn alloys. a) Al - as sorted, b) Al - LMS fit, c) Ca - as sorted and d) Ca- LMS fit.

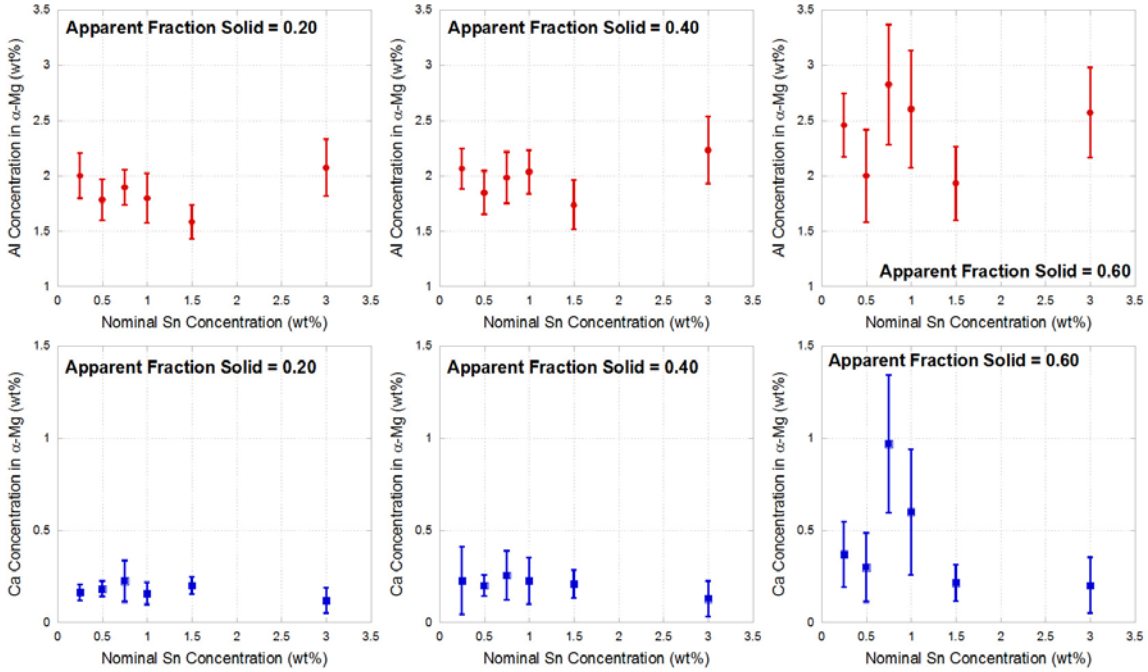

Figure 5.8 - Comparison of measured Al and Ca concentrations in α-Mg at three different fractions solid.

Table 5-4 - Calculated Scheil partitioning coefficients for Mg-Al-Ca-Sn alloys

Alloy	k_{Mg}	k_{Al}	k_{Ca}	k_{Sn}
Mg-5Al-3Ca-0.25Sn	1.07	0.30	0.07	0.14
Mg-5Al-3Ca-0.5Sn	1.08	0.25	0.05	0.05
Mg-5Al-3Ca-0.75Sn	1.08	0.28	0.09	0.06
Mg-5Al-3Ca-1Sn	1.13	0.26	0.07	0.02
Mg-5Al-3Ca-1.5Sn	1.12	0.22	0.05	0.02
Mg-5Al-3Ca-3Sn	1.11	0.32	0.05	0.02
Mg-6.5Al-3Ca-0.5Sn	1.11	0.25	0.04	0.05
Mg-8Al-3Ca-0.5Sn	1.11	0.28	0.05	0.07
Mg-6.5Al-2.25Ca-0.8Sn	1.07	0.32	0.06	0.07
Mg-8Al-1Ca-0.8Sn	1.05	0.39	0.03	0.09

For alloys with greater than 1wt% Sn, CaMgSn is the first phase to solidify, with α-Mg forming second. Thus, the validity of sorting by decreasing Mg concentration must be considered for these alloys. The data for the Mg-5Al-3Ca-3Sn alloy was resorted according to decreasing Sn concentration, Figure 5.9. Using Sn concentration to sort

clearly captures the formation of the CaMgSn phase during solidification, but the formation of the C36 eutectic is difficult to distinguish compared with Figure 5.6, particularly for Al (Figure 5.9b). Mg-5Al-3Ca-3Sn has approximately 2% CaMgSn in the final solidified structure; the alloys with 1wt% and 1.5wt% Sn have less than 1% of this phase. The α-Mg phase, while not the first phase to solidify, comprises the majority of the microstructure, and starts forming at a fraction solid of ~1%, according to Pandat calculations. Thus, although it misses the primary CaMgSn phase that solidifies, sorting with a decreasing Mg concentration most accurately captures the entire range of solidification and is appropriate to use even for alloys with greater than 1wt% Sn.

The experimental partitioning curves for Mg-5Al-3Ca-0.75Sn and Mg-5Al-3Ca-1.5Sn have also been compared with Pandat Scheil simulations in Figure 5.10. The Scheil simulations are for the α-Mg phase only, while the experimental data includes information from all phases present. Thus, at large fraction solid, greater differences will exist between the experimental and simulated curves. For this reason, only the first half of solidification will be considered to minimize the complication of other phases. The predicted concentration of Al in the α-Mg phase, Figures 5.10a and 5.10c, is in better agreement with the experimental data than for the Ca, Figures 5.10b and 5.10d. It is not clear what causes this difference, but the higher than expected Ca concentration could be related to a decrease in Ca diffusivity in the α-Mg, or it could also indicate inaccuracies in the current thermodynamic model for the quaternary system. Based on the increased Ca partitioning observed in several of the alloys, it is likely that the addition of Sn is changing the free energy of the phases.

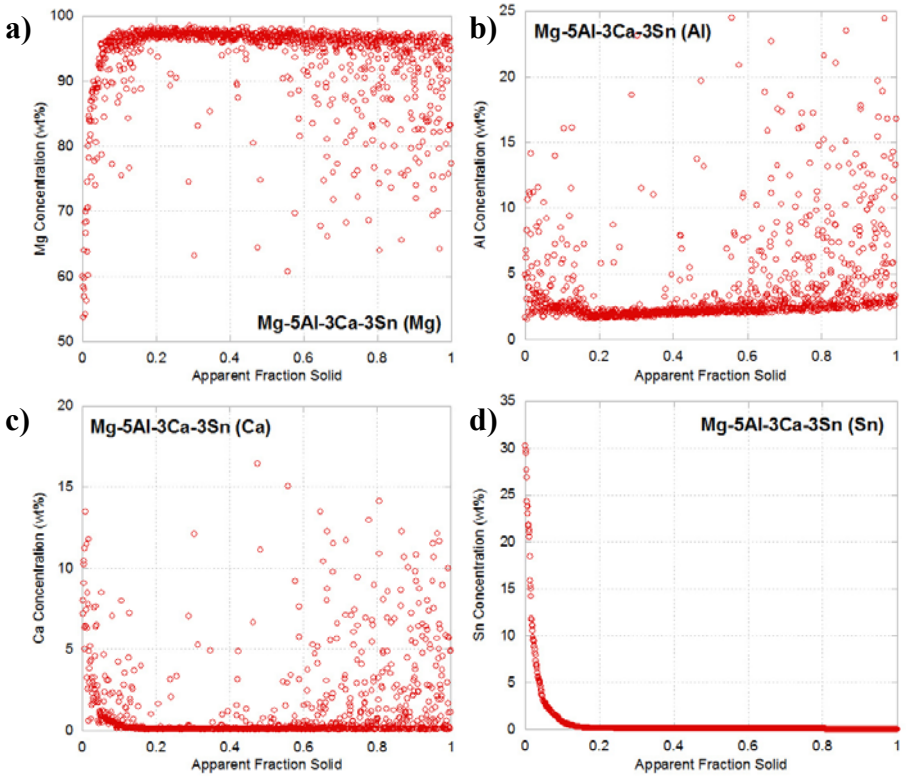

Figure 5.9 - Segregation profiles for a) Mg, b) Al, c) Ca and d) Sn for Mg-5Al-3Ca-3Sn. The data was sorted according to decreasing Sn concentration.

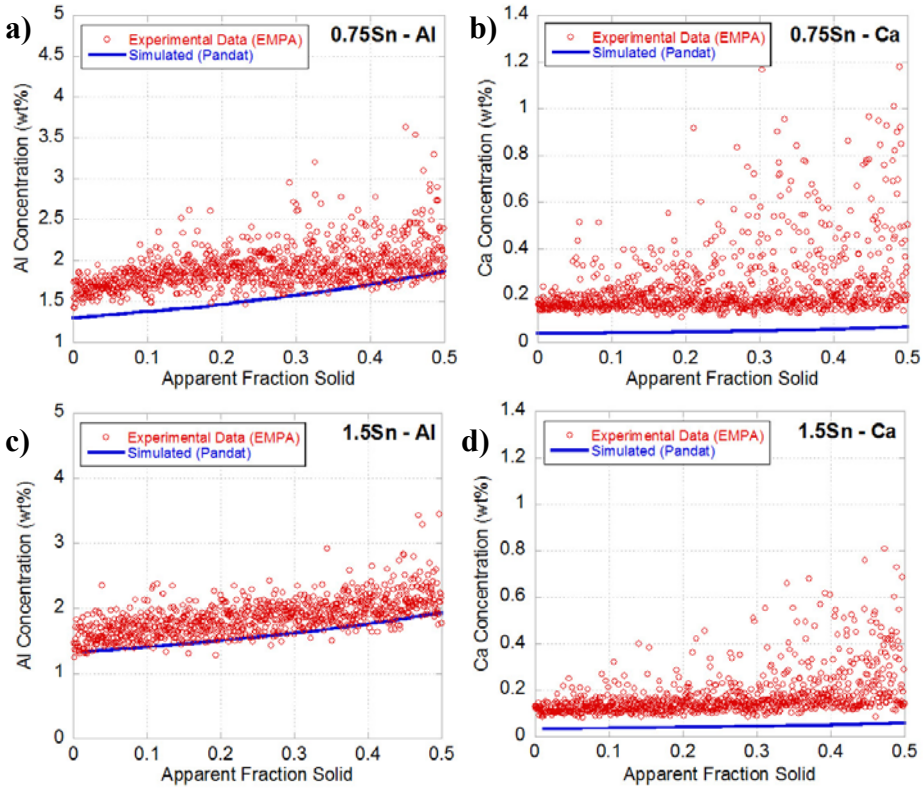

Figure 5.10 - Comparison of experimental partitioning curves and Pandat Scheil simulations for a) 0.75Sn - Al, b) 0.75Sn - Ca, c) 1.5Sn - Al and d) 1.5Sn - Ca.

5.2.2 Comparison of Model Mg-Al-Ca-Sn Alloys to Mg-Al-Ca-xSn-ySr Alloys

The partitioning curves for the Mg-5Al-3Ca-xSn alloys can also be compared with the alloys discussed in the previous chapter in Section 4.3. For this comparison, two of the quaternary alloys were selected: Mg-5Al-3Ca-0.75Sn, as an example of a quaternary alloy with increased Al and Ca partitioning, and Mg-5Al-3Ca-1.5Sn, with lower Al and Ca partitioning to the α-Mg phase. In Figure 5.11, the partitioning curves for these two alloys are plotted with the curves for AX44, AXJ530 and MRI230D, and calculated partitioning coefficients can be compared from Tables 4-3 and 5-4.

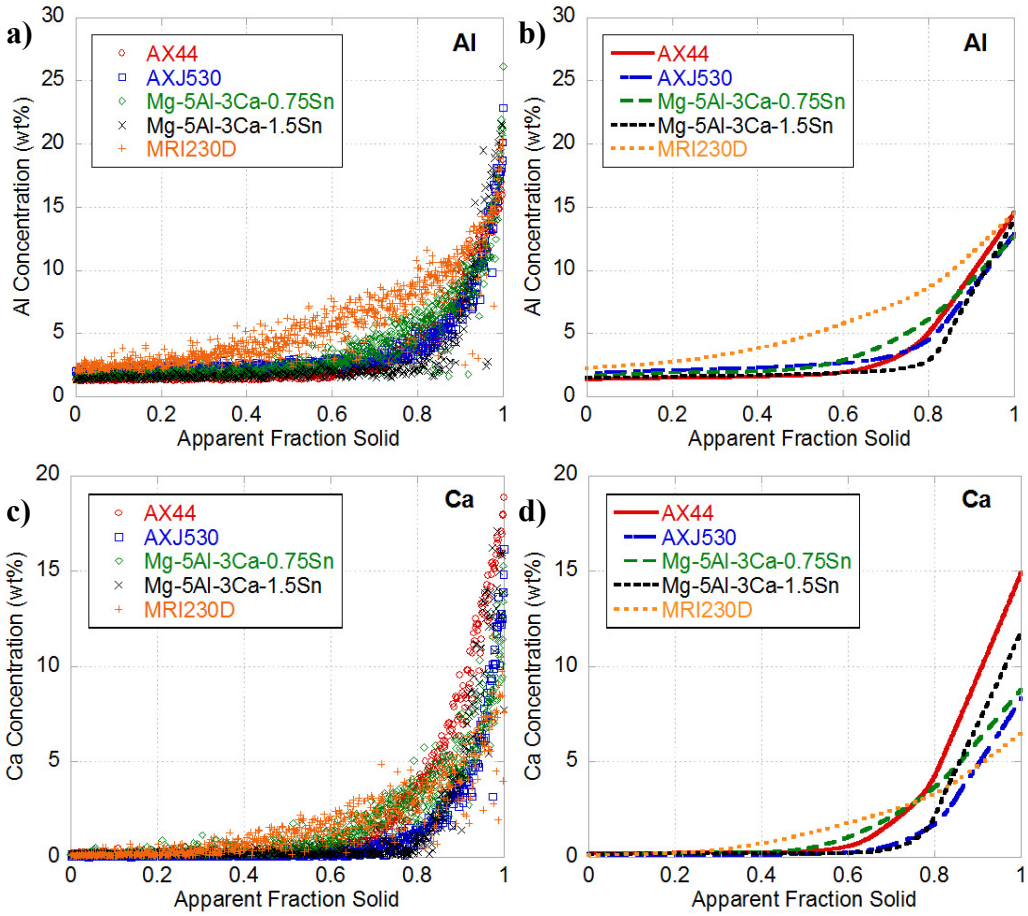

Figure 5.11 - Comparison of partitioning curves for the experimental quaternary and commercial alloys. a) Al - as sorted, b) Al - LMS fit, c) Ca - as sorted, and d) Ca - LMS fit.

Although the Mg-5Al-3Ca-1.5Sn has lower Al and Ca partitioning to the α-Mg phase than some of the other quaternary alloys, the Ca partitioning is very similar to that of AXJ530. The Al partitioning to the α-Mg is lower for the Mg-5Al-3Ca-1.5Sn than that observed for AXJ530 and AX44, however. For the Mg-5Al-3Ca-0.75Sn alloy, Al partitions less strongly to the α-Mg phase than it does for AXJ530, although the Al partitioning coefficient for the 0.75Sn alloy is higher than that of the 1.5Sn alloy. Greater partitioning of Ca to the α-Mg phase is observed for the 0.75Sn alloy than is observed for AXJ530 and AX44. AX44 has a nominal Ca composition that is 1wt% higher than the Mg-5Al-3Ca-0.75Sn, so this is a significant increase in Ca partitioning in the quaternary Sn-containing alloy. However, the increase in Ca partitioning to the α-Mg phase observed for the 0.75Sn alloy is not as great as that observed in MRI230D. The Sn additions do appear to increase the partitioning of Ca, but the effect was more modest

than expected based on the observed behavior in MRI230D. Sn additions actually slightly decrease the Al partitioning to the α-Mg phase compared with AXJ530 and AX44, leading to the conclusion that the increase in Al partitioning observed in MRI230D cannot be attributed to Sn.

The increased Ca partitioning in MRI230D is especially interesting, since this alloy has a lower nominal Ca concentration (2.25wt%) than the other alloys. This leads to the question of what accounts for the dramatic increase in partitioning observed in MRI230D. The Al and Ca partitioning behavior of MRI230D (Mg-6.5Al-2.25Ca-0.25Sr-0.8Sn) was compared with the Mg-6.5Al-2.25Ca-0.8Sn alloy that was cast as part of the current study, Figure 5.12. MRI230D has increased Al and Ca partitioning to the α-Mg phase compared with the quaternary alloy, Table 5-4. The only major difference between these two alloys is that MRI230D also contains 0.25wt% Sr. This suggests that it is the combination of Sn and Sr in this alloy leads to the greater Al and Ca partitioning to the α-Mg phase that is observed, although the effects of Sr additions are currently still under investigation. In an earlier investigation, Suzuki et al. reported that Sr additions can increase the partitioning of Al to the α-Mg phase in Mg-Al-(Ca,Sr) alloys [3], while Saddock has suggested that the Sr present in AXJ530 accounts for the observed difference in partitioning between AXJ530 and AX44 [4].

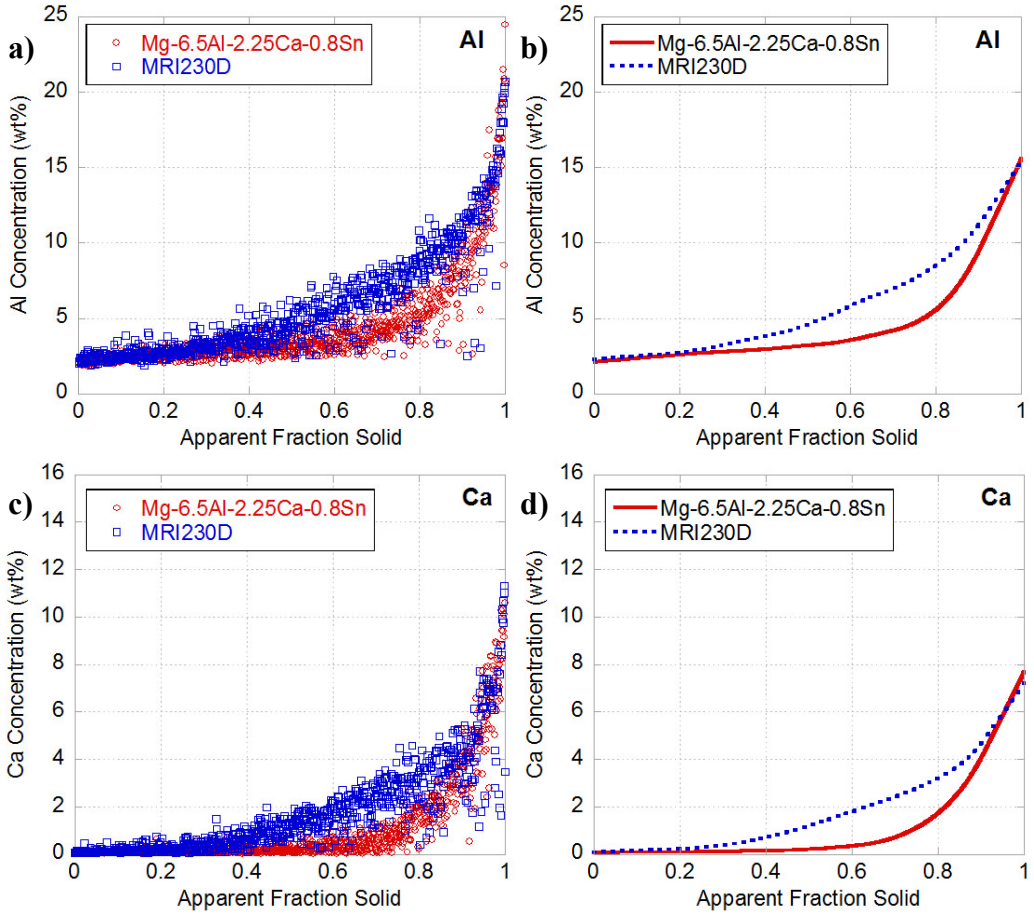

Figure 5.12 - Comparison of partitioning curves for Mg-6.5Al-2.25Ca-0.8Sn and MRI230D (Mg-6.5Al-2.25Ca-0.25Sr-0.8Sn). a) Al - as sorted, b) Al - LMS fit, c) Ca - as sorted, d) Ca- LMS fit.

5.2.3 Mg-xAl-3Ca-0.5Sn Alloys

The Al and Ca partitioning curves for Mg-5Al-3Ca-0.5Sn, Mg-6.5Al-3Ca-0.5Sn and Mg-8Al-3Ca-0.5Sn alloys are shown in Figure 5.13. The Al partitioning for these alloys increases slightly with increasing nominal Al concentration, Table 5-4. As was seen with MRI230D and MRI153M, a higher nominal Al concentration leads to an increased average Al concentration in the primary α-Mg phase. Of greater interest is the Ca partitioning, which is relatively unaffected by the increase in nominal Al concentration, Table 5-4. Thus, increasing the nominal Al concentration does not significantly affect the Al or Ca partitioning to the α-Mg phase when the nominal Ca and Sn concentrations are held constant. The average Al concentration in the α-Mg increases as the nominal Al concentration increases, however.

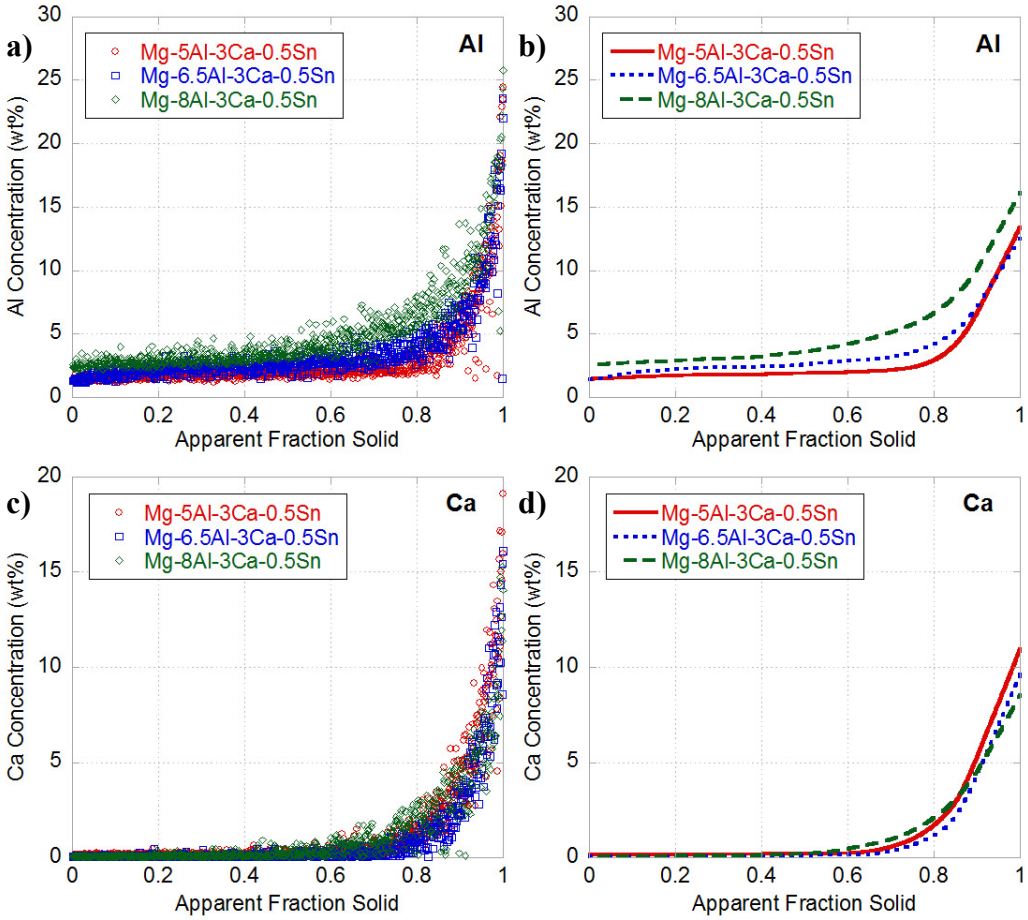

Figure 5.13 - Partitioning curves for Mg-xAl-3Ca-0.5Sn. a) Al - as sorted, b) Al - LMS fit, c) Ca - as sorted and d) Ca - LMS fit.

5.2.4 Sn Additions to MRI153M

An Mg-8Al-1Ca-0.8Sn alloy was cast and the partitioning behavior determined, Figure 5.14, to examine the effect of Sn additions on high Al, low Ca alloys such as MRI153M. MRI153M contains 0.27wt% Sr, so this is in effect a comparison of the effect on microsegregation of 0.27wt% Sr and 0.8wt% Sn. The nominal Sn concentration of 0.8wt% was selected because MRI230D contains 0.8wt% Sn. The Mg-8Al-1Ca-0.8Sn alloy had a lower average Al concentration in the α-Mg phase than MRI153M, and the calculated Al partitioning coefficient is also lower for the quaternary alloy, Table 5-4. The Ca partitioning coefficient is significantly reduced for the quaternary alloy compared with MRI153M, and the average Ca concentration in the α-Mg is also lower. The amount of Al supersaturation in the near-interdendritic region is also reduced in Mg-8Al-1Ca-

0.8Sn compared with MRI153M; however, this is most likely because of the increased amount of β-$Mg_{17}Al_{12}$ in the interdendritic region for the quaternary alloy.

5.2.5 Summary of Elemental Partitioning Behavior

Elemental partitioning has been studied for three series of Mg-Al-Ca-Sn alloys. Increasing the nominal Al concentration while holding the Ca and Sn concentrations constant did not significantly affect Al or Ca partitioning to the α-Mg phase. Al partitioning to the α-Mg was slightly decreased compared with AX44 and AXJ530 for the Mg-5Al-3Ca-xSn series of alloys, but greater Ca partitioning to the α-Mg phase was observed for the alloys with 0.25wt%, 0.75wt% and 1.0wt% Sn. MRI230D had significantly higher Al and Ca partitioning compared with the Mg-5Al-3Ca-xSn alloys and Mg-6.5Al-2.25Ca-0.8Sn, suggesting that Sr may also contribute to the increased partitioning in MRI230D. In the next section, the effect on creep resistance of this variation in Al and Ca partitioning to the α-Mg phase will be examined.

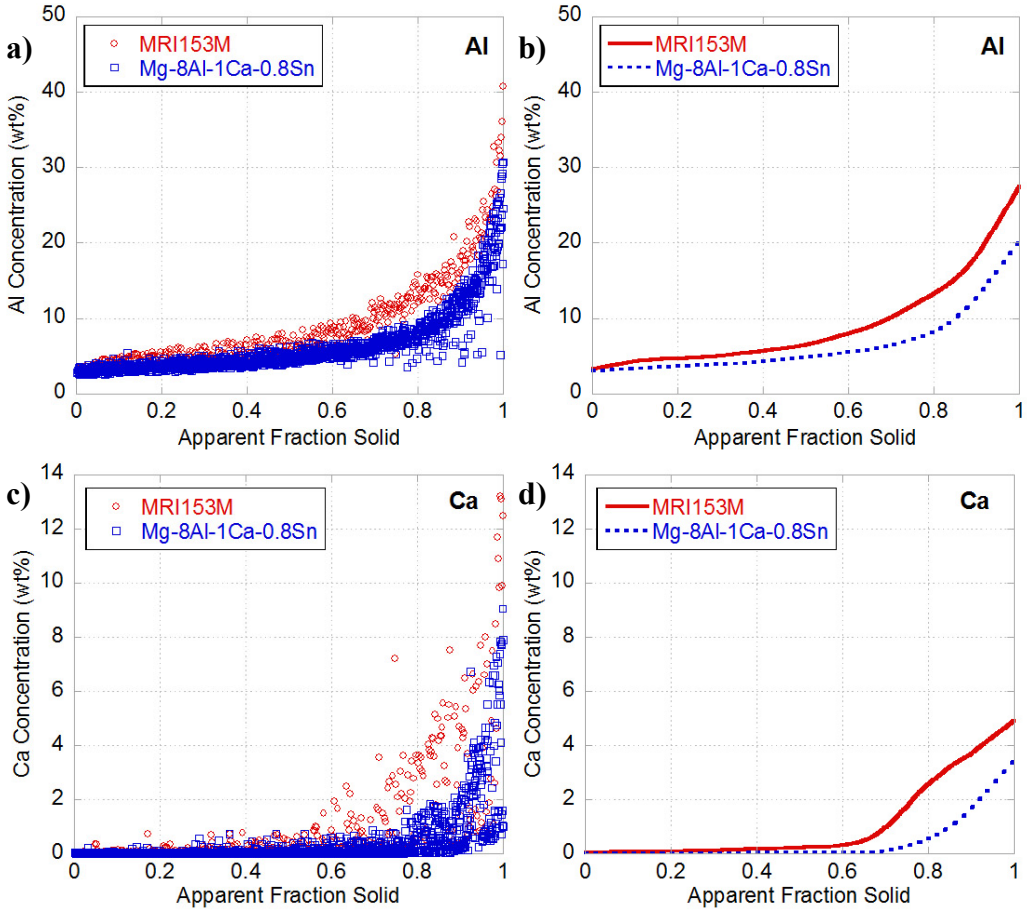

Figure 5.14 - Comparison of partitioning curves of Mg-8Al-1Ca-0.8Sn and MRI153M (Mg-8Al-1Ca-0.27Sr). a) Al - as sorted, b) Al- LMS fit, c) Ca - as sorted and d) Ca - LMS fit.

5.3 Compressive Creep

The effect of partitioning differences on creep behavior was investigated in an effort to determine whether increased Al and Ca partitioning to the α-Mg phase leads to improved creep resistance. Given the small volume of material that was cast during preparation of the quaternary alloys and the lack of availability of die-cast specimens, compressive creep tests were conducted using specimens prepared from the 25 g induction melted samples. These specimens have larger grain sizes than die-cast specimens, and Saddock has shown that larger grain sizes lead to a higher minimum creep rate in AXJ530 [4]. Grain sizes have not been directly measured for the quaternary alloys, but are expected to be similar to that of permanent mold cast alloys, ~150-200 μm [4], given the similar cooling rates. Direct comparison of the minimum creep rates in the compression tests to those measured using die-cast tensile creep specimens discussed in

Chapter 3 will therefore not be possible. However, dislocation substructures in as-crept material for both specimen types will be analyzed in Section 5.3.3. Testing was carried out at 110 MPa at both 150°C and 180°C, similar to the conditions used in Section 3.1.

5.3.1 Creep Behavior at 110 MPa and 180°C

Within the Mg-5Al-3Ca-xSn series of alloys cast in this study, two have been selected for creep testing – Mg-5Al-3Ca-0.75Sn and Mg-5Al-3Ca-1.5Sn, Figure 5.15. The alloy with 1.5wt% Sn had lower Al and Ca partitioning to the α-Mg phase than the 0.75Sn alloy. At least three specimens were tested for each alloy, to account for microstructural variability within the casting and to confirm that the results obtained are representative of the creep behavior of the alloy. The 0.75Sn alloy exhibited better creep resistance than the 1.5Sn alloy, Table 5-5. The minimum creep rate of the 1.5Sn alloy varied between 2.3×10^{-7} and 3.6×10^{-7} s^{-1}, with an average value of 3.0×10^{-7} s^{-1}, while the minimum creep rate for the 0.7Sn alloy averaged 1.4×10^{-7} s^{-1}. The minimum creep rate is therefore ~2 times higher for the 1.5Sn alloy at this temperature, suggesting that increased Al and Ca partitioning to the α-Mg phase may be modestly beneficial for creep resistance.

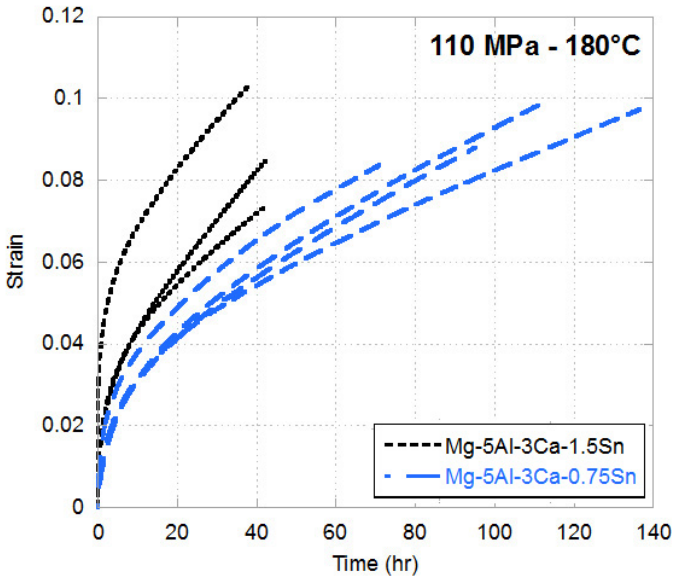

Figure 5.15 – Compressive creep curves for Mg-5Al-3Ca-0.75Sn and Mg-5Al-3Ca-1.5Sn tested at 110 MPa and 180°C.

Table 5-5 - Minimum creep rates at 110 MPa and 180°C

Alloy	Minimum Creep Rate ($\times 10^{-7}$ s^{-1})	Average Minimum Creep Rate ($\times 10^{-7}$ s^{-1})	Average % Al in α-Mg	Average % Ca in α-Mg
Mg-5Al-3Ca-0.75Sn	1.51	1.40	2.19	0.47
	1.16			
	1.39			
	1.54			
Mg-5Al-3Ca-1.5Sn	3.13	3.00	1.71	0.21
	3.58			
	2.29			
Mg-6.5Al-2.25Ca-0.8Sn	3.30	2.51	2.93	0.20
	2.12			
	2.10			
MRI230D	1.97	2.51	3.83	0.78
	3.01			
	2.54			

Based on these results, it is expected that MRI230D, which has even greater Al and Ca partitioning to the α-Mg phase than the 0.75Sn alloy, would have better creep resistance than the two quaternary alloys. However, the measured creep resistance of MRI230D falls between the creep resistances of the two quaternary alloys, Figure 5.16. The minimum creep rates are again listed in Table 5-4, and the average for MRI230D has been calculated to be 2.5×10^{-7} s^{-1}, approximately 1.8 times higher than that of Mg-5Al-3Ca-0.75Sn.

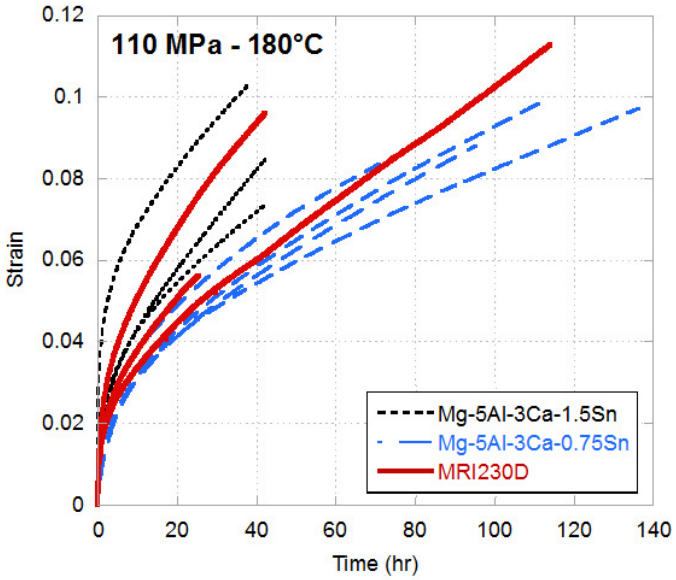

Figure 5.16 - Compressive creep curves for Mg-5Al-3Ca-0.75Sn, Mg-5Al-3Ca-1.5Sn and MRI230D, tested at 110 MPa and 180°C.

What then accounts for the difference in creep rate between MRI230D and the 0.7Sn alloy? From an earlier study by Suzuki et al., the minimum creep rate for an as-die-cast AXJ530 specimen was ~1.5-2 times higher than the creep rate for an aged AXJ530 specimen. This difference in creep resistance was attributed to the presence of Al_2Ca precipitates in the α-Mg matrix of the aged sample. These precipitates were not present in the as-cast condition. Given the orientation of the precipitates – plates parallel to the basal plane of the α-Mg phase – only a modest amount of strengthening could be obtained [5]. Considering the similar magnitude of improvement for the 0.75Sn alloy compared with MRI230D, it thus seems reasonable to suggest that precipitation strengthening is applicable in this case as well.

To confirm if precipitation is possible in these alloys at 180°C, two different experiments were conducted. First, the hardness was measured after aging for 100 hours at 180°C, which was comparable to the longest creep test conducted at this temperature. Second, TEM images of crept specimens were examined to determine if precipitation occurred with thermal exposure. The as-cast and aged hardness of the three alloys are listed in Table 5-6. Only Mg-5Al-3Ca-0.75Sn showed an increase in hardness after the aging treatment, which suggests that the precipitates present in this alloy had sufficient size/spacing for effective strengthening. This is further confirmed by the TEM images

shown in Figure 5.17. Although precipitates are observed in all three samples, the precipitates are finer in the 0.75Sn alloy. A greater volume fraction of precipitates may also be present in this alloy, although more areas would need to be examined to determine this conclusively. The implications of this will be discussed in more detail later in this chapter.

Table 5-6 - Vickers hardness of selected alloys

Alloy Composition	As-cast Hardness (Hv)	Aged Hardness (Hv)
Mg-5Al-3Ca-0.75Sn	62.1 +/- 3.5	70.5 +/- 6.2
Mg-5Al-3Ca-1.5Sn	56.7 +/- 4.1	56.2 +/- 9.0
Mg-6.5Al-2.25Ca-0.25Sr-0.8Sn (MRI230D)	66.7 +/- 5.5	66.1 +/- 6.9

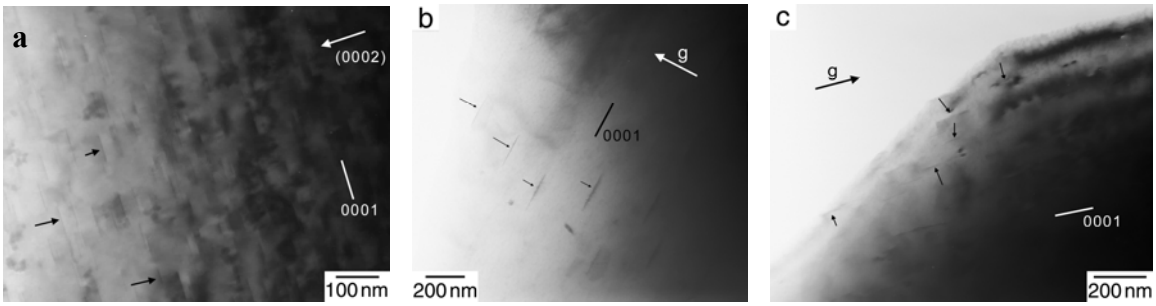

Figure 5.17 - TEM BF micrographs of samples of a) Mg-5Al-3Ca-0.75Sn, b) MRI230D and c) Mg-5Al-3Ca-1.5Sn crept at 110 MPa and 180°C. ZA = $[11\bar{2}0]$ and g = (0002) for a-b) and $(1\,\bar{1}\,00)$ for c). Several precipitates are indicated by the small arrows.

Several Mg-6.5Al-2.25Ca-0.8Sn specimens were also crept in compression for comparison with the behavior observed in MRI230D, Figure 5.18. The average minimum creep rate for both alloys is 2.51×10^{-7} s^{-1}, indicating that the 0.25wt% Sr present in MRI230D has minimal impact on the creep resistance of this alloy despite the difference in partitioning, at least under this temperature and stress condition.

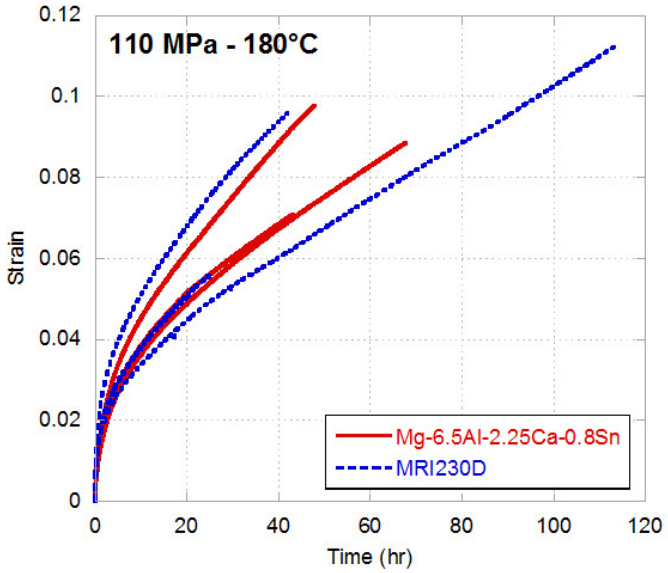

Figure 5.18 - Compressive creep curves for MRI230D and Mg-6.5Al-2.25Ca-0.8Sn, crept at 110 MPa and 180°C.

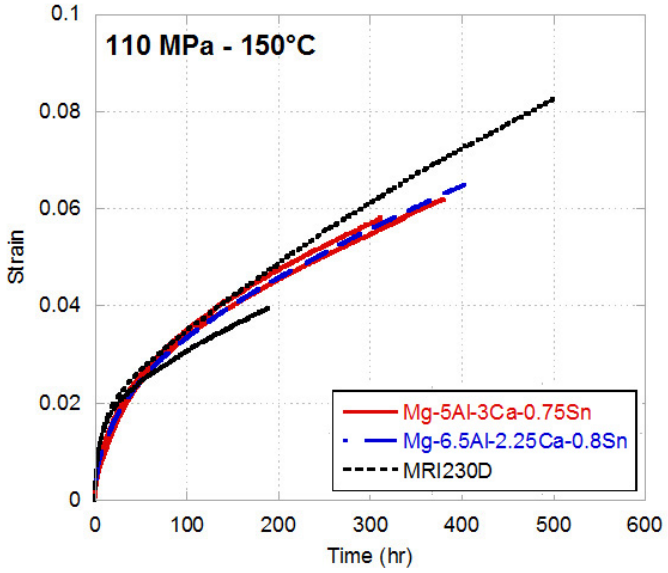

Figure 5.19 - Compressive creep curves for alloys tested at 110 MPa and 150°C.

5.3.2 Creep Behavior at 110 MPa and 150°C

Mg-5Al-3Ca-0.75Sn, Mg-6.5Al-2.25Ca-0.8Sn and MRI230D were crept in compression at 110 MPa and 150°C, and creep curves are shown in Figure 5.19. Minimum creep rates are listed in Table 5-7. Unlike the behavior observed at 180°C, similar minimum creep rates are observed for all three alloys tested at 150°C. The differences at 180°C were attributed to increased precipitation strengthening in the Mg-

5Al-3Ca-0.8Sn alloy. The similarity in creep behavior at 150°C may also be explained in terms of precipitation.

Although precipitates are thermodynamically possible at both temperatures (150 and 180°C), kinetics ultimately control the precipitation process. At lower temperatures, the start of precipitation will be delayed to longer times during high temperature exposure, given the slower rate of diffusion at these temperatures. The nucleation rate of precipitates can be related to the diffusion rate through the following equations:

$$\frac{dN}{dt} \cong N_0 Z\beta \exp\left(\frac{-\Delta G^*}{kT}\right) \qquad (5\text{-}1),$$

where N_0 is the number of atoms per unit volume, Z is Zeldovich's factor (~1/20), k is Boltzmann's constant, T is temperature, ΔG^* is the barrier to nucleation, and β is a frequency factor known as the atomic impingement rate that can be written as:

$$\beta = \frac{4\pi R^{*2} D_{Ca}^{\alpha} X_{Ca}^{bulk}}{a_0^4} \qquad (5\text{-}2),$$

when only Ca, as the slowest diffusing element involved in the precipitation process, is considered. In this frequency factor, R^* is the critical radius, a_0 is the lattice parameter, D_{Ca}^{α} is the diffusivity of Ca in Mg, and X_{Ca}^{bulk} is the Ca concentration of the alloy [6-8]. Thus, the nucleation rate is expected to decrease as both the temperature and diffusivity decrease. This is illustrated by the TTT curve for AXJ530, Figure 5.20, which was experimentally determined by Suzuki et al. [9]. Although the TTT curve has not been determined for the alloys in the current investigation, a similar shape is expected based on the creep behavior at 150 and 180°C. However, considering that the nucleation behavior at 150°C is not that different from 180°C, especially for the times experienced in the creep tests, and that precipitates were present in the as-cast alloys, nucleation is not expected to be the determining factor kinetically for these alloys.

Instead, growth and coarsening of precipitates is likely the controlling factor. As was discussed in Section 4.2, precipitates present in the as-cast microstructure will grow and coarsen at different rates depending on temperature. The optimum precipitate size and spacing for strengthening (peak aging condition) requires longer exposure times at lower temperatures, Figure 4.4. This exposure time will also differ from alloy to alloy, depending on diffusivity, local solute concentration, initial particle size and interfacial

energy [8]. At 180°C, only Mg-5Al-3Ca-0.75Sn had an increased hardness after aging for 100 hours, and correspondingly, the lowest minimum creep rate was measured for this alloy. The other two alloys (Mg-5Al-3Ca-1.5Sn and MRI230D) decreased in hardness from the as-cast state, indicating that the precipitates present were less efficient in strengthening compared with those present in Mg-5Al-3Ca-0.75Sn. At 150°C, the minimum creep rates for all the alloys were similar, indicating that the precipitates present were not of sufficient size/spacing for strengthening. The thermal exposure times during creep testing were either too short to reach the peak hardness (underaging), or were too long and led to coarsening (overaging), illustrated schematically in Figure 5.21. Precipitate strengthening will be discussed in more detail in Section 5.4.2.

Table 5-7 – Minimum creep rates at 110 MPa and 150°C

Alloy	Minimum Creep Rate (s^{-1})
Mg-5Al-3Ca-0.75Sn	2.57×10^{-8}
	2.49×10^{-8}
Mg-6.5Al-2.25Ca-0.8Sn	2.55×10^{-8}
MRI230D	2.78×10^{-8}
	2.75×10^{-8}

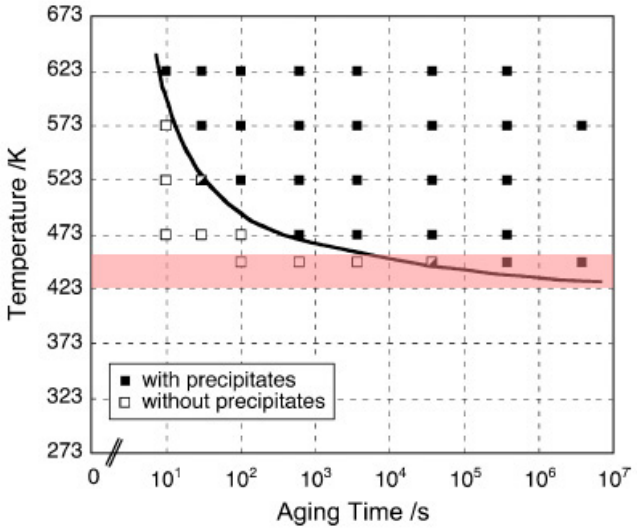

Figure 5.20 - TTT curve for die-cast AXJ530 [9]. The range of creep temperatures used in the current study is highlighted.

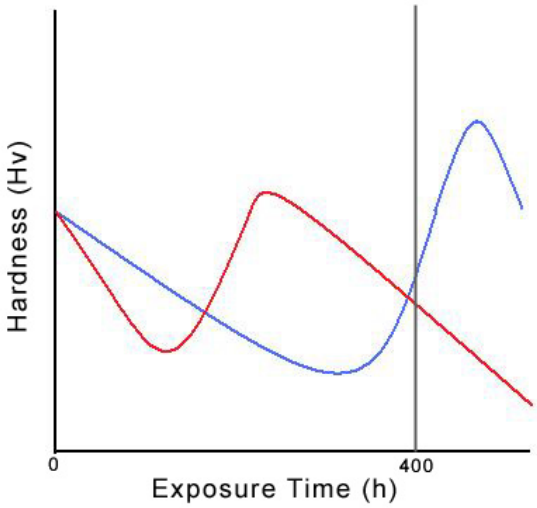

Figure 5.21 - Schematic of hardness vs aging time. The vertical gray line indicates an exposure time of 400 h. Both curves have a decreased hardness compared with the initial hardness at this exposure time, but the red represents a material that has overaged, while the blue is an underaged material.

5.3.3 Dislocation Substructures

Dislocation substructures have been examined by TEM for specimens crept at 110 MPa. Shown in Figure 5.22 are images from an MRI230D specimen crept at 150°C, which had accumulated approximately 4% strain when the test was interrupted after 190 hours. A zone axis of $[11\bar{2}0]$ was used for imaging, and <a> dislocations will be invisible in Figures 5.22b and 5.22d. The majority of the dislocations observed are basal <a> type dislocations with some non-basal <a> dislocations also present. The basal <a> dislocations are aligned parallel to the basal trace indicated in Figure 5.22a and 5.22c with this foil orientation.

The dislocations shown in Figure 5.22 can be compared with those produced in an MRI230D specimen tested at 180°C, Figure 5.23. In this case, the specimen had accumulated 9.6% creep strain when the test was interrupted after 42 hours. Again, basal <a> dislocations are also observed (Figure 5.23a-b), which interact very weakly with the Al_2Ca precipitates present. Some non-basal <a> dislocations are also present. It is not possible to distinguish between basal and non-basal <a> dislocation in Figure 5.23c-d, but precipitates of Al_2Ca are observed in Figure 5.23d.

A sample of Mg-5Al-3Ca-0.75Sn crept at 180°C was also examined, and is shown in Figure 5.24. The specimen had accumulated 8.4% strain when the test was

interrupted after 71 hours. As with the MRI230D specimen, the dislocations are mostly basal <a> type with some non-basal <a> also present, and interact only weakly with the basal precipitates. However, as will be discussed in the next section, modest increases in strength can still result from the interaction of <a> dislocations with basal precipitates.

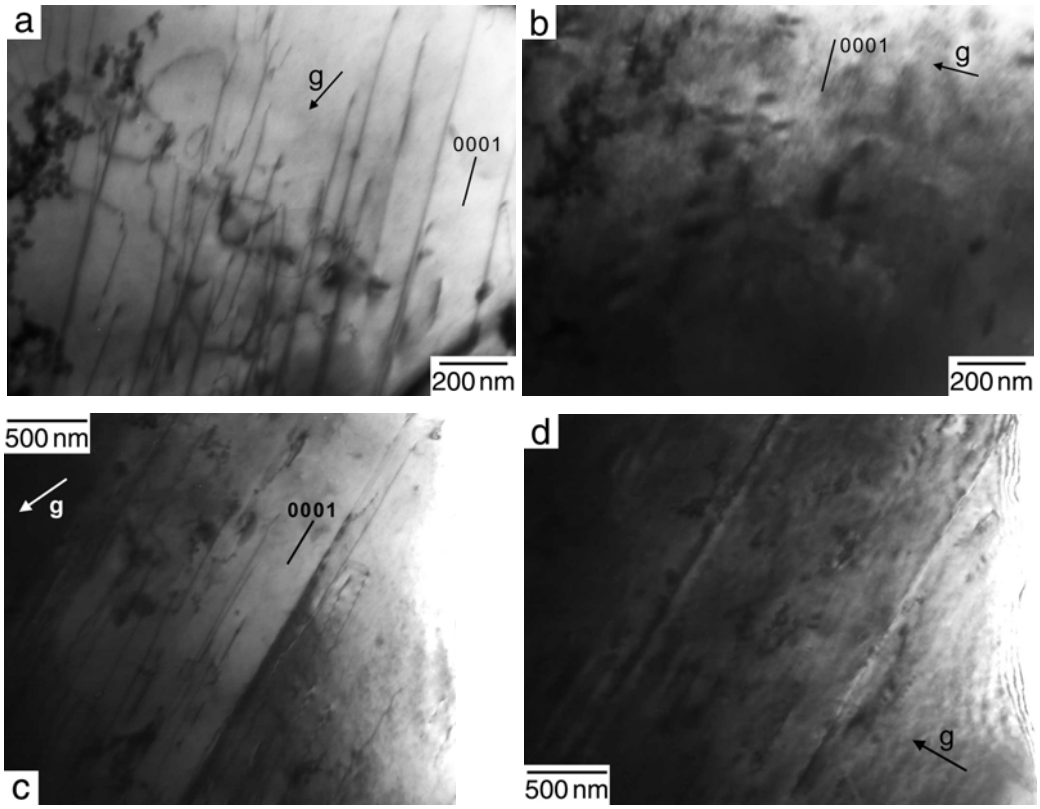

Figure 5.22 - TEM BF images of a specimen crept at 110 MPa and 150°C. Zone axis = $[11\bar{2}0]$ **and g =** $(1\bar{1}01)$ **for a) and c). g =** (0002) **for b) and d). <a> dislocations are invisible in b) and d).**

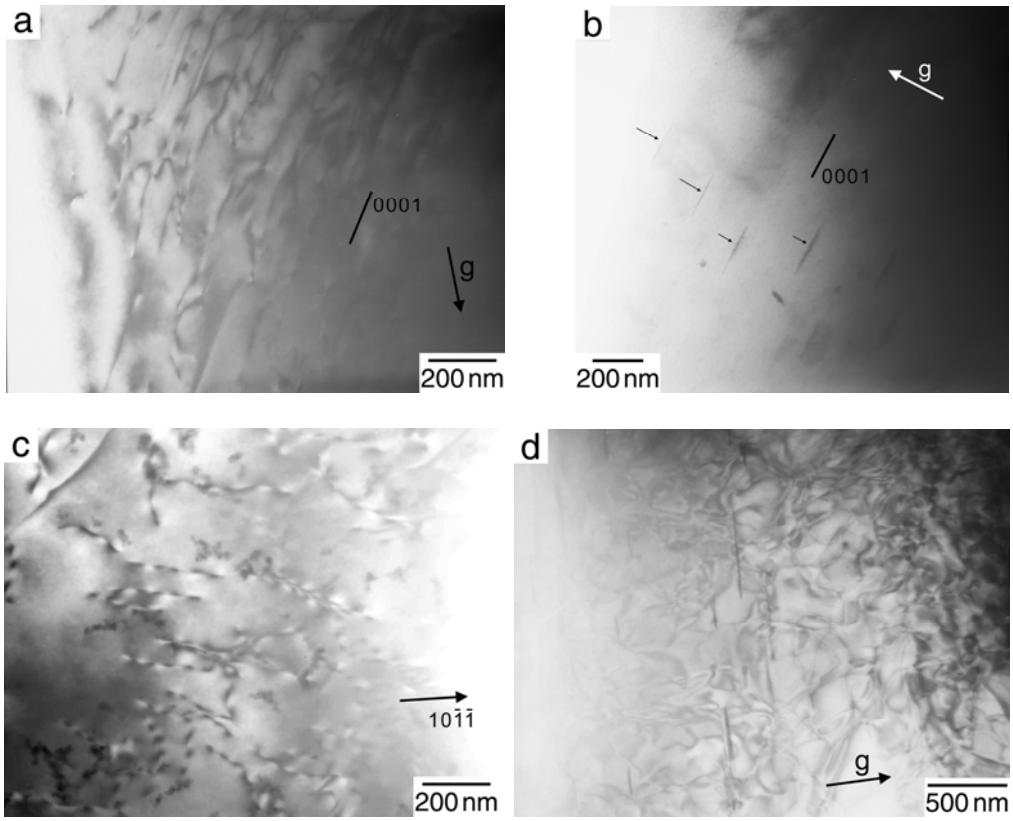

Figure 5.23 - TEM BF images of a specimen of MRI230D crept at 110 MPa and 180°C. a) B = $[11\bar{2}0]$ **and g =** $(1\,\bar{1}\,01)$**, b) same area, but g =** (0002)**, c) different area: B =** $[01\,\bar{1}\,1]$ **and g =** $(10\,\bar{1}\,\bar{1})$**, d) third area, B =** $[0001]$ **and g =** $(\bar{1}\,100)$**. <a> dislocations are invisible in b).**

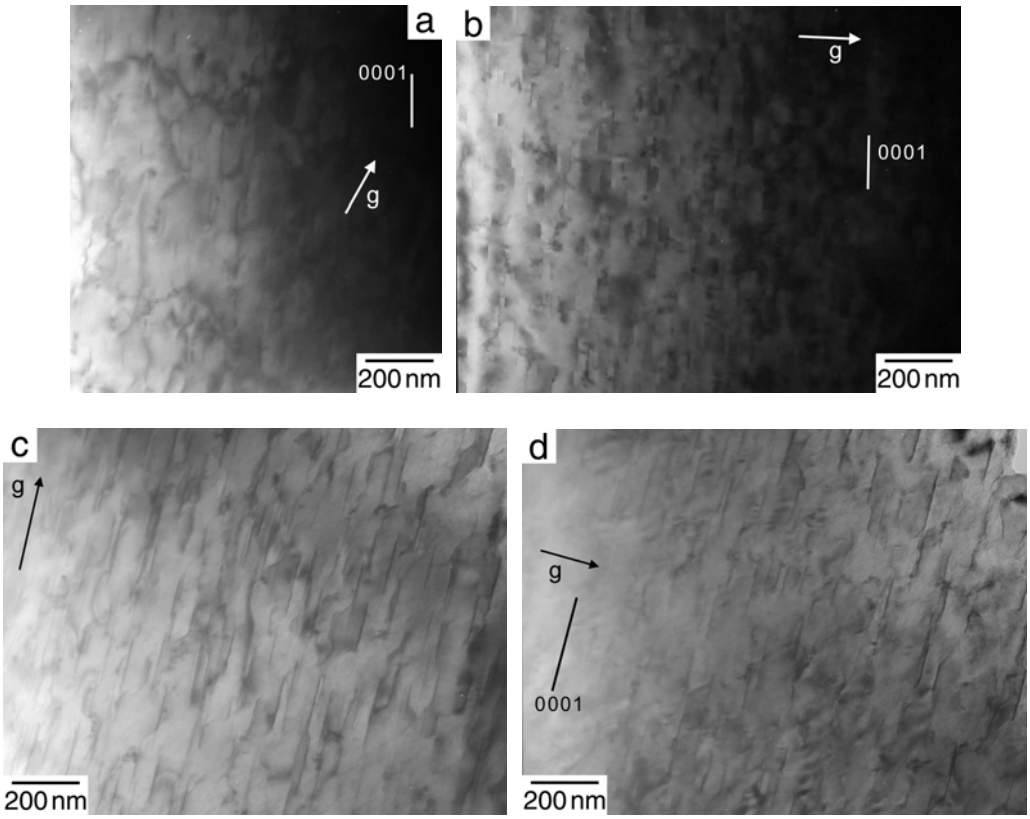

Figure 5.24 - TEM BF images of an Mg-5Al-3Ca-0.75Sn specimen crept at 110 MPa and 180°C. a) B = $[11\bar{2}0]$ and g = $(1\bar{1}01)$, b) same area, but g = (0002), c) different area: B = $[01\bar{1}0]$ and g = $(2\bar{1}\bar{1}0)$, d) same area but g = (0002). <a> dislocation are invisible in b) and d).

The dislocation substructures observed for the induction melted samples were similar to the substructures seen in the die-cast material, discussed in Section 3.4. Images from two die-cast specimens (MRI230D and AXJ530) crept in tension are shown in Figure 5.25 for comparison with the compression samples, Figures 5.22-5.24. Despite the differences in alloy composition, casting technique and testing condition, mainly <a> dislocations (basal and non-basal) were observed in each specimen. This indicates that the same creep mechanism, viscous glide, is in operation. The creep rate should thus be affected by both solute and precipitation strengthening in the α-Mg phase, which will be described in the next section.

5.3.4 Summary of Creep Deformation in Mg-Al-Ca-Sn Alloys

Compressive creep behavior at 110 MPa has been examined for four alloys: Mg-5Al-3Ca-0.75Sn, Mg-5Al-3Ca-1.5Sn, Mg-6.5Al-2.25Ca-0.8Sn and MRI230D. Despite

having the greatest partitioning of Al and Ca to the α-Mg phase, MRI230D did not have the lowest minimum creep rate at either 150 or 180°C. Minimum creep rates at 150°C were almost identical for all four alloys, while at 180°C the Mg-5Al-3Ca-0.75Sn alloy had a minimum creep rate that was approximately two times lower than the other alloys. Similar dislocation substructures are observed for the quaternary alloys, consisting predominantly of basal and non-basal <a> dislocations. As in the die-cast Mg-Al-Ca-xSr-ySn alloys studied in Chapter 3, viscous glide of dislocations has been identified as the operative creep deformation mechanism. Precipitates were observed in crept samples, and varied in size from alloy to alloy. The strengthening contribution of these precipitates will be discussed in the next section, along with the contribution of the measured solute concentrations.

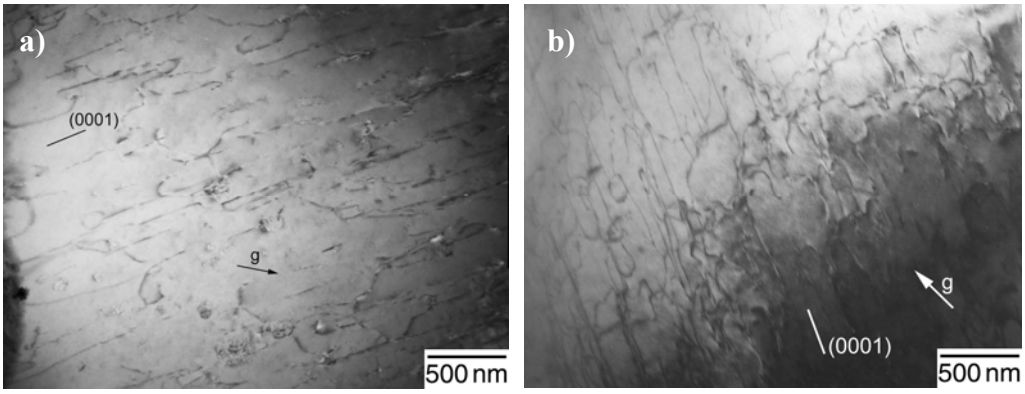

Figure 5.25 – BF TEM images of two die-cast specimens crept in tension at 110 MPa and 180°C. a) MRI230D (0.70% strain, 38 hours to failure) and b) AXJ530 (3.64% strain when test interrupted after 500 hours). B = $[11\bar{2}0]$ **and g =** $(1\bar{1}01)$ **for both images.**

5.4 Solute and Precipitation Strengthening at 180°C

Creep deformation of Mg-Al-Ca alloys occurs predominantly by the glide of <a> type dislocations along basal and non-basal planes. Thus, by inhibiting dislocation motion in the α-Mg phase, whether through increased solute in the matrix or by the formation of precipitate phases, creep resistance can be improved. The alloys in the current study have been shown to have varying levels of solute and precipitation strengthening, which should influence creep behavior. In the remainder of Chapter 5 the contribution of solute and precipitation strengthening to creep behavior at 180°C is examined.

5.4.1 Solute Strengthening During Creep

As described in Section 4.4, the creep rate in a solute strengthened alloy can be related to solute concentration, atomic misfit and diffusivity [10]:

$$\dot{\varepsilon} \approx \frac{\pi(1-\nu)kT\widetilde{D}}{6e^2cb^5G}\left(\frac{\sigma}{G}\right)^3 \qquad (4\text{-}1),$$

where ν is Poisson's ratio, σ is the applied stress, k is Boltzmann's constant, T is the absolute temperature, $\widetilde{D}$ is the interdiffusion coefficient for the solute, G is the shear modulus, b is the Burgers vector, e is the solute-solvent size difference and c is the concentration of solute. The largest ($e^2c/\widetilde{D}$) term corresponds to the lowest creep rate, assuming all other terms are similar for the alloys. Table 5-8 includes the solute concentration from the experimentally measured data as well as the predictions from Pandat. For both of these, average concentrations have been calculated for solid fractions from 0 to 0.7, while maximum concentrations have been determined for a fraction solid of ~0.7 and correspond to the concentration of the α-Mg phase in the near-interdendritic region. Eutectic phases are expected to start forming around $f_s = 0.75$ for most of the alloys (Table 5-2). The Pandat Scheil simulations are for the α-Mg phase only, and for most alloys predict significantly lower Ca concentrations than are actually measured. Less variability in Ca concentration (maximum or average) is predicted by Pandat, and the predictions therefore fail to capture the wide range of Ca concentrations experimentally measured for the Mg-5Al-3Ca-xSn alloys. Therefore, the experimental average concentrations will be used for most of the ensuing calculations.

Table 5-8 - Solute concentration in α-Mg (at%) for the experimental alloys

Alloy	Al - Experimental		Al - Predicted		Ca - Experimental		Ca - Predicted	
	c_{max}	c_{avg}	c_{max}	c_{avg}	c_{max}	c_{avg}	c_{max}	c_{avg}
Mg-5Al-3Ca-0.25Sn	3.14	2.05	2.11	1.59	0.79	0.18	0.07	0.04
Mg-5Al-3Ca-0.5Sn	2.16	1.64	2.16	1.54	0.41	0.14	0.07	0.04
Mg-5Al-3Ca-0.75Sn	**3.64**	**1.99**	**2.20**	**1.53**	**1.28**	**0.29**	**0.07**	**0.04**
Mg-5Al-3Ca-1Sn	3.01	1.87	2.26	1.62	0.78	0.18	0.07	0.04
Mg-5Al-3Ca-1.5Sn	**1.88**	**1.54**	**2.37**	**1.71**	**0.23**	**0.13**	**0.06**	**0.04**
Mg-5Al-3Ca-3Sn	2.77	2.06	2.67	1.76	0.35	0.09	0.05	0.02
Mg-6.5Al-3Ca-0.5Sn	2.88	2.16	2.87	2.02	0.15	0.08	0.05	0.03
Mg-8Al-3Ca-0.5Sn	4.88	3.08	3.62	2.93	0.47	0.15	0.03	0.03
Mg-6.5Al-2.25Ca-0.8Sn	**3.94**	**2.66**	**3.44**	**2.12**	**0.39**	**0.12**	**0.03**	**0.02**
Mg-8Al-1Ca-0.8Sn	5.99	3.91	5.49	3.00	0.11	0.04	0.01	0.01
MRI230D	**6.08**	**3.51**	**3.35**	**2.12**	**1.54**	**0.48**	**0.04**	**0.02**

Table 5-9 includes the calculated values of e^2c for the crept alloys discussed in the previous section (those listed in bold in Table 5-8). For these calculations, values of 0.124 and 0.204 were used for e for Al and Ca, respectively. If we assume that the diffusion coefficient of Al in Mg is 3.32×10^{-16} cm^2/s at 180°C [11] and that the diffusion coefficient of Ca in Mg is one order of magnitude smaller (~3×10^{-17} cm^2/s) [4], then the values of $(e^2c/\widetilde{D})$ can be estimated, Table 5-10. This is an approximation, since the diffusivity is expected to vary with bulk alloy concentration. Although not involved extensively in the strengthening process given the low concentration in the α-Mg phase, Sn and Sr (in the case of MRI230D) will also be present, which can affect the rate of diffusion of Al and Ca. In pure Mg, Sn and Sr are both expected to be slow diffusing species. The diffusion coefficient of Sn in Mg at 180°C is 2.22×10^{-17} cm^2/s [12], which is on the order of that of Ca. The diffusion coefficient of Sr in Mg is estimated to be one order of magnitude less than that of Ca [4]. Thus, $\widetilde{D}$ may differ greatly from alloy to alloy, but will not be considered in the current analysis.

Based on the experimentally measured Al and Ca concentrations in the α-Mg phase, MRI230D is expected to have the lowest creep rate from solute strengthening considerations alone, followed by Mg-5Al-3Ca-0.75Sn. The expected minimum creep rates are of the same order of magnitude for the quaternary alloys, which correlates well with the experimentally determined creep rates from Section 5.3.1. The minimum creep

rate for each alloy is plotted against the experimentally determined average ($e^2c/\widetilde{D}$) values in Figure 5.26, using the values for Al alone, Ca alone, and the sum of the Al and Ca. The sum of Al and Ca most accurately ranks the alloys according to minimum creep rate, with the exception of MRI230D which is predicted to be more creep resistant than was experimentally observed. For the quaternary alloys, the minimum creep rate decreases (creep resistance improves) as the value of ($e^2c/\widetilde{D}$) increases. These calculations have considered only solute strengthening, making the assumption that the entire Al and Ca concentrations measured are in solid solution form; as shown in Figure 5.17, however, precipitates are also present in the crept alloys. Therefore, the contribution of precipitate strengthening also needs to be considered and will be discussed in the next section.

The values of ($e^2c/\widetilde{D}$) listed in Table 5-10 are sensitive to the diffusion coefficient used in the calculation. For Al, experimental data is available (e.g. Moreau et al. [11]) but data is lacking for Ca in Mg. The estimated value used in the previous calculations could be off as much as an order of magnitude. The effect of different Ca diffusivities on the solute strengthening has been calculated and is included in Table 5-11. The same Al diffusivity has been used for all calculations, but values of the Ca diffusivity that are one order of magnitude higher and lower than the original estimate have been used, as well as values two times higher or lower (but the same order of magnitude). If the Ca diffusivity is assumed to be one order of magnitude higher (~3×10^{-16} cm^2/s, or approximately equal to the Al diffusivity at 180°C), Mg-6.5Al-2.25Ca-0.8Sn is expected to have a lower creep rate than Mg-5Al-3Ca-0.75Sn, which is not observed experimentally. However, if a diffusivity that is one order of magnitude *lower* is used (~3×10^{-18} cm^2/s), Mg-5Al-3Ca-1.5Sn is expected to have a lower creep rate than Mg-6.5Al-2.25Ca-0.8Sn, which again was not observed. The correct ranking of minimum creep rate for the quaternary Mg-Al-Ca-Sn alloys (0.75Sn < Mg-6.5Al-2.25Ca-0.8Sn < 1.5Sn) is obtained if the Ca diffusivity is assumed to be of the order of 10^{-17} cm^2/s, as in the original estimation. MRI230D is predicted to have a much lower creep rate than experimentally determined regardless of the Ca diffusivity value used.

The higher values of ($e^2c/\widetilde{D}$) calculated for Ca suggests that the Ca concentration in the α-Mg phase is more important to creep than Al, although again this depends somewhat on the value of Ca diffusivity that is used; if the Ca diffusivity is assumed to be approximately the same as the Al diffusivity, the Al contribution has greater weight. The best estimate of Ca diffusivity (one order of magnitude lower than the Al diffusivity) results in a greater contribution of Ca, however. Thus, for Sn to be an effective alloying addition for improved creep resistance, the Ca partitioning to the α-Mg phase must be increased. Of the alloys cast in the current study, Mg-5Al-3Ca-0.25Sn, Mg-5Al-3Ca-0.75Sn and Mg-5Al-3Ca-1Sn have increased Ca partitioning to the α-Mg phase compared with AXJ530, while the Mg-6.5Al-2.25Ca-0.8Sn alloy has approximately the same level of Ca partitioning as AXJ530. Of these alloys, Mg-5Al-3Ca-0.75Sn has the highest maximum and average Ca concentration in the α-Mg phase.

Table 5-9 - Calculated values of e^2c for selected alloys

Alloy	Al - Experimental		Al - Prediction		Ca - Experimental		Ca - Prediction	
	e^2c_{max} ($\times10^{-5}$)	e^2c_{avg} ($\times10^{-5}$)	e^2c_{max} ($\times10^{-5}$)	e^2c_{avg} ($\times10^{-5}$)	e^2c_{max} ($\times10^{-5}$)	e^2c_{avg} ($\times10^{-5}$)	e^2c_{max} ($\times10^{-5}$)	e^2c_{avg} ($\times10^{-5}$)
Mg-5Al-3Ca-0.75Sn	56	31	34	24	53	12	2.9	1.7
Mg-5Al-3Ca-1.5Sn	29	24	36	26	10	5.4	2.5	1.7
Mg-6.5Al-2.25Ca-0.8Sn	61	41	53	33	16	5.0	1.3	0.8
MRI230D	93	54	52	33	64	20	1.7	0.8

Table 5-10 - Values of $(e^2c)/D$ for selected alloys

Alloy ($\dot{\varepsilon}_{min}$)	Al - Experimental		Al - Prediction		Ca - Experimental		Ca - Prediction	
	e^2c_{max}/D	e^2c_{avg}/D	e^2c_{max}/D	e^2c_{avg}/D	e^2c_{max}/D	e^2c_{avg}/D	e^2c_{max}/D	e^2c_{avg}/D
Mg-5Al-3Ca-0.75Sn (1.4×10^{-7} s^{-1})	1.69×10^{12}	9.22×10^{11}	1.02×10^{12}	7.09×10^{11}	1.78×10^{13}	4.02×10^{12}	9.71×10^{11}	5.55×10^{11}
Mg-5Al-3Ca-1.5Sn (3.0×10^{-7} s^{-1})	8.71×10^{11}	7.13×10^{11}	1.10×10^{12}	7.92×10^{11}	3.19×10^{12}	1.80×10^{12}	8.32×10^{11}	5.55×10^{11}
Mg-6.5Al-2.25Ca-0.8Sn (2.51×10^{-7} s^{-1})	1.82×10^{12}	1.23×10^{12}	1.59×10^{12}	9.82×10^{11}	5.41×10^{12}	1.66×10^{12}	4.16×10^{11}	2.77×10^{11}
MRI230D (2.51×10^{-7} s^{-1})	2.82×10^{12}	1.63×10^{12}	1.55×10^{12}	9.82×10^{11}	2.14×10^{13}	6.66×10^{12}	5.55×10^{11}	2.77×10^{11}

Table 5-11 - Effect of variation in Ca diffusivity on solute strengthening

D_{Ca} (cm^2/s)	Total (e^2c)/D (for Al + Ca)			
	0.75Sn	1.5Sn	Mg-6.5Al-2.25Ca-0.8Sn	MRI230D
3×10^{-17}	4.94×10^{12}	2.52×10^{12}	2.90×10^{12}	8.28×10^{12}
3×10^{-16}	1.32×10^{12}	8.94×10^{11}	1.40×10^{12}	2.29×10^{12}
6×10^{-17}	2.93×10^{12}	1.61×10^{12}	2.06×10^{12}	4.95×10^{12}
1.5×10^{-17}	8.97×10^{12}	4.32×10^{12}	4.56×10^{12}	1.49×10^{13}
3×10^{-18}	4.12×10^{13}	1.87×10^{13}	1.79×10^{13}	6.82×10^{13}

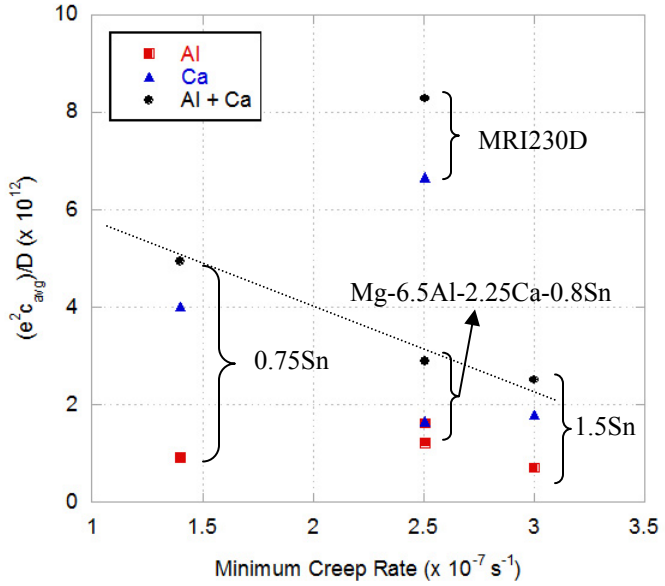

Figure 5.26 - Minimum creep rate vs e^2c/D for Mg-5Al-3Ca-0.75Sn, Mg-5Al-3Ca-1.5Sn, Mg-6.5Al-2.25Ca-0.8Sn and MRI230D

5.4.2 Precipitation Strengthening

Precipitation strengthening can be considered in terms of the Orowan equation. Two versions of the Orowan equation exist, one for dislocations shearing through the precipitates and one for dislocations bowing around the precipitates. Hutchinson et al. have calculated the critical radius for dislocations bowing around the precipitates to be ~3nm for AZ91, which is similar to critical radius for nucleation that they calculated for this same alloy. Therefore, they have assumed that at all times the dislocation will bow around the particle [8]. A similar assumption (of dislocation bowing) will be made for the Al_2Ca precipitates in the current study. In a sample of aged AXJ530, Suzuki [9] has observed steps parallel to the basal plane on gliding non-basal dislocation, Figure 5.27.

These steps were approximately the same size as the Al_2Ca precipitates present in the aged alloy, so it seems valid to assume that the dislocations do not shear the precipitates.

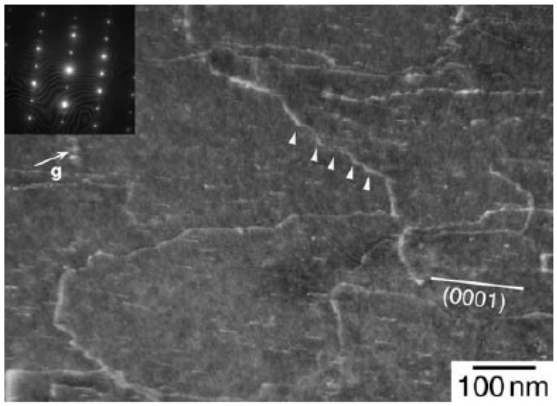

Figure 5.27 - Weak beam DF TEM image of dislocation interaction with basal precipitates in aged AXJ530 [9]. Arrows indicate steps in the dislocation parallel to the basal plane.

Making the assumption of dislocation bowing, the Orowan equation can be written as

$$\Delta\tau = \frac{Gb}{2\pi\lambda\sqrt{1-\nu}}\ln\frac{d_p}{r_0} \qquad (5\text{-}3),$$

for point obstacles of identical strength. Here, $\Delta\tau$ is the increment in critical resolved shear strength (CRSS), G is the shear modulus, b is the Burgers vector, ν is Poisson's ratio, d_p is the mean planar diameter of the point obstacles, r_0 is the core radius of the dislocations and λ is the effective inter-obstacle spacing [13]. Nie has further modified this equation for magnesium alloys containing plate precipitates on the basal plane:

$$\Delta\tau = \frac{Gb}{2\pi\sqrt{1-\nu}\left(\frac{0.953}{\sqrt{f}}-1\right)d_t}\ln\frac{d_t}{b} \qquad (5\text{-}4),$$

where τ is the shear stress, G is the shear modulus, b is the magnitude of the Burgers vector, ν is Poisson's ratio, f is the volume fraction of precipitates, and d_t is the diameter of the precipitate disc [13, 14]. This equation is a much better representation of what actually occurs in precipitate-strengthened Mg alloys, and will be used for the subsequent analysis.

Given the similar base composition of our class of alloys, G, ν and b are not expected to differ much from alloy to alloy. Thus, the parameters that will have the

largest impact on strengthening are f, the volume fraction of precipitates, and d_t, the precipitate diameter. Due to the edge-on view of precipitates lying on multiple basal planes, it can be difficult to measure the true precipitate diameter from a TEM micrograph. The plane of view will slice through the various precipitates at different distances from the center of the disc, resulting in the distribution of precipitate sizes observed in Figure 5.17a. The diameter can be approximated by measuring the largest precipitate present, Table 5-12.

The volume fraction and precipitate diameter affect the mean particle spacing (λ) for the precipitates. Smaller particle spacing will lead to a greater increase in strength. The Mg-5Al-3Ca-0.75Sn alloy is thus expected to have higher precipitate strengthening from the smaller precipitate size (Figure 5.17), assuming a similar volume fraction of precipitates were present in each alloy, which is likely not true. It is difficult to measure the volume fraction of precipitates present from the TEM micrographs, especially given the disc morphology. However, Suzuki et al. has estimated that for a peak-aged AXJ530 specimen, the volume fraction is only a few percent [9]. Pandat simulations predict that at 180°C, the equilibrium volume fraction of C15 (Al_2Ca) is 5.11% for Mg-5Al-3Ca-0.75Sn and 3.50% for MRI230D. If we assume that the additional 1.61% is all in the form of Al_2Ca precipitates in the α-Mg matrix, then Mg-5Al-3Ca-0.75Sn will also have additional strengthening from the increased volume fraction and number density of precipitates.

Using Equation (5-4) and the values in Table 5-12, an approximate change in shear strength ($\Delta\tau$) was calculated for Mg-5Al-3Ca-0.75Sn, Mg-5Al-3Ca-1.5Sn and MRI230D. Two sets of precipitate volume fractions were used: assuming a constant volume fraction of precipitates (~0.02) for all alloys, and using the predicted equilibrium volume fraction of C15 at 180°C from Pandat simulations for each alloy. The predicted volume fraction is likely an overestimate, since C15 is expected to be the stable (equilibrium) eutectic phase at this temperature, rather than C36. The calculated values of $\Delta\tau$ range from ~5-18 MPa for the alloys, which can be converted to tensile strength using a Taylor factor of 5 [8], Table 5-12. Precipitation could account for 20-50% of the creep strength for the alloys (110 MPa). As expected from the smaller precipitate diameter, Mg-5Al-3Ca-0.75Sn has the highest Orowan strengthening from precipitates for either volume fraction, while MRI230D, with the largest precipitate size, has the

lowest strengthening. A higher Orowan strengthening is calculated for Mg-5Al-3Ca-1.5Sn compared with MRI230D, yet the 1.5Sn alloy had a higher minimum creep rate. Thus, it is necessary to consider the contribution of both solute and precipitation strengthening.

Table 5-12 - Contribution of Orowan (precipitate) strengthening to tensile strength

Alloy	G (GPa) [8]	b (nm) [8]	ν [8]	f	d_t (nm)	Δτ (MPa)	σ_{ppt} (MPa)
0.75Sn	17.2	0.32	0.35	0.051	80	17.8	88.9
1.5Sn	17.2	0.32	0.35	0.047	120	12.2	60.8
MRI230D	17.2	0.32	0.35	0.035	225	6.2	31.1
0.75Sn	17.2	0.32	0.35	0.020	80	11.1	55.6
1.5Sn	17.2	0.32	0.35	0.020	120	8.0	39.8
MRI230D	17.2	0.32	0.35	0.020	225	4.7	23.5

Solute strengthening has been considered in terms of creep rate. However, for comparison to the calculated precipitation strengthening contribution, the contribution of solute strengthening to tensile strength can be approximated as:

$$\sigma_{ss} \approx CX^{2/3} \qquad (5\text{-}5),$$

where X is the concentration in atomic fraction and C is a constant, which for Al in Mg is equal to 197 MPa [8]. The constant for Ca is not presently known, so the same value of C will be used for the current analysis. The average Al and Ca concentrations in the α-Mg phase from the electron microprobe scans were converted to at% for the calculation, Table 5-13. The contribution of solute strengthening to tensile strength from Al and Ca ranges from 26.8 MPa for MRI230D to 14.5 MPa for Mg-5Al-3Ca-1.5Sn. These calculations once again assume that the entire Al and Ca concentration measured was in solid solution form. Since precipitates are present, this is obviously not true. Pandat has been used to approximate the actual concentration of Al and Ca that are in solid solution in the α-Mg phase. The average concentration measured by the microprobe was used as the input for a point calculation, which yielded the equilibrium concentration of the α-Mg phase at 180°C. The contribution of solute strengthening to the creep strength was then recalculated with these numbers, Table 5-14. Very low Ca concentrations are predicted for the α-Mg solid solution, so the contribution is dominated by the Al portion. Recall

that the Pandat Scheil calculations from Section 5.2.1 greatly underestimated the Ca concentration of the α-Mg phase during solidification as well, so the low Ca concentration determined here was not completely unexpected. The values included in Tables 5-13 and 5-14 thus most likely represent the upper and lower bounds of the solute contribution, respectively.

The sum of precipitate and solute strengthening contributions are included in Table 5-15, and have been converted to Vickers hardness using the following equation:

$$Hv = 0.44\ (\sigma + 39) \qquad (5\text{-}6),$$

which was determined by Caceres et al. [15] for gravity cast Mg-Al alloys. Mg-5Al-3Ca-0.75Sn was calculated to have the highest hardness, 64.4 Hv (or 49.8 Hv if a constant precipitate volume fraction of 0.02 is used). The measured age hardness of this alloy was 70.5 Hv, so there is decent agreement between the calculation and experiment for this alloy. Mg-5Al-3Ca-1.5Sn had a calculated hardness of 50.2 Hv (or 41.1 Hv), while the measured hardness was 56.2 Hv. For MRI230D, there agreement between calculated (42.6 Hv or 39.3 Hv, depending on which volume fraction is used) and experimentally determined hardness values (66.1 Hv) is not as good. Still, relatively good accuracy was obtained in general, given the number of approximations and assumptions made, and the Mg-5Al-3Ca-0.75Sn was correctly identified as having the highest precipitate strengthening and hardness. A more detailed analysis would also consider grain size effects [8].

Table 5-13 - Contribution of solute strengthening to tensile strength

Alloy	**c_{avg} – Al (at%)**	**c_{avg} – Ca (at%)**	**σ_{ss} – Al (MPa)**	**σ_{ss} – Ca (MPa)**	**σ_{ss} – Al + Ca (MPa)**
0.75Sn	2.00	0.29	14.5	4.0	18.5
1.5Sn	1.54	0.13	12.2	2.3	14.5
MRI230D	3.51	0.49	21.1	5.7	26.8

Table 5-14 - Contribution of solute strengthening to tensile strength using Pandat predicted concentrations

Alloy	c_{Al} in α-Mg (at%)	c_{Ca} in α-Mg (at%)	σ_{ss} – Al (MPa)	σ_{ss} – Ca (MPa)	σ_{ss} – Al + Ca (MPa)
0.75Sn	1.50	2.42×10^{-6}	12.0	0.002	12.0
1.5Sn	1.30	2.88×10^{-6}	10.9	0.002	10.9
MRI230D	2.00	1.39×10^{-6}	14.5	0.001	14.5

Table 5-15 - Combined contribution of solute and precipitation strengthening to tensile strength and hardness

Alloy	σ_{ppt} (MPa)	σ_{ss} (MPa)	$\sigma_{(ppt + ss)}$ (MPa)	Calculated Hardness (Hv)	Measured Hardness (Hv)
0.75Sn	88.9	18.5	107.4	64.4	70.5 +/- 6.2
1.5Sn	60.8	14.5	75.3	50.2	56.2 +/- 9.0
MRI230D	31.1	26.8	57.9	42.6	66.1 +/- 6.9
0.75Sn*	55.6	18.5	74.1	49.8	70.5 +/- 6.2
1.5Sn*	39.8	14.5	54.3	41.1	56.2 +/- 9.0
MRI230D*	23.5	26.8	50.3	39.3	66.1 +/- 6.9

* Using a precipitate volume fraction of 0.02

Despite the smaller precipitate size and increased number density in Mg-5Al-3Ca-0.75Sn, only a modest decrease in minimum creep rate (~2x) is obtained compared with MRI230D and Mg-5Al-3Ca-1.5Sn. This is because the basal plane orientation of the precipitates is the least effective for blocking slip of basal <a> dislocations [8, 13]. Basal dislocations can interact weakly with plate-shaped precipitates with the basal orientation, but these precipitates do serve as effective obstacles for prismatic or pyramidal dislocations [9]. To greatly increase the precipitation strengthening in these alloys, it is necessary to either substantially increase the number density of basal precipitates present or to somehow change the morphology of the precipitate [8, 16]. Both of these can theoretically be done through alloying additions, although the latter approach is the more difficult.

In some Mg alloys, microalloying additions have successfully been shown to increase the number density of precipitates present. For example, in the Mg-Sn binary

system, ternary microadditions of 0.1at% Na and 0.5at% In-Li to Mg-1.3at%Sn and Mg-1.9at%Sn, respectively, have increased the number density by two orders of magnitude (from 10^{17} to 10^{19} m^{-3}). These microalloying additions are not appropriate for Mg-Al alloys, however, due to the phase separation tendencies between Al and Na and In [17]. Trace amounts of Cu added to AZ91 increased the number of precipitates by a factor of 10 [16], and minor additions of Bi or Sb may also refine the β-$Mg_{17}Al_{12}$ precipitates [18]. Figure 5.28 shows the effect of increasing the volume fraction of precipitates on the mean particle spacing for AZ91.

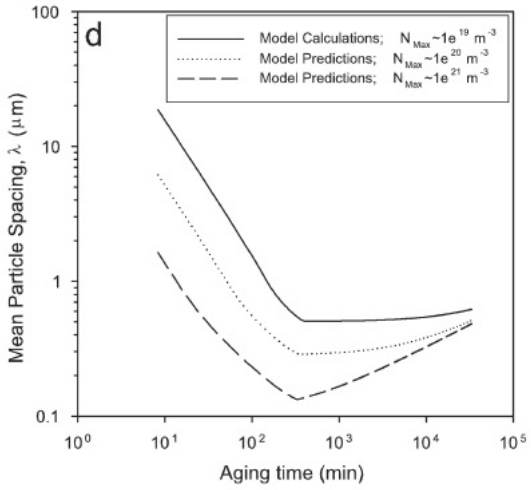

Figure 5.28 - Mean particle spacing vs aging time for AZ91. Three different precipitate volume fractions have been modeled [8].

Basal plate precipitates lead to the smallest increase in strength since they have the least effective orientation for inhibiting the glide of basal dislocations. Alloys like WE54 and binary Mg-Y alloys, which have prismatic plate precipitates, Figure 5.29, have a much larger increase in strength with aging [8, 19]. These prismatic plates are very effective obstacles for basal slip. In Figure 5.30, the inter-particle spacing is plotted against the number density at a given volume fraction for four different precipitate orientations. Prismatic plates, [0001] rods and spherical precipitates are all more effective strengtheners than basal plates. However, to date, no alloying additions have been identified which will change the precipitate morphology in Mg-Al alloys, although this has not been the focus of many studies.

Basal plate precipitates are effective obstacles to non-basal dislocations, however. It has been suggested that non-basal dislocations in the near-grain-boundary region

account for the localized damage that occurs after the minimum creep rate is reached in samples of permanent mold cast AXJ530 [4]. By inhibiting the motion of non-basal dislocations in this region, the onset of damage could be delayed and the creep resistance improved. Certain alloying additions (e.g. Al, Zn and Li [20, 21]) have also been found to decrease the CRSS for non-basal deformation, perhaps making basal precipitates more effective strengtheners for these alloys. Based on the solute profiles discussed earlier, increased Al and Ca concentrations are observed in the near-interdendritic regions as well, perhaps leading to increased solute or precipitation strengthening in this region. Further investigation of the behavior of basal and non-basal dislocations in the near-interdendritic region is needed to fully answer this question, however.

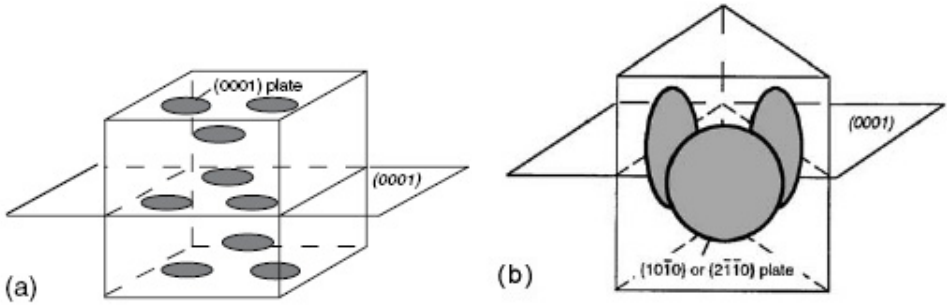

Figure 5.29 - Illustration of a) basal and b) prismatic precipitate plates [13].

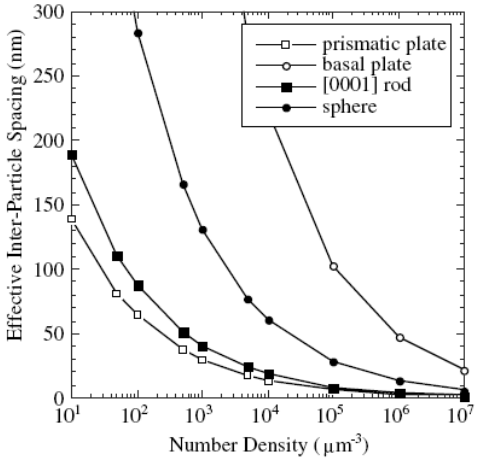

Figure 5.30 - Variation of inter-particle spacing with number density for various precipitate orientations, calculated at a precipitate volume fraction of 0.04 [13].

Nucleation and growth of precipitates removes solute from the α-Mg phase, reducing the amount of solute strengthening that can occur, illustrated in Figure 5.31 for AZ91. If the precipitates are efficient strengtheners, the reduction in solute strengthening

will have less impact on the creep resistance, since it will be offset by the increased precipitation strengthening. However, if the precipitates are not efficient strengtheners, e.g. a low volume fraction of large, widely-spaced basal plates, then removing solute will have a pronounced negative effect on the minimum creep rate. For example, precipitates of β-$Mg_{17}Al_{12}$ that form during continuous precipitation in Mg-Al-base alloys have been suggested to be inefficient strengtheners; they are reported to coarsen rapidly during high temperature exposure in AZ91 [22] and AE42 [23], leading to a reduction in creep resistance. It seems reasonable to conclude that Al_2Ca precipitation decreases the solute strengthening of MRI230D at 180°C, based on the higher creep rate measured for this alloy. Based on solute strengthening effects alone, MRI230D was predicted to have a lower creep rate than Mg-5Al-3Ca-0.75Sn, but this was not observed experimentally.

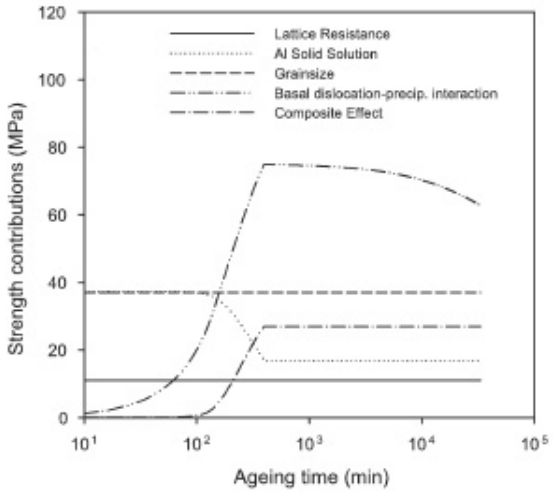

Figure 5.31 - Contribution of various strengthening mechanisms to the overall strength of AZ91 [8]. The solute strengthening decreases as the precipitation strengthening increases until the start of coarsening.

According to Suzuki et al., the volume fraction of Al_2Ca precipitates in Mg-Al-Ca alloys can be increased by increasing the Ca solubility in the α-Mg phase through alloying additions [9]. As shown in the current study, the addition of ~0.75wt% Sn led to an increase in Ca partitioning to the α-Mg phase, which in turn led to a slight increase in creep resistance. No attempt has been made to optimize the aging treatment for Mg-5Al-3Ca-0.75Sn, so further improvement in creep resistance may be possible for this alloy. However, increased solute and precipitation strengthening have been demonstrated in the

quaternary Mg-Al-Ca-Sn system, proving additions of Sn can be effectively used to improve the creep resistance of Mg-Al-Ca-based alloys.

5.5 Implications for Alloy Design

The current investigation has demonstrated the importance of understanding the solidification path and elemental partitioning during design of new alloys. Since creep is predominantly controlled by viscous glide of <a> dislocations for Mg-Al-Ca alloys, solute and precipitation strengthening are viable ways to decrease dislocation mobility, which in turn leads to higher creep resistance.

Through the incorporation of thermodynamic modeling in the alloy design process, Mg-Al-Ca-based alloys with improved creep resistance can be developed for high temperature applications. Alloying additions that increase the concentration of Ca in the α-Mg phase during the solidification process are especially of interest. At creep temperatures, the precipitation of the Al_2Ca phase (C15) should be possible for increased strengthening of the α-Mg matrix, although thermodynamic models will not provide information on the kinetics of the precipitation process. Instead, this requires the use of nucleation and growth models, which is difficult given the lack of some fundamental information, including diffusivity in these complex alloys. Quaternary or higher order additions that increase Ca solubility at lower temperatures and Ca partitioning during solidification will be particularly useful for future alloy development. As mentioned earlier, microalloying additions that increase the volume fraction of C15 precipitates can also increase the precipitate strengthening possible at creep temperatures. These microalloying additions may also help delay coarsening and overaging of the precipitates, which would improve the creep resistance as well. The current investigation has shown that Sn additions of ~0.75wt% to an Mg-5Al-3Ca alloy can lead to minor improvements in the creep resistance at 180°C compared with MRI230D, which has been targeted for powertrain applications. This is attributed to the small precipitate size/spacing and the potential for an increased volume fraction of Al_2Ca precipitates at creep temperatures in the Mg-5Al-3Ca-0.75Sn alloy.

The Ca concentration in the α-Mg phase contributes more to solute strengthening than the Al concentration. For improved creep resistance, Sn additions should be

selected so as to maximize the Ca concentration in the α-Mg phase through increased Ca partitioning during solidification. Considering the Mg-5Al-3Ca-xSn alloys cast in the current study, additions of 0.75wt%, 0.25wt% and 1wt% increased Ca partitioning the most, listed in decreasing order of effectiveness. These same alloys also had the highest fraction eutectic for the quaternary series. The reverse is also true – the alloy with the lowest fraction of eutectic (3wt% Sn) also had the lowest Ca partitioning to the α-Mg phase. Within the Mg-xAl-3Ca-0.5Sn series, the highest Ca partitioning was observed for the alloy with largest eutectic fraction as well (Mg-8Al-3Ca-0.5Sn); however, this trend was not true for the other two alloys in the series. Comparison cannot be made across multiple series though; the Mg-5Al-3Ca-0.75Sn alloy had the highest Ca partitioning to the α-Mg phase, yet the Mg-8Al-3Ca-0.5Sn alloy had the highest fraction eutectic. The increase in Ca partitioning to the α-Mg phase, as well as the slower precipitate growth/overaging observed for the 0.75Sn alloy also suggests that Sn additions ultimately change the free energy of the α-Mg phase.

The effect of quaternary alloying additions on elemental partitioning to the α-Mg is not very well understood for most elements. The current investigation has focused on Sn, but other elements may exist that will similarly increase Ca partitioning to the α-Mg phase as well as the average Ca concentration in this phase. Using the Pandat thermodynamic database several potential additions have been identified, although further experiments are necessary to confirm the validity of these predictions. Using a base composition of Mg-5Al-3Ca-0.75X, silver (Ag), cerium (Ce), gadolinium (Gd), lithium (Li), neodymium (Nd) and zinc (Zn) were predicted to have a slight increase in Ca concentration in the α-Mg phase compared with Sn, Table 5-16. Pandat underestimates the Ca concentration for the 0.75Sn alloy however, so it is difficult to predict how the actual Ca concentration will compare. A slightly higher average Al concentration is predicted for the 0.75X alloys compared with the 0.75Sn alloy. The relevant properties for each of the alloying additions are summarized in Table 5-16, and the predicted Scheil segregation curves for Ag are compared with those of Sn in Figure 5.32 as an example. Ag, Gd, Li and Zn all have significant solubility in the α-Mg phase. Equilibrium phase calculations predict at least 5% Al_2Ca (C15) at 180°C for these same elements, and the melting point of the alloy remains below 700°C. Additions of Ni, Sc,

C, Si, Y and Zr greatly increased the melting point of the alloy, leading to potential difficulties in processing the alloys. Thus, these latter elements were not considered in great detail. Only a composition of Mg-5Al-3Ca-0.75X has been considered at the current time; other compositions should also be considered to optimize the effect of these alloying additions on Al and Ca partitioning to the α-Mg phase.

Table 5-16 - Properties of Mg-5Al-3Ca-0.75X alloys

Element	Max. Solubility in Mg (%) [24]	Atomic radius (pm)	Solidification Temperature (°C)	c_{avg} – Al (wt%)	c_{avg} – Ca (wt%)	c_{avg} – X (wt%)	% C15 at 180°C	% Eutectic (Scheil)
Ag	15	144	609.1	1.87	0.08	0.24	5.6	27.2
C			1936.5					
Ce	0.52	182	607.9	1.81	0.09	0.0007	5.6	25.0
Gd	23.5	180	608.2	1.77	0.08	0.10	5.6	24.7
Li	6	152	608.7	1.89	0.10	0.67	5.4	25.2
Nd	0	181	605.1	1.78	0.08	0.0007	5.6	24.7
Ni	0	124	787.8					
Sc	24.6	162	875.3					
Si	0	111	785.9					
Sn	14.5	163	608.3	1.69	0.06	0.10	5.1	24.4
Y	11.4	180	1192.9					
Zn	6.2	134	607.6	1.90	0.08	0.11	5.6	26.7
Zr	3.8	160	1736					

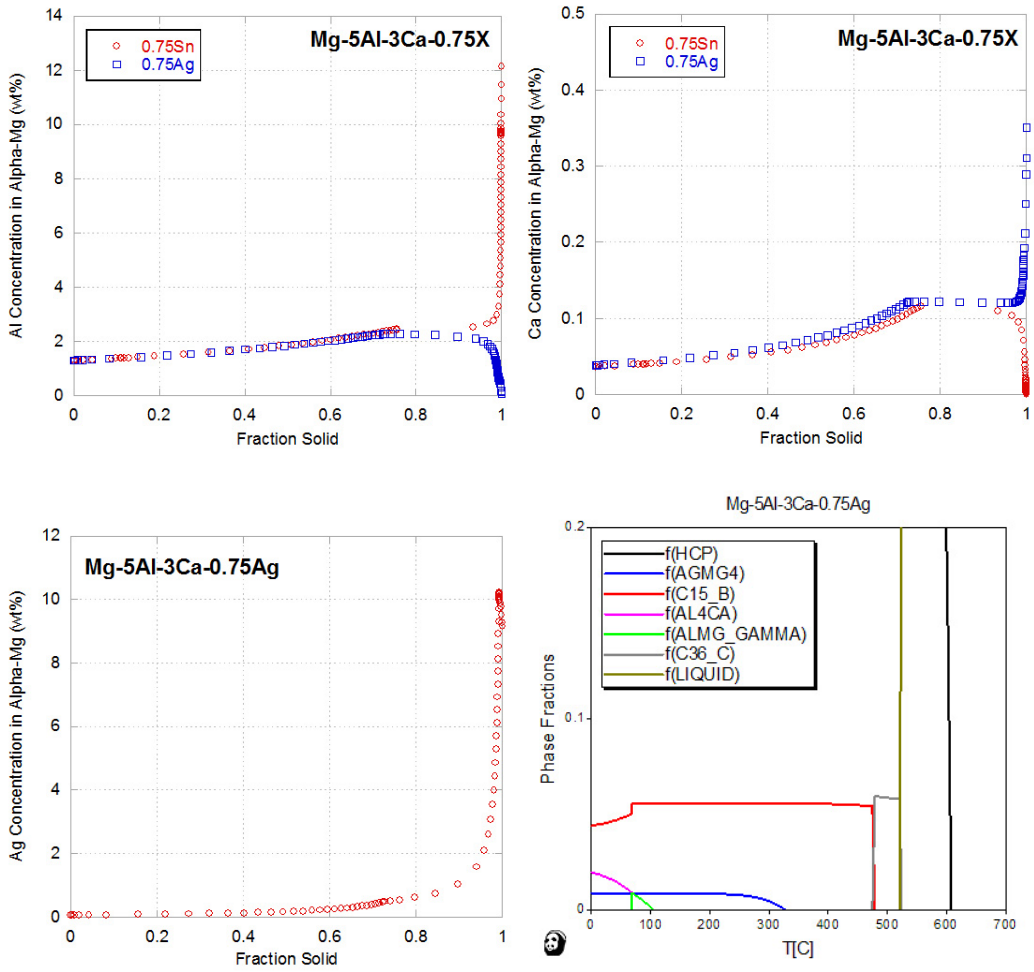

Figure 5.32 - Pandat predictions of a) Al concentration in α-Mg, b) Ca concentration in α-Mg, c) Ag concentration in α-Mg and d) equilibrium phase fractions as a function of temperature for Mg-5Al-3Ca-0.75Ag. Data for Mg-5Al-3Ca-0.75Sn is included in a-b) for comparison.

References

[1] A. Kozlov, M. Ohno, R. Arroyave, Z. K. Liu, R. Schmid-Fetzer, *Intermetallics* **2008**, *16*, 299.

[2] A. Kozlov, M. Ohno, T. Abu Leil, N. Hort, K. U. Kainer, R. Schmid-Fetzer, *Intermetallics* **2008**, *16*, 316.

[3] A. Suzuki, N. D. Saddock, L. Riester, E. Lara-Curzio, J. W. Jones, T. M. Pollock, *Metallurgical and Materials Transactions A* **2007**, *38A*, 420.

[4] N. D. Saddock, Ph.D. thesis, University of Michigan (Ann Arbor, MI), **2007**.

[5] A. Suzuki, N. D. Saddock, J. R. TerBush, B. R. Powell, J. W. Jones, T. M. Pollock, in *Magnesium Technology 2007* (Eds.: R. S. Beals, A. A. Luo, N. R. Neelameggham, M. O. Pekguleryuz), TMS, Orlando, FL, **2007**, pp. 375.

[6] R. Wagner, R. Kampmann, P. W. Voorhees, in *Phase Transformations in Materials* (Ed.: G. Kostorz), Wiley-VCH, Weinheim, **2001**, pp. 309.

[7] C. Sigil, *Materials Science Forum* **2000**, *331-337*, 513.

[8] C. R. Hutchinson, J. F. Nie, S. Gorsse, *Metallurgical and Materials Transactions A* **2005**, *36A*, 2093.
[9] A. Suzuki, N. D. Saddock, J. R. TerBush, B. R. Powell, J. W. Jones, T. M. Pollock, *Metallurgical and Materials Transactions A* **2008**, *39A*, 696.
[10] F. A. Mohamed, T. G. Langdon, *Acta Metall.* **1974**, *22*, 779.
[11] G. Moreau, J. A. Cornet, D. Calais, *Journal of Nuclear Materials* **1971**, *38*, 197.
[12] S. Cohen, G. Goren-Muginstein, S. Avraham, B. Rashkova, G. Dehm, M. Bamberger, *Z. Metallkd.* **2005**, *96*, 1081.
[13] J. F. Nie, *Scripta Materialia* **2003**, *48*, 1009.
[14] J. F. Nie, B. C. Muddle, in *Magnesium Alloys and their Applications* (Eds.: B. L. Mordike, K. U. Kainer), Werkstoff-Informationsgesellschaft mbH, Frankfurt, Germany, **1998**, pp. 229.
[15] C. H. Caceres, J. R. Griffiths, A. R. Pakdel, C. J. Davidson, *Materials Science and Engineering A* **2005**, *402*, 258.
[16] C. J. Bettles, M. A. Gibson, *Advanced Engineering Materials* **2003**, *5*, 859.
[17] C. L. Mendis, C. J. Bettles, M. A. Gibson, S. Gorsse, C. R. Hutchinson, *Philosophical Magazine Letters* **2006**, *86*, 443.
[18] Y. Guangyin, S. Yangshan, D. Wenjiang, *Materials Science and Engineering A* **2001**, *308*, 38.
[19] J. F. Nie, B. C. Muddle, *Acta Materialia* **2000**, *48*, 1691.
[20] E. W. Kelley, W. F. Hosford Jr., *Transactions of the Metallurgical Society of AIME* **1968**, *242*, 5.
[21] A. Akhtar, E. Teghtsoonian, *Acta Metall.* **1969**, *17*, 1351.
[22] W. Blum, B. Watzinger, P. Zhang, *Advanced Engineering Materials* **2000**, *2*, 349.
[23] S. M. Zhu, M. A. Gibson, J. F. Nie, M. A. Easton, T. B. Abbott, *Scripta Materialia* **2008**, *58*, 477.
[24] *ASM Handbook, Vol. 3 - Alloy Phase Diagrams*, ASM International, **1992**.

Chapter 6

Conclusions and Recommendations

6.1 Conclusions

Vehicle mass can be greatly reduced by the use of lightweight cast magnesium alloys in automotive applications. These alloys are typically used in the as-cast condition. Thus, a fundamental understanding of the role of alloy composition on elemental partitioning during solidification and the subsequent development of creep resistant microstructures is critical to the development of new alloys to meet these applications. The objective of the current research has been to advance this understanding in the commercially relevant Mg-Al-Ca ternary system. Improved understanding of creep deformation mechanisms in this system has been achieved through the characterization of dislocation structures that develop during creep, and the role of solute and precipitation strengthening in improving creep resistance has been explored. Specifically, the effect of Sn additions on elemental partitioning during solidification has been investigated. Sn was chosen for both its high solubility in Mg and because preliminary elemental partitioning results from MRI230D suggested that Sn additions could potentially increase the partitioning of Al and Ca to the α-Mg phase. The conclusions drawn from this investigation are presented and recommendations for further research are presented in the remainder of this chapter.

Viscous glide of <a> dislocations was determined to be the dominant creep mechanism in Mg-Al-Ca-based alloys for temperatures between 100 and 180°C at 110 MPa, conditions relevant for the most extreme automotive powertrain applications. A random distribution of mostly basal and non-basal <a> dislocations that were confined mainly to the α-Mg cell interiors were observed in all crept alloys. Minimal interaction was observed between dislocations and eutectic phases in the interdendritic region, although this was not a major focus of the current study and should be investigated in

greater detail before any conclusions are drawn on the behavior of dislocations in the near-interdendritic region. Creep in the Mg-Al-Ca ternary system examined here is predominantly controlled by dislocation glide in the α-Mg phase, and compositional/microstructural changes offer a pathway for improved creep resistance.

The addition of 0.75-1wt% Sn to Mg-5Al-3Ca alloys led to increased partitioning of Ca to the α-Mg phase during solidification, which led in turn to improved creep properties. The greatest partitioning was observed for alloys with a higher fraction of eutectic. When greater than 1wt% Sn was added to this same series of alloys, however, the solidification path was modified such that CaMgSn became the first phase to form, which in turn led to decreased Ca partitioning to the α-Mg phase. Sn additions to Mg-5Al-3Ca resulted in lower Al partitioning to the α-Mg phase compared with AX44 and AXJ530. The high Al and Ca partitioning that was observed in MRI230D (Mg-6.5Al-2.25Ca-0.25Sr-0.8Sn) is likely due to the combination of Sr and Sn present in the alloy, rather than from Sn additions alone. The free energy of the phases present in Mg-5Al-3Ca-0.75Sn changes with the addition of Sn, leading to an increased average Ca concentration in the α-Mg phase, especially in the near-interdendritic region.

Solute and precipitation strengthening of the α-Mg phase are an effective means to improve the creep resistance of Mg-Al-Ca alloys. The contribution to solute strengthening has been calculated using Mohamed and Langdon's equation which relates the creep rate to diffusivity, atomic size misfit and solute concentration of Al and Ca in the α-Mg phase as a function of $(e^2c/\tilde{D})^{-1}$. From these calculations it was determined that the Ca concentration in the α-Mg phase is more important to creep resistance than the Al concentration due to the lower diffusivity and larger atomic misfit of Ca in Mg. Thus, Sn additions that increase the Ca concentration in the α-Mg phase are effective at improving creep resistance, and should be targeted in future alloy development, in addition to other alloying elements that increase Ca partitioning to the α-Mg phase. However, consideration of partitioning alone is not enough ensure improved creep resistance; high average concentrations of Ca (and Al, to a lesser extent) in the α-Mg phase are also necessary. In the current investigation, increased Ca partitioning with the highest average Ca concentration measured in the α-Mg phase for the quaternary alloys was measured for the Mg-5Al-3Ca-0.75Sn alloy. For a fixed level of solute, increasing

the partitioning to the α-Mg phase will increase solute strengthening to some extent, but the goal should be high levels of desirable solute in the α-Mg paired with the highest possible partitioning during solidification.

The minimum creep rate for Mg-5Al-3Ca-0.75Sn was approximately two times lower than for the other alloys crept at 110 MPa and 180°C. Solute strengthening can account for part of the differences observed, but precipitation strengthening must also be considered. Basal disc precipitates of Al_2Ca (C15) were observed in crept specimens for all three Mg-Al-Ca-Sn alloys examined. These precipitates were smaller in the 0.75Sn alloy, and an apparent increase in volume fraction of precipitates was observed compared to the other alloys, although the exact increase is difficult to quantify given the precipitate morphology and limited volume of material examined. A modified Orowan equation was used to calculate the contribution of precipitation strengthening, and it was determined that precipitation could account for 20-50% of the creep strength for the three alloys. When the summed contribution of solute strengthening and precipitation strengthening were considered, the Mg-5Al-3Ca-0.75Sn alloy was correctly predicted as the alloy with the lowest creep rate. MRI230D would be expected to have the lowest creep rate if only solute strengthening were considered, but when precipitation strengthening is also considered, MRI230D is more accurately predicted to have a creep resistance similar to Mg-5Al-3Ca-1.5Sn, indicating that the precipitates present in MRI230D are less effective strengtheners than those present in Mg-5Al-3Ca-0.75Sn.

6.2 Recommendations for Future Research

Based on the findings of this study, the following recommendations are made for future investigations:

(1) Measurement of the diffusion coefficients in these complex alloy systems are needed for accurate models of creep, solute strengthening and precipitate nucleation and growth. Although the diffusion coefficients of Al [1] and Sn [2] in pure Mg have been reported for a limited range of temperatures, diffusivity data for Ca and Sr is lacking and has been approximated in the current investigation. No data is available for the diffusivity of the elements in the ternary or quaternary alloy. Based on the aging kinetics for MRI230D and the Sn-containing quaternaries, Sn additions have been suggested to

slow the diffusion of Al and/or Ca in the α-Mg compared to AXJ530. Diffusion couples would be necessary for these measurements, and a technique similar to that of Dayananda and Sohn [3], which has been applied to Cu-Ni-Zn, Fe-Ni-Al and Ni-Cr-Al, could be used to calculate the ternary interdiffusion coefficients. A similar approach has been successfully applied by Kulkarni et al. for an RuAl-NiAl couple [4].

(2) Saddock [5] has demonstrated in crept samples of permanent-mold cast AXJ530 that strain is heterogeneously distributed on the order of the grain size, with some grains experiencing more local strain than others. This distribution of strain may affect the dislocation substructures that are observed in the TEM, although more studies are needed to confirm this. The alloys studied in the current investigation were expected to have similar grain sizes (on the order of 200 μm), and thus the grain to grain variability in dislocation substructures should be investigated. The strain mapping technique employed by Saddock could be used to select specific regions of a sample to examine (i.e. from a highly strained grain and a grain with lower local strain), and TEM samples could be prepared via FIB lift-out to compare the dislocation substructures that develop in these each of these regions.

(3) Similarly, an investigation of the variability of the dislocation substructures between cell interiors and near-interdendritic regions should also be conducted. The current study has focused on the cell interiors, and although little interaction between the dislocations and eutectic phases was observed, only limited areas near the interdendritic region were examined. Some dislocation/eutectic interaction must be occurring, since the α-Mg cells cannot deform on their own, isolated from the rest of the microstructure. Increased solute concentrations were measured in the near-eutectic regions with the electron microprobe in the current investigation, which should impact dislocation motion differently than in the cell interiors where the solute concentration is lower. The precipitation behavior of the near-interdendritic region should be examined, as well as the density of basal and non-basal dislocations in this region. It has been suggested [5] that the onset of damage at grain boundaries is related to the activity of non-basal dislocations after the minimum creep rate has been reached. The approach described above in (2) could also be used to better understand at what strain level non-basal dislocations become relevant to the creep deformation behavior. Basal plate precipitates are effective

obstacles to non-basal dislocation motion, so the effect of precipitates in the near-interdendritic region on the onset of damage (void/crack nucleation) in this area could be examined in greater detail.

(4) For the precipitation strengthening model utilized in the current study, approximations of precipitate size and volume fraction were made. A more thorough TEM investigation, including the use of HRTEM and perhaps atom probe to examine the precipitates, would allow a more precise determination of these parameters. More samples would need to be examined in order to increase the confidence of the measurements, and multiple zone axes would need to be used. The $[11\bar{2}0]_\alpha$ zone axis most commonly used in this investigation allows determination of orientation, but only a cross-sectional view (through thickness) of the disc-shaped precipitates; the $[1\bar{2}13]_\alpha$ zone axis should provide a view of the entire precipitate disc. Foil thickness would also have to be known, or perhaps calculated from thickness fringes or convergent beam techniques [6], to accurately measure the precipitate volume fraction.

(5) The creep deformation behavior of additional alloys from the Mg-Al-Ca-Sn system should be examined to build on the results presented here. Increased Ca partitioning has been suggested to increase the creep resistance, so the Mg-5Al-3Ca-0.25Sn and Mg-5Al-3Ca-1Sn alloys are expected to have lower minimum creep rates than the Mg-5Al-3Ca-0.5Sn or Mg-5Al-3Ca-3Sn alloys. Die-cast specimens of the Mg-5Al-3Ca-0.75Sn alloy should also be crept in tension for direct comparison with the creep tests conducted for AXJ530, MRI153M and MRI230D. If a wider range of temperatures and stresses are used, activation energies and stress exponents can also be calculated for comparison to studies from the literature.

(6) Identification of micro-alloying additions that will increase the precipitate density at creep temperatures or change the precipitate habit plane. Additions of less than 1at% Na or In-Li to Mg-Sn binary alloys increased the precipitate number density by two orders of magnitude, but these additions do not work for Mg alloys that contain Al. In Mg-Y alloys, the precipitates that form during high temperature exposure have prismatic orientation and can better impede the motion of basal dislocations. Either approach will lead to an increase in precipitate strengthening, which in turn should decrease the creep rate and thereby increase the creep resistance of the alloy.

References

[1] G. Moreau, J. A. Cornet, D. Calais, *Journal of Nuclear Materials* **1971**, *38*, 197.

[2] S. Cohen, G. Goren-Muginstein, S. Avraham, B. Rashkova, G. Dehm, M. Bamberger, *Z. Metallkd.* **2005**, *96*, 1081.

[3] M. A. Dayananda, Y. H. Sohn, *Metallurgical and Materials Transactions A* **1999**, *30*, 535.

[4] K. N. Kulkarni, B. Tryon, T. M. Pollock, M. A. Dayananda, *Journal of Phase Equilibria and Diffusion* **2007**, *28*, 503.

[5] N. D. Saddock, Ph.D. thesis, University of Michigan (Ann Arbor, MI), **2007**.

[6] S. Celotto, *Acta Materialia* **2000**, *48*, 1775.